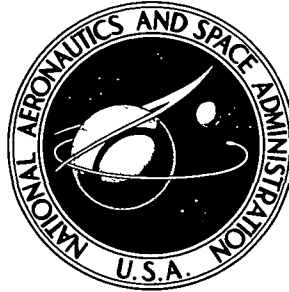


NASA CONTRACTOR
REPORT



NASA CR-2214

Declassified by authority of NASA
Classification Change Notices No. 242
Dated ** 1 DEC 1977

NASA CR-2214

CONFIDENTIAL	CLASSIFIED
BY Henry A. Fedziuk	
SUBJECT TO GENERAL DECLASSIFICATION SCHEDULE OF EXECUTIVE ORDER 11652, AUTOMATICALLY DOWNGRADED AT TWO YEAR INTERVALS AND DECLASSIFIED ON DEC 31 1979	

CLASSIFICATION CHANGE

UNCLASSIFIED

Authority of ADA-42 Memo
Classified by ODANIA L. MERBIT Date 3/30/77
Classified Document in the General Station, NASA
Scientific and Technical Information Facility

CLASSIFIED FILE

TWO-DIMENSIONAL WIND-TUNNEL TESTS
OF A NASA SUPERCRITICAL AIRFOIL
WITH VARIOUS HIGH-LIFT SYSTEMS

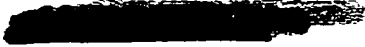
Volume I - Data Analysis

by *E. Omar, T. Zierten, and A. Mahal*

Prepared by
THE BOEING COMPANY
Seattle, Wash. 98124
for Langley Research Center

1. Report No. NASA CR-2214		2. Government Accession No		3. Recipient's Catalog No.	
4. Title and Subtitle TWO-DIMENSIONAL WIND-TUNNEL TESTS OF A NASA SUPERCRITICAL AIRFOIL WITH VARIOUS HIGH-LIFT SYSTEMS - VOLUME I - DATA ANALYSIS				5. Report Date April 1973	
7. Author(s) E. Omar, T. Zierten, and A. Mahal				6. Performing Organization Code	
9. Performing Organization Name and Address The Boeing Company Commercial Airplane Group Seattle, Washington 98124				8. Performing Organization Report No. D6-41063-1	
				10. Work Unit No. 760-64-60-01	
12. Sponsoring Agency Name and Address National Aeronautics and Space Administration Washington, D. C. 20546				11. Contract or Grant No. NAS1-10824	
				13. Type of Report and Period Covered Contractor Report	
				14. Sponsoring Agency Code	
15. Supplementary Notes					
16. Abstract In fulfillment of NASA contract NAS1-10824, "Two-Dimensional Wind Tunnel Tests of a NASA Supercritical Airfoil With Various High-Lift Systems," three high-lift systems for a NASA, 9.3%, blunt-based, supercritical airfoil were designed, fabricated, and wind tunnel tested. In addition, a method furnished by NASA for calculating the viscous flow about two-dimensional multicomponent airfoils was evaluated by comparing its predictions with test data. The primary objective of this program was to determine whether high-lift systems derived from supercritical airfoils would have performance comparable to high-lift systems derived from conventional airfoils. The high-lift systems for the supercritical airfoil were designed to achieve maximum lift and consisted of: (1) a single-slotted flap, (2) a double-slotted flap and a leading-edge slat, and (3) a triple-slotted flap and a leading-edge slat. This volume contains a summary of the wind-tunnel data obtained for these high-lift systems and a comparison between their performance characteristics and those of high-lift systems for more conventional airfoils. Agreement between theoretical predictions and experimental results are also discussed.					
17. Key Words (Suggested by Author(s)) Supercritical Airfoil High-Lift Flap Systems Two-Dimensional Data				18. Distribution Statement [REDACTED] available to U. S. Government Agencies and their contractors only	
19. Security Classif. (of this report) [REDACTED]		20. Security Classif. (of this page) Unclassified		21. No. of Pages 88	22. Price*
<p style="text-align: center;">"NATIONAL SECURITY INFORMATION"</p> <p style="text-align: center;">Unauthorized Disclosure Subject to Criminal Sanctions</p>				<p style="text-align: center;">CONFIDENTIAL CLASSIFIED</p> <p style="text-align: center;">Henry A. Fedziuk</p> <p style="text-align: center;">SUBJECT TO SECURITY CLASSIFICATION SCHEDULE OF EXECUTIVE ORDER 11652 AUTOMATICALLY DOWNGRADED AT TWO-YEAR INTERVALS AND DECLASSIFIED ON 08-20-81</p> <p style="text-align: center;">1979</p>	

Page Intentionally Left Blank



FOREWORD

This report was prepared in fulfillment of National Aeronautics and Space Administration contract NAS1-10824. The contract was awarded 26 May 1971 to the Aerodynamics Research Unit of The Boeing Company Commercial Airplane Group as part of a systems study for defining an advanced-technology transport aircraft system.

The contract study involved the design, fabrication, and two-dimensional wind tunnel testing of three high-lift configurations of a 9.3% thick NASA supercritical airfoil. The high-lift configurations consisted of a single-slotted trailing-edge flap and no leading-edge device, a double-slotted trailing-edge flap and a leading-edge slat, and a triple-slotted trailing-edge flap and a leading-edge slat. The slot geometry and deflections of the high-lift systems were varied to achieve maximum lift.

In addition, an analytical method furnished by NASA for calculating the viscous flow about two-dimensional multicomponent airfoils was evaluated by comparing its predictions with test data.

1971-10824-1-1

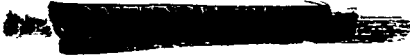
Page Intentionally Left Blank



CONTENTS

	Page
SUMMARY	1
INTRODUCTION	3
SYMBOLS	5
TEST PROGRAM	9
Models	9
High-Lift System Design	9
Experimental Optimization Procedure	11
Test Facilities	12
Data Acquisition	12
TEST RESULTS	13
Sectional Characteristics	13
Comparison of High-Lift Systems	17
Comparison of Leading-Edge Slats	19
High-Lift System Optimization	19
Boundary-Layer Profiles	21
COMPARISON OF DATA AND THEORY	23
Aerodynamic Characteristics	23
Boundary-Layer Properties	25
CONCLUSIONS	27
REFERENCES	28





**TWO-DIMENSIONAL WIND TUNNEL TESTS OF A NASA
SUPERCritical AIRFOIL WITH VARIOUS HIGH-LIFT SYSTEMS**

Volume I—Data Analysis

**By E. Omar, T. Zierten, and A. Mahal
The Boeing Company
Commercial Airplane Group**

SUMMARY

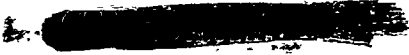
In fulfillment of NASA contract NAS1-10824, "Two-Dimensional Wind Tunnel Tests of a NASA Supercritical Airfoil With Various High-Lift Systems," three high-lift systems for a NASA, 9.3%, blunt-based, supercritical airfoil were designed, fabricated, and wind tunnel tested. In addition, a method furnished by NASA for calculating the viscous flow about two-dimensional multicomponent airfoils was evaluated by comparing its predictions with test data.

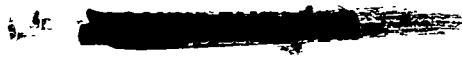
The primary objective of this program was to determine whether high-lift systems derived from supercritical airfoils would have performance comparable to high-lift systems derived from conventional airfoils. The high-lift systems for the supercritical airfoil were designed to achieve maximum lift and consisted of:

- A single-slotted flap
- A double-slotted flap and a leading-edge slat
- A triple-slotted flap and a leading-edge slat

The secondary objective was to produce high-quality two-dimensional data to verify the NASA theoretical method for predicting the flow characteristics about multicomponent airfoils. The data would also serve as a basis for future improvements of the method.

To achieve these objectives, wind tunnel tests were conducted in the Boeing research wind tunnel (BRWT), which is equipped with wall boundary-layer control to ensure two-dimensionality. Tests of the basic supercritical airfoil were conducted at Mach numbers ranging from 0.08 to 0.284. The corresponding Reynolds numbers ranged from 1.1 million to 4.02 million. All high-lift system





tests were conducted at a Mach number of 0.2 and a Reynolds number of 2.83 million. The tests were conducted over sufficient ranges of angle of attack to adequately define the aerodynamic characteristics of each configuration. Tests were conducted for a range of settings of the leading-edge devices and trailing flaps to determine the maximum lift of the high-lift systems. Boundary-layer and wake measurements for comparison with theory were conducted only on the single-slotted flap configuration.

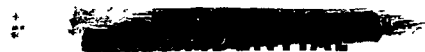
The maximum lift produced by each configuration of the NASA supercritical airfoil is tabulated below along with the trailing-edge flap deflection at which the maximum lift occurred.

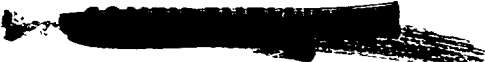
<u>Configuration</u>	<u>Maximum Lift Coefficient</u>	<u>Flap Deflection for Maximum Lift</u>
Basic airfoil	1.73	-
Single-slotted flap	2.79	30°
Double-slotted flap	4.85	29°/50°
Triple-slotted flap	5.5	20°/45°/65°

The maximum lift coefficient produced by the supercritical airfoil is considered excellent compared with conventional airfoils under similar test conditions. The performance of the high-lift configurations of the supercritical airfoil was found to be comparable to that of high-lift configurations of the NACA 23012 airfoil and the Boeing 707 airfoil. Neither the supercritical airfoil contours from which high-lift components were derived, nor the blunt trailing edge (0.01 c thick) had an appreciable effect on high-lift performance.

Test data of configurations having little or no boundary-layer separation were compared with predictions of the analytical method furnished by NASA. The comparisons indicate that the tendency of the NASA method is to:

- Predict lift, pitching moments, and surface pressures reasonably well for single airfoils and airfoils with slotted flaps at low deflection angles
- Underpredict the lift at high angles of attack of airfoils with slotted flaps at high deflection angles
- Overpredict the drag of flapped and unflapped airfoils





INTRODUCTION

A research and development program has been initiated by the National Aeronautics and Space Administration to exploit the characteristics of the NASA supercritical airfoil, which has a transonic drag rise at substantially higher speeds than conventional airfoils. The program includes system studies that would lead to the definition of an advanced-technology transport aircraft and identify areas of needed research. One area of interest has been the evaluation of the high-lift systems that would provide the aircraft with the necessary low-speed capabilities to meet field length and low-speed handling requirements. To determine the high-lift characteristics of the supercritical airfoil, NASA contracted with The Boeing Company to design and test various two-dimensional high-lift systems for a NASA supercritical airfoil having a thickness of 9.3% of its chord. NASA provided the airfoil coordinates and specified that the high-lift systems include a single-slotted flap and a configuration with a double-slotted flap and leading-edge slat. A third high-lift system was recommended by Boeing and consisted of a triple-slotted flap and a leading-edge slat.

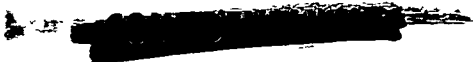
The primary technical objectives of this contract were to:

- Design the high-lift systems for maximum lift conditions
- Evaluate their aerodynamic characteristics through wind-tunnel tests
- Experimentally determine the orientations of airfoil components that will produce the maximum lift
- Compare these high-lift systems with systems designed for conventional airfoils

An additional objective was to make comparisons between experimental data and results of a NASA theoretical method for calculating the viscous flows about multicomponent airfoils.

In accordance with the terms of NASA contract NAS1-10824, this document is submitted as the final technical report. The report consists of two volumes. Volume I contains:

- A discussion of the designs of high-lift systems and optimization procedures
- A discussion of test results
- A comparison of the NASA method with test results



The contents of volume II (NASA CR-2215) consist of:

- A description of the test facilities and models
- A discussion of data acquisition and reduction
- Plots of selected wind tunnel data



SYMBOLS

All geometric airfoil parameters defined below are illustrated in figure 1.

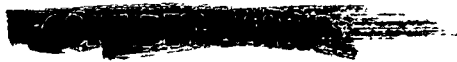
c	airfoil reference chord length, meters
c'	camber-line length of a deployed high-lift system measured from the wing leading edge (0,0) to the trailing edge of the last flap component, meters
c'_f	camber-line length of a deployed trailing-edge flap, meters
c_f	chord length of a retracted flap, meters
$c_{\ell e}$	chord length of a deployed leading-edge device, meters
C_d	section drag coefficient, $C_d = D/q_\infty S$
C_ℓ	section lift coefficient, $C_\ell = L/q_\infty S$
$C_{\ell_{\max}}$	the maximum lift coefficient an airfoil configuration generates as angle of attack is varied
$C_{m_{0.25}}$	section pitching moment coefficient about a moment center located at (0.25c,0), $C_{m_{0.25}} = m/q_\infty S c$
C_p	pressure coefficient, $(P_L - P_\infty)/q_\infty$
$C_{p_{\min}}$	pressure coefficient of airfoil component suction peak
D	drag, newtons
G	slot gap size, meters
H	boundary-layer shape factor, $H = \delta^*/\theta$
L	lift, newtons
L/D	ratio of lift to drag

m	pitching moment, newton-meters
M_∞	freestream Mach number
P_L	local static pressure, newtons per square meter
P_t	freestream total pressure, newtons per square meter
P_∞	freestream static pressure, newtons per square meter
q_∞	freestream dynamic pressure, $q_\infty = \rho_\infty U_\infty^2/2$, newtons per square meter
Re	Reynolds number based on airfoil reference chord length
S	wing area, square meters
T_t	freestream total temperature, °K
U	local velocity, meters per second
U_∞	freestream velocity, meters per second
U_p	local potential velocity based on freestream total pressure and local static pressure, meters per second
x, y	horizontal and vertical Cartesian coordinates, meters
x_0, y_0	location of the leading-edge point of a high-lift component in a deployed position, meters
Δx	airfoil component overlap measured parallel to the chord line of the most forward of two overlapping components, meters
y_t	the elevation (measured from the wing chord line) of the trailing edge of a leading-edge device, meters
α	airfoil angle of attack, degrees
δ_f	trailing-edge flap deflection measured from the wing chord line to the flap component chord line, degrees

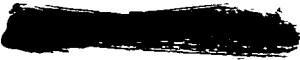


- $\delta_{f_{eq}}$ equivalent plain flap deflection angle (the deflection of a plain flap having the same chord and producing the same potential flow lift as a deployed slotted trailing-edge flap), degrees
- $\delta_{\rho e}$ deflection of a leading-edge device measured from the wing chord line to the device chord line, degrees
- δ^* boundary-layer displacement thickness, meters
- θ boundary-layer momentum thickness, meters
- ρ_{∞} freestream density, kilograms per cubic meter

... ..



Page Intentionally Left Blank



TEST PROGRAM

MODELS

Four configurations were fabricated and tested. These include:

Model A—basic 9.3% chord thick NASA supercritical airfoil

Model B—a 0.295c single-slotted flap configuration

Model C—a configuration with a 0.325c double-slotted flap and a 0.156c leading-edge slat

Model D—a configuration with a 0.325c triple-slotted flap and a 0.155c leading-edge slat

The first three configurations were required by NASA; the fourth was Boeing's recommendation. The four configurations are illustrated in figure 2.

The models were fabricated of steel to a 0.6096 m (24 in.) chord and 0.9144 m (36 in.) span. Ordinates defining the individual airfoil components are presented in volume II.

HIGH-LIFT SYSTEM DESIGN

Constraints

The five primary design constraints required that:

- In their retracted positions, all exposed surfaces of high-lift components must coincide with the basic airfoil contour.
- The retracted flap chords would be 0.325c.
- The slats would retract into the forward 0.15c of the airfoil.
- The cove trailing edge of the main airfoil would be located at 0.825c.
- In their deployed positions, the double- and triple-slotted flaps would extend the airfoil chord by 0.27c and 0.33c, respectively.

- 
- The double-slotted flap would be of the vane-flap type (i.e., having a small forward component and large aft component).

To satisfy the constraints of flap chord and flap extension, chords of $0.15c$ and $0.295c$ were selected for the first and second components of the double-slotted flap, and chords of $0.15c$, $0.235c$, and $0.12c$ were selected for the first, second, and third components of the triple-slotted flap, respectively. The first component of the double- and triple-slotted flaps were designed to be common to both. The aft component of the double-slotted flap was designed to also serve as the single-slotted flap.

To delineate between the two slats, the slat for model C will be referred to as slat 1 while the slat for model D will be referred to as slat 2. An assumption made in designing the slat 1 lower surface was that a segment sealing the slat/wing lower surface while the slat is nested could be rotated into the slat lower surface as the slat is deployed (see fig. 3).

A basic requirement for slat 2 was that in practice it would retract into the wing lower surface. The forward 30% of the flap would be hinged and would fold inside the wing during retraction as shown in figure 3. The aft 70% of the flap would be rigid and would serve as the forward lower surface of the wing when retracted.

Considering the above constraints, aerodynamic contouring was limited to the portions of the wing and flaps presented in heavy lines in figure 4.

Design Conditions

The high-lift systems were designed to achieve maximum lift. Since the generation of lift is limited by the ability of an airfoil upper surface boundary layer to negotiate adverse pressure gradients, the high-lift systems were designed under conditions at which the most severe pressure gradients were anticipated. For the leading-edge slats, this condition occurs just before the airfoil stalls; hence, the design conditions correspond to expected values of maximum lift and the stall angle of attack. For models C and D, maximum lift design conditions of $C_{\ell} = 4.9$ at $\alpha = 16^{\circ}$ and $C_{\ell} = 5.1$ at $\alpha = 16^{\circ}$, respectively, were predicted on the basis of Boeing data.

At high flap deflections, pressure gradients on trailing-edge flaps are most severe at low angles of attack. Hence, a design angle of attack of 0° was selected for the flaps of models C and D. Design deflection angles were selected that produce the highest lift due to flap deflection. From figure 5, an initial equivalent flap deflection of 50° was selected for both the double- and triple-slotted flaps. Equivalent flap deflection ($\delta_{f_{eq}}$) is defined as the deflection of a plain flap having the same chord length and producing the same potential flow lift as a deployed slotted flap.



Design Procedure

The design of the high-lift systems was conducted using potential-flow theory. The slat design conditions were achieved in potential flow by reducing the deflection of the trailing-edge flaps to compensate for viscous effects. Three parameters were used to define the orientations of the slats: deflection angle, slot gap, and elevation of the trailing edge of the slat. From Boeing data, slot gaps of $0.0175c$ and deflections of 50° and 47° were selected for slat 1 and slat 2, respectively. Elevations were selected for the slat trailing edges to give the lowest main-section potential-flow suction peaks. Fixing the orientations of the slats, all unconstrained leading-edge contours were then tailored to reduce leading-edge suction peaks, thereby producing less adverse pressure gradients. The resulting pressure distributions are presented in figures 6 and 7. The final step of the design was to reorient the slats to minimize the main-section suction peaks. In so doing, the local Mach numbers on the slats were not allowed to exceed 1.25. From reference 1, this value was found to be near the point above which shock-induced separation occurs. The resulting slat orientations are listed in table 1.

A similar procedure was used in designing the trailing-edge flaps. For an equivalent flap deflection of 50° , slot gaps, component overlaps, and component deflections were selected for the double- and triple-slotted flaps from Boeing data. Fixing the orientations of the flap components, their unconstrained contours were tailored to produce the potential-flow pressures presented in figures 8 and 9. An equivalent flap deflection series was then selected for each flap, and appropriate slot geometry and component deflections were selected from Boeing data for each equivalent deflection. Representative orientations of each flap are listed in table 1.

The original cove shape (cove 1) for models B, C, and D was designed to allow the flaps to be retracted. Since the NASA theoretical method does not treat separated flows, a second cove shape (cove 2) was designed by NASA to be free of boundary-layer separation. Cove 2 was fabricated by removing material from and adding a fairing to cove 1, as illustrated in figure 10.

EXPERIMENTAL OPTIMIZATION PROCEDURE

Optimizations of the slot geometry and deflection angles of the multislot high-lift systems C and D for $C_{l_{\max}}$ were first conducted for the leading-edge slats and then the trailing-edge flaps. The optimizations were conducted in this sequence since leading-edge boundary-layer conditions have a greater effect on trailing-edge flap performance than trailing-edge boundary-layer conditions have on leading-edge slat performance (i.e., leading-edge conditions at $C_{l_{\max}}$ do not vary greatly with changes in flap effectiveness, as illustrated in fig. 11). The deflection angles of the slats were optimized first,



followed by leading-edge slot optimizations. For the trailing-edge flaps, the combinations of component deflections were first optimized for flap effectiveness at a constant equivalent flap deflection. Then the slots were optimized for $C_{l_{\max}}$ starting with the most forward slot and proceeding aft.

After following this procedure on model C, a second slat optimization was conducted. The improvement in $C_{l_{\max}}$ was found to be less than 0.5%. From the chart in figure 12, it is evident that further optimization would not have been too productive.

TEST FACILITIES

The tests were conducted in the 0.9144 m (36 in.) by 2.438 m (96 in.) Boeing research wind tunnel (BRWT) located at Seattle, Washington. The tunnel was designed specifically for two-dimensional high-lift testing. It has a 12:1 bellmouth contraction ratio and a 6.0960-m (240-in.) long test section. The test section walls are equipped with a blowing boundary-layer-control (BLC) system to ensure two-dimensionality. The locations at which test section BLC is applied are illustrated in figure 13 and appear in figure 14, which also depicts a typical model installation. Figure 13 also shows the location of the self-integrating wake rake used for drag measurements. The wake rake is equipped to traverse both horizontally and vertically. A more detailed description of the BRWT is presented in volume II of this report.

DATA ACQUISITION

The test data acquired included:

- Model forces and moments ($C_l, C_d, C_{m_{0.25c}}$)
- Surface pressures
- Boundary-layer profiles (for model B only)
- Test section conditions (P_t, P_∞, T_t)
- Flow visualizations to determine the locations of flow separation and transition
- Angle of attack

Details of all measurements and corrections applied to the measurements are discussed in volume II. A summary of the test program is presented in table 2.



TEST RESULTS

Wind tunnel tests of the basic supercritical airfoil (model A) were conducted at Mach numbers ranging from 0.08 to 0.284. The corresponding Reynolds numbers ranged from 1.1 million to 4.02 million. Tests of the high-lift systems were all conducted at a Mach number of 0.2 and a Reynolds number of 2.83 million.

Four significant features were considered while analyzing the test results. These were:

- The maximum lift that can be achieved
- The lift increment due to trailing-edge flap deflection
- The minimum drag a configuration generates
- The maximum lift-to-drag ratio (L/D) produced by a configuration

Other features that will be discussed are the pitching moments produced by a configuration and the change in stall angle due to flap deflection. The latter is of importance when applying sectional data to wings with part-span trailing-edge flaps.

In the following discussion of test results, reference to $C_{\ell_{\max}}$ will pertain to the maximum lift that can be sustained. For many of the configurations, the flow was unsteady at $C_{\ell_{\max}}$ causing small but continuous fluctuations in lift. For others, the flow was steady for short periods of time mixed with periods of intermittent stalling. The procedure for defining $C_{\ell_{\max}}$ was to determine the highest angle of attack at which lift could be sustained with no intermittent stalling, then to record a time-averaged value of lift.

SECTIONAL CHARACTERISTICS

Model A

The specific conditions at which the supercritical airfoil was tested are tabulated below. Mach number and Reynolds number both affect the lift and drag of an airfoil. The variations of $C_{\ell_{\max}}$ with Mach number are summarized in figures 15 and 16. Figure 15a shows that $C_{\ell_{\max}}$ reaches a maximum at $M_{\infty} = 0.17$. Below this Mach number, $C_{\ell_{\max}}$ is reduced primarily by Reynolds number effects. Above $M_{\infty} = 0.17$, $C_{\ell_{\max}}$ is reduced by compressibility effects. Figure 15 shows that sonic

M_∞	$Re \times 10^{-6}$
0.08	1.1
0.142	2.01
0.201	2.83
0.259	3.66
0.284	4.02

velocity exists on the airfoil leading edge at $C_{l_{\max}}$ for $M_\infty = 0.225$, and, for higher Mach numbers, a region of supersonic flow exists on the airfoil leading edge.

The composite effects of Mach number and Reynolds number on $C_{l_{\max}}$ are demonstrated in figure 16. Compressibility effects are evident throughout the test Mach number range. The effects are much greater, however, for Mach numbers above 0.2. Also shown in figure 16 are experimental curves of $C_{l_{\max}}$ versus Reynolds numbers for a Boeing airfoil and the NACA 23012 airfoil (ref. 2) and theoretical predictions of $C_{l_{\max}}$ versus Reynolds number for model A. All three curves show the same trends and indicate that the test data of model A can be readily extrapolated to full-scale Reynolds numbers.

Variations of freestream Mach number had little effect on minimum drag, as shown in figure 17a, except at the lowest test Mach number where $C_{d_{\min}}$ was found to be considerably lower. The $(L/D)_{\max}$ was found to increase continuously with increasing Mach number, with an exceptionally large increase between Mach numbers of 0.14 and 0.2 (see fig. 17b).

The sectional aerodynamic characteristics of model A are presented in figure 18 for $M_\infty = 0.2$ and $Re = 2.83 \times 10^6$. Also shown in figure 18 is the effect of boundary-layer trip strips. The trips tended to decrease lift and increase drag and pitching moments due to an increase in turbulent boundary-layer growth. The increase in drag is substantiated by predictions by both NASA and Boeing theoretical methods. The experimental drag increment due to trips at zero angle of attack is $\Delta C_d = 0.001$. The NASA and Boeing theories predicted $\Delta C_d = 0.003$ and $\Delta C_d = 0.0022$, respectively.

Model B

The single-slotted flap was tested for flap deflections of $\delta_f = 20^\circ, 30^\circ, 40^\circ$, and 50° . The corresponding equivalent flap deflections were $20^\circ, 29^\circ, 38.5^\circ$, and 47.3° , respectively. At $\delta_f = 20^\circ$, the slot geometry was optimized for $C_{l_{\max}}$ and profiles through the confluent boundary layer were obtained at angles of attack of $0^\circ, 4^\circ$, and 8° . The slot geometry was optimized using cove 1 while cove 2 was used for measuring the boundary-layer profiles. Slot optimization is discussed under "High-Lift System Optimization." The boundary-layer measurements are discussed under "Boundary-Layer Profiles."

The section characteristics for the four flap deflections are presented in figure 19. At $\delta_f = 20^\circ$ data are presented for both cove 1 and the faired cove 2. The configuration with cove 2 has a 0.04 lower potential-flow lift than that with cove 1. Yet, the reduced separation due to the cove fairing enabled the configuration with cove 2 to obtain slightly higher measured lifts and stall angle of attack. The improvement amounted to 0.4° in stall angle of attack with a corresponding $C_{l_{\max}}$ increase of 0.03. Figure 19 shows that, as flap deflection was increased, the lift at low angles of attack continually increased through $\delta_f = 50^\circ$, whereas $C_{l_{\max}}$ reached a maximum at $\delta_f = 30^\circ$. For all deflection angles, stall occurred abruptly. Pitching moments did not vary greatly with flap deflection. Excessive drag occurred at $\delta_f = 40^\circ$ and 50° due to flap separation.

Flow visualizations by use of china clay indicated that:

- The flap was free of separation at $\delta_f = 20^\circ$
- At $\delta_f = 30^\circ, 40^\circ,$ and 50° , boundary-layer separation was observed at $0.08c, 0.167c,$ and $0.193c$ forward of the flap trailing edge, respectively.

The above separation point measurements were made along the flap upper surface.

Model C

The double-slotted flap was tested at equivalent-flap deflections ($\delta_{f_{\text{eq}}}$) of $0^\circ, 12^\circ, 30^\circ, 44^\circ,$ and 49° .

In addition to the equivalent-flap deflection series, the following studies were conducted with model C.

- Optimization of the leading-edge slat orientation for $C_{l_{\max}}$ at $\delta_{f_{\text{eq}}} = 44^\circ$
- Optimization of trailing-edge flap component deflection angles for flap effectiveness at $\delta_{f_{\text{eq}}} = 44^\circ$
- Optimization of trailing-edge slot geometry for $C_{l_{\max}}$ at $\delta_{f_{\text{eq}}} = 44^\circ$
- A comparison of a typical takeoff flap setting with a near-optimum takeoff flap setting.

The results of the optimizations are presented in the section, "High-Lift System Optimization," of this report.

The sectional characteristics of model C are presented in figure 20. With increasing flap deflection, the lift at zero angle of attack was found to increase continuously to $\delta_{f_{eq}} = 49^\circ$. Intermittent stalling of the trailing-edge flaps was observed for the 49° configuration; therefore, the 44° configuration was considered best. The 44° configuration also produced the maximum $C_{l_{max}}$. The stall of model C was not abrupt as was the case with model B, which had no leading-edge device. The stall angle of attack decreased from 26.7° with 0° flap setting to 12° with 44° flap setting. This is a net spread of 14.7° as compared to a maximum stall angle spread of 9° for model B. Just as with model B, maximum L/D deteriorated rapidly for equivalent deflections past 30° .

Flow visualizations of the double-slotted trailing-edge flaps at zero angle of attack revealed:

- No flap boundary-layer separation occurred at $\delta_{f_{eq}} = 12^\circ$ and 30° .
- Separation occurred 0.02c forward of the vane trailing edge at $\delta_{f_{eq}} = 44^\circ$. No appreciable separation was found on the aft component.
- Extreme separation occurred on the flap components for $\delta_{f_{eq}} = 49^\circ$. Two deflection combinations ($30^\circ/57^\circ$ and $35^\circ/55.5^\circ$) were investigated. For $\delta_f = 30^\circ/57^\circ$, no appreciable separation occurred on the vane, but the flow was separated over the last 30% of the aft component. For $\delta_f = 35^\circ/55.5^\circ$, no separation was visible on the aft component; however, the flow was separated over the last 25% of the vane. Both flaps produced the same level of flap effectiveness, but the $30^\circ/57^\circ$ setting produced a higher $C_{l_{max}}$. Severe intermittent stalling of the flaps was observed for the $35^\circ/55.5^\circ$ setting.

The $\delta_{f_{eq}} = 12^\circ$ configuration in figure 20 was not optimized for $C_{l_{max}}$. Actually, it represented a practical takeoff flap setting that could be achieved readily by a simplified actuator mechanism. To demonstrate the penalties that may occur by compromising the intermediate deflection settings to achieve an optimum maximum deflection setting, a near-optimum takeoff setting was tested. The two takeoff settings are compared in figure 21. An increase in $C_{l_{max}}$ of 0.5 (or 13%) was achieved with the improved setting. This $C_{l_{max}}$ improvement was accompanied by degradation of $(L/D)_{max}$ from 87 to 77 and a 0.1 increase in $C_{m_{0.25c}}$.

Model D

The triple-slotted flap was tested at equivalent deflection angles ($\delta_{f_{eq}}$) of 0° , 16° , 46° , and 53° . The slat deflection and leading-edge slot geometry were optimized for $C_{l_{max}}$ at $\delta_{f_{eq}} = 46^\circ$. The combination of trailing-edge flap component deflections was optimized for flap effectiveness at $\delta_{f_{eq}} = 46^\circ$.



The sectional characteristics are presented in figure 22. Flap effectiveness continuously increased up to $\delta_{f_{eq}} = 46^\circ$. No appreciable increase in lift was achieved by increasing the equivalent flap deflection to 53° ; however, the drag increased significantly. The spread in stall angle of attack from trailing-edge flaps up to maximum flap deflection is only 8° for the triple-slotted flap, as compared to 9° for model B and 14.7° for model C. In the case of model C, the slat deflection was nearer an optimum setting for flaps up than with model D; hence, the stall of model D with flaps up was premature.

Flow visualizations indicated no flow separation except at $\delta_{f_{eq}} = 53^\circ$. At this angle, the flow was separated over the last 20% of the second flap component

COMPARISON OF HIGH-LIFT SYSTEMS

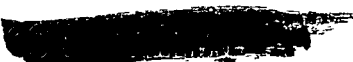
The performance of models B, C, and D have been compared with each other and with high-lift systems designed for conventional airfoils. These include high-lift configurations of a Boeing 707 10% thick airfoil, developed through Boeing independent research efforts, and high-lift configurations of the NACA 23012 airfoil (ref. 2). The high-lift systems for the Boeing 707 airfoil were designed without constraint and represent highly idealized configurations. Models B, C, and D, on the other hand, were designed to represent practical configurations. This basic difference in design philosophy is reflected primarily in comparisons of lift efficiency (experimental lift/potential-flow lift) and drag. Comparisons have been made on the basis of lift, drag, and pitching moments and are discussed below. In general, models B, C, and D have been found to compare favorably with the other high-lift systems.

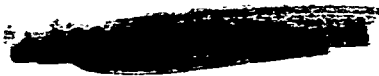
Lift

Two significant lift features were considered. These were:

- The maximum lift that can be achieved
- The lift increment due to trailing-edge flap deflection

The maximum lift of model B is compared with that of a single-slotted flap configuration of the NACA 23012 airfoil (ref. 2) for a range of flap deflections. Due to differences in flap chord, chord extension (c'/c), and test Reynolds numbers, no conclusions can be drawn concerning the absolute lifts of the two systems. A point of interest, however, is that the maximum $C_{l_{max}}$ occurs at a lower deflection angle for the aft-cambered model B flap than for the forward-cambered flap of the NACA 23012 airfoil (see fig. 23). This could be attributed to the characteristics of the pressure recovery produced by aft-cambered flaps.





The maximum lifts of models C and D are compared with those of double- and triple-slotted configurations of the Boeing 707 airfoil in figure 24. Although the chords of the high-lift devices of model D and the Boeing triple-slotted configuration are similar, model D produced a maximum lift coefficient that is 0.57 higher. In comparing maximum lifts of model C with those of the Boeing double-slotted configuration it should be noted that they have leading-edge-device chords of 0.156c versus 0.1c, flap chords of 0.35c versus 0.29c, and flap extensions of 0.27c versus 0.22c, respectively. In spite of the larger high-lift devices of model C, it produced a maximum lift coefficient that was higher by only 0.31.

The experimental versus potential-flow lifts at $\alpha = 0^\circ$ produced by models B, C, and D are compared with lifts of the high-lift configurations (i e., single-, double-, and triple-slotted trailing-edge flap and a 0.1c leading-edge flap) of the Boeing 707 airfoil in figure 25. Zero angle of attack is near the angle of zero lift with trailing-edge flaps retracted; hence, $C_{l_{\alpha=0}}$ closely represents the lift increment due to trailing-edge flap deflection. From figure 25, the maximum $C_{l_{\alpha=0}}$ produced by models B, C, and D are 2.23, 3.92, and 4.48, respectively, as compared to values of 2.42, 3.69, and 3.82 produced by the single-, double-, and triple-slotted flap configurations of the Boeing 707 airfoils. By removing the effects of flap extension and normalizing data in figure 25 to a common flap chord ratio, it can be seen (fig. 26) that lift due to flap deflection increases continuously to $\delta_{f_{eq}} = 50^\circ$ for the double- and triple-slotted flaps. Model B was found to reach its limit at 44° , whereas the single-slotted flap configuration of the 707 airfoil reached its limit at 37° .

Drag

Drag envelopes of models B, C, and D are compared in figure 27. In general, model C produced the best drag envelope. From $C_D = 1.4$ to $C_D = 3.0$, L/D 's of 90 or better are achieved. Model B produced an L/D of approximately 100; however, it occurred at a C_D of less than 1.0. The drag polars of model B and a single-slotted flap configuration of the NACA 23012 airfoil (ref. 2) for $\delta_f = 20^\circ$ are compared in figure 28. Over the C_D range from 0.6 to 2.2, the maximum difference between the two drag polars is less than 0.002.

Pitching Moments

The pitching moments of models B, C, and D and of the high-lift systems of the Boeing 707 airfoil have been found to compare well, as shown in figure 29. The pitching moments presented have been adjusted to remove the effects of flap extension.



COMPARISON OF LEADING-EDGE SLATS

Additional testing of the triple-slotted flap was conducted with slat 1 and the modified main-section leading edge from model C. The tests were conducted with the basic trailing edge and for $\delta_{f_{eq}} = 16^\circ$ and 46° . The aerodynamic characteristics are compared with those of model D in figure 30. Slat 1 was found to produce a slightly higher $C_{l_{max}}$ for the flaps-up case than slat 2. At $\delta_{f_{eq}} = 16^\circ$ and 46° , slat 2 produced greater maximum lifts than slat 1 by 0.5 and 0.17, respectively. Slat 1 gave consistently lower lifts than slat 2 at all angles of attack below stall. The potential-flow lift levels shown in figure 30 for the trailing-edge flaps nested cases indicate that the experimental lift differences at low angles of attack is a potential-flow difference, not a viscous effect.

Slat 1 was found to produce higher drag than slat 2 at low angles of attack and less drag at high angles of attack. As a result, slat 1 produced consistently higher values of $(L/D)_{max}$.

HIGH-LIFT SYSTEM OPTIMIZATION

Leading-Edge Slats

Following the experimental optimization procedure outlined earlier in this report for model C, the slat deflection was optimized with a fixed slot gap of $0.0175c$. A slat deflection of 45° was selected on the basis of preliminary data, and the slot geometry (i.e., position of the slat trailing edge) was optimized. As indicated in figure 31, the slot optimization produced an increment in $C_{l_{max}}$ of 0.11. The optimum slot gap was found to be $0.035c$.

After optimizing the trailing-edge flap, a second slat optimization was conducted. For a slot gap of $0.035c$, an optimum slat deflection of 50° was selected and the slot geometry was again optimized. The optimization again produced a slot gap of $0.035c$ and an increment in $C_{l_{max}}$ of only 0.04. Furthermore, the $C_{l_{max}}$ of 4.85 produced with $\delta_{\rho_e} = 50^\circ$ was only 0.02 higher than the $C_{l_{max}}$ produced with $\delta_{\rho_e} = 45^\circ$. Hence, further optimization was not conducted.

Contours of slat trailing-edge position for constant $C_{l_{max}}$ for the two optimizations are presented in figure 32. Although an optimum slot gap of $0.035c$ was found from both optimizations, the elevation of the slat trailing edge varied from $y_t = 0.0125c$ at $\delta_{\rho_e} = 45^\circ$ to $y_t = -0.0015c$ at $\delta_{\rho_e} = 50^\circ$.

Only one leading-edge optimization was conducted for model D. The design slat deflection (44°) was found to produce the highest $C_{l_{max}}$ at a constant slot gap of $0.0175c$ (fig. 33). For that deflection, the slot optimization produced an increment in $C_{l_{max}}$ of 0.1. The optimum slot gap was found



to be $0.025c$ as compared to $0.035c$ for model C. The optimum elevation of the slat trailing edge of model D was found to be $0.033c$. Contour plots of $C_{l_{\max}}$ for slat 2 are presented in figure 34.

The leading-edge slot geometry for highest $C_{l_{\max}}$ was found not to coincide with the slot geometry for lowest drag. For model C, the slot geometry that produced the highest $C_{l_{\max}}$ produced a $C_{d_{\min}}$ that was 0.005 higher, a $C_{l_{\max}}$ that was 0.11 higher, and a $(L/D)_{\max}$ that was 6 points lower than the $C_{d_{\min}}$, $C_{l_{\max}}$, and $(L/D)_{\max}$ produced by the setting that had the lowest $C_{d_{\min}}$. For model D, the slot geometry for highest $C_{l_{\max}}$ produced a minimum drag that was only 0.001 higher than the lowest minimum drag achieved. For both models C and D, the minimum drag was found to decrease and $(L/D)_{\max}$ was found to increase with decreasing slat deflections over the range of deflections investigated.

The leading-edge optimizations were found to have little effect on pitching moments.

Trailing-Edge Flaps

The trailing-edge optimization of model B consisted of optimizing the slot geometry for $C_{l_{\max}}$ at $\delta_f = 20^\circ$. The optimization was conducted with the vane of the double-slotted flap nested in the wing cove to provide a smooth fairing as illustrated in figure 35. The optimum slot gap and component overlap (Δx) were found to be approximately $0.02c$ and $0.0c$, respectively. As shown in figure 35, the increase in $C_{l_{\max}}$ over the design position amounted to 0.02 or less than 1% .

The trailing-edge flap of model C was optimized at an equivalent flap deflection of 44° . Past experience has indicated that the higher the lift increment due to deflection of a multislot flap, the higher the achievable $C_{l_{\max}}$. Hence, the first step in the optimization of the double-slotted flaps was to optimize the combination of flap component deflections for lift at $\alpha = 0^\circ$. The variation of $C_{l_{\alpha=0}}$ and $C_{d_{\min}}$ with varying deflection combinations are shown in figure 36. Although the design deflection combination had the best performance, the flow about the configuration had a tendency to be unsteady at angles of attack above 4° . To avoid this characteristic, a combination having a vane deflection of 28.5° , as opposed to the design value of 30° , was selected for conducting the slot optimizations. The forward slot was optimized first, followed by the rear slot optimization. $C_{l_{\max}}$ was found to be more sensitive to forward slot geometry changes than to changes in the rear slot. This is demonstrated in figure 37. The figure shows that the small movement of the vane leading edge from the design position to the optimum position produced an increment in $C_{l_{\max}}$ of 0.04 , while the larger movement of the aft component leading edge from the design position only yielded a 0.02 increase in $C_{l_{\max}}$. The optimum forward slot gap and overlap were found to be $0.011c$ and $-0.005c$, respectively. The second slot gap and overlap were found to be $0.024c$ and $0.01c$ as opposed to the design values of $0.017c$ and $0.0c$, respectively.



A complete optimization of the triple-slotted flap was not conducted. At an equivalent flap deflection of 46° , the flap component deflection combinations were varied. First, the vane deflection was varied and the potential-flow lift changes were compensated for by deflecting the mid and aft components as a unit. Then, holding the vane deflection constant, the combination of mid and aft component deflections was varied. In both cases, the design deflection combinations exhibited the best $C_{l_{\alpha=0}}$, as shown in figure 38.

The slot geometry studies conducted on the triple-slotted flap consisted of investigating the effects of first-component overlap, followed by tests of several combinations of second and third slot geometries. None of the latter combinations produced any significant increases in $C_{l_{\max}}$. The effects of first-component overlap are illustrated in figure 39. Reducing the overlap from the design value of $-0.004c$ to $-0.0105c$ resulted in a $C_{l_{\max}}$ increase of 0.12 or about 2%.

Unlike the leading-edge optimum $C_{l_{\max}}$ setting, the optimum trailing-edge settings for $C_{l_{\max}}$, in most cases, also produce the least drag and highest $(L/D)_{\max}$. Pitching moments did not significantly vary during the trailing-edge optimizations as long as the flap extension was not appreciably changed.

BOUNDARY-LAYER PROFILES

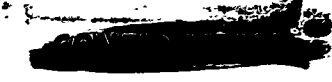
Boundary-layer measurements were taken at 11 stations on the upper and lower surfaces of model B, as illustrated in figure 40. The measurements were taken at angles of attack of 0° , 4° , and 8° . Flow visualizations indicated incipient separation in the cove at $\alpha = 0^\circ$ and definite cove separation at negative angles of attack. The boundary layer separated from the main-section upper surface (i.e., the wing stalled) at 8.5° . The single-slotted flap was deflected to 20° and had a slot gap of $0.02c$ and an overlap of $0.01c$.

The boundary-layer measurements revealed that:

- The flap boundary layer was relatively insensitive to angle-of-attack changes, whereas, the main-section wake size increased with angle of attack.
- A potential core separating the main-section wake from the flap boundary layer was present at all angles of attack.

These traits are demonstrated in figure 41. The profiles measured at the cove and flap trailing edges show that the slot profile is unchanged between $\alpha = 0^\circ$ and $\alpha = 8^\circ$ as is the boundary layer at the flap trailing edge. The principal changes are in the main-section upper surface boundary layer and in the main-section wake.





The complete set of measured profiles is presented in volume II of this report. Boundary-layer parameters, including displacement thickness, momentum thickness, and shape factor, have been calculated from the measured profiles. These are discussed under "Boundary-Layer Properties" in this volume. Drag values calculated from the measured profiles using the Squire-Young formula compare well with drag measurements via integrating wake rake, as shown in figure 46



COMPARISON OF DATA AND THEORY

A secondary objective of this program was to analyze models A, B, C, and D using a method furnished by NASA and compare the results with test data. In brief, the NASA method consists of iterating through potential-flow and boundary-layer calculations until the forces on an airfoil converge. The potential-flow calculations are accomplished in the usual manner of representing the airfoil contour by distributed vortex singularities and then solving for the vortex strengths to satisfy nonlinear boundary conditions on the airfoil surfaces. Viscous flow calculations are accomplished through integral solutions to the laminar, turbulent, and confluent boundary-layer equations. The calculations are applicable to airfoils having no boundary-layer separation.

The method was developed for NASA under contract NAS1-9143 (ref. 3). Modifications to the method have been made by NASA. The results of both the original and modified methods are discussed below.

AERODYNAMIC CHARACTERISTICS

Model A

Theoretical predictions of the performance of the NASA supercritical airfoil are compared with the experimental measurements in figure 42. The drag predictions by the original NASA method (ref. 3) are an order of magnitude higher than the measured drag, hence, are not shown. The original method predicted the lift and pitching moments reasonably well at the lowest angles of attack, but the predictions grow progressively worse as angle of attack is increased. The modified method predicted the lift and pitching moments well over most of the angle-of-attack range investigated but not the drag. The lift near $C_{l_{\max}}$ was overpredicted, as would be expected, since the method is only applicable when there is no boundary-layer separation. The curves of lift, drag, and pitching moments tend to be rotated relative to the corresponding measured curves. The predicted curves cross the measured curves at a lift of approximately 1.3.

The pressure distributions calculated by the NASA methods are compared with experimental pressures in figures 43 and 44 for angles of attack of 0° and 8° . At both angles of attack, the agreement between experiment and theory is good over most of the chord length. The original method was deficient in predicting the leading and trailing-edge pressures at $\alpha = 0^\circ$ and the entire upper surface pressure distribution at $\alpha = 8^\circ$. The modified method was only deficient in predicting the leading-edge pressures at $\alpha = 0^\circ$.

The measured aerodynamic characteristics of model A with leading-edge slat 1 are compared with predictions by the modified NASA method in figure 45. The predictions agree reasonably well



with experiment only over the intermediate range of angle of attack. At low angles of attack, flow visualizations showed boundary-layer separation from the slat lower surface, which explains the disparity between theory and experiment below $\alpha = 8^\circ$.

Model B

The sectional characteristics of model B predicted by the NASA methods have been compared with experiments for flap deflections of 20° , 30° , and 40° in figures 46 through 49. In figure 46, drag values calculated by applying the Squire-Young formula to the measured boundary-layer profiles are presented in addition to the usual wake drag measurements.

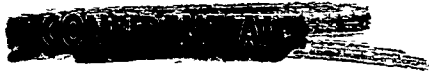
Through china clay visualizations, boundary-layer separation was observed on the model B flap at all deflections except $\delta_f = 20^\circ$. Evidence of lower surface cove separation was observed at $\delta_f = 20^\circ$ for angles of attack below $\alpha = 0^\circ$, and, of course, separation is always present for the sharp-cornered cove used at $\delta_f = 30^\circ$ and 40° . Since the NASA method is applicable only in the absence of boundary-layer separation, only the comparison for $\delta_f = 20^\circ$ serves as a true evaluation of their merits. For that configuration, the original NASA method underpredicted lift and overpredicted drag and pitching moments. The predicted drag values again were an order of magnitude higher than the measured values, hence, were not presented in figure 46. The modified NASA method predicted lift and pitching moments reasonably well but overpredicted the drag.

The experimental and theoretical pressure distributions at $\delta_f = 20^\circ$ and $\alpha = 0^\circ$ are presented in figure 47. The modified NASA method predicted the pressures reasonably well. The greatest discrepancy was in the prediction of the flap suction peak. The modified method overpredicted it by 0.2. The original method predicted the main section pressures reasonably well but was deficient in predicting the flap pressures.

The performance of model B with the flap deflected to 30° and 40° was only predicted using the modified NASA method. The predictions are compared with experiment in figures 48 and 49. In both cases, the method overpredicted the lift and underpredicted the pitching moments. At $\delta_f = 30^\circ$, the drag was overpredicted while at $\delta_f = 40^\circ$ the drag level appears reasonable.

Multislotted Airfoils

The sectional characteristics predicted by the NASA methods of three multislotted configurations have been compared with experiment in figures 50, 51, and 52. The first two configurations consist of models C and D without leading-edge slats and with flaps at deflections of $\delta_{f_{eq}} = 13^\circ$ and 16° , respectively. The third configuration is model C with the flaps at an intermediate deflection ($\delta_{f_{eq}} = 30^\circ$) where there is no separation on the flap components.



The comparison in figure 50 for model C without a leading-edge slat shows that the modified NASA method accurately predicted pitching moments, slightly underpredicted lift, and overpredicted drag. The original method grossly underpredicted lift and overpredicted drag and pitching moments.

Figure 51 shows that the modified method predicted the performance of model D with no leading-edge slat reasonably well. The pitching moments were accurately predicted, the lift was slightly underpredicted, and the drag was overpredicted. The modified method predicted the performance of model C at $\delta_{f_{eq}} = 30^\circ$ well for low angles of attack, as shown in figure 52. At higher angles of attack, the lift was underpredicted, while the drag and pitching moments were overpredicted.

BOUNDARY-LAYER PROPERTIES

Boundary-layer parameters (i.e., displacement thickness δ^* , momentum thickness θ , and shape factor H) calculated from the measured boundary-layer profiles are compared with parameters calculated via the modified NASA method in figures 53, 54, and 55. The boundary-layer properties presented in figure 53 are for the wing lower surface in the region of the cove. The method slightly underpredicted the momentum thickness and grossly underpredicted the displacement thickness. As a result, the experimental and theoretical shape factors are in gross disagreement. The extremely high experimental shape factors at $x/c = 0.65$ were substantiated by flow visualizations that indicated separation on the cove at $\alpha = 0^\circ$.

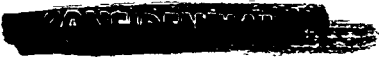
The predicted boundary-layer parameter on the wing upper surface and through the confluent boundary layer are compared with experiment in figures 54 and 55. The NASA method only calculates the momentum thickness of the flap boundary layer when performing confluent boundary-layer calculations. The predicted values of momentum thickness of the wing and flap upper surfaces agree reasonably well with experiment, as shown in figure 54. The flap trailing-edge momentum thickness is underpredicted at $\alpha = 0^\circ$, while the momentum thickness over the aft 50% of the flap is overpredicted at $\alpha = 4^\circ$ and 8° . The predicted displacement thickness is compared with experiment in figure 55. At angles of attack of 0° and 4° the displacement thickness is overpredicted over most of the flap and underpredicted at the flap trailing edge. At 8° angle of attack, the displacement thickness is predicted with an accuracy of $\pm 10\%$ over the forward 80% of the flap but is grossly underpredicted at the flap trailing edge.

Also shown in figure 55 are the locations of flap boundary-layer transition determined by flow visualization. The visualizations reveal that the boundary layer is laminar over the forward 40% of the flap, whereas, the NASA method assumes the flap boundary layer to be turbulent from the slot exit. Another point of interest is the discontinuous nature of the predicted displacement thickness curves. The discontinuities occurring at $x/c = 1.082$, 1.064 , and 1.048 for angles of attack of 0° , 4° , and 8° , respectively, indicate the points at which the NASA method predicts the confluence of the



flap boundary layer and the main-section wake. The measured boundary-layer profiles, on the other hand, showed that a potential core separating the flap boundary layer from the main-section wake existed all the way to the flap trailing edge at all angles of attack.

The measured boundary-layer profiles are compared with predictions by the NASA methods in figure 56. Over most of the profiles, the predictions by the modified method are within $\pm 10\%$ of the measured profiles. The modified method somewhat overpredicted the velocities at the flap suction peak (station 7 in fig 56), the growth of the flap boundary layer, and the thickness of the entire confluent boundary layer. The original method did not predict the profiles well. The velocities below the wake center were mostly overpredicted, while the velocities above the wake center were mostly underpredicted. The boundary-layer thickness was also overpredicted.



CONCLUSIONS

On the basis of data obtained from the contract test program, the following conclusions have been drawn:

- High-lift components derived from a supercritical blunt-based airfoil perform as well as those derived from conventional airfoils.
- For configurations having no boundary-layer separation, the original NASA method consistently underpredicts the lift and overpredicts drag and pitching moments. The modified NASA method predicts lift and pitching moments reasonably well but overpredicts the drag.



REFERENCES

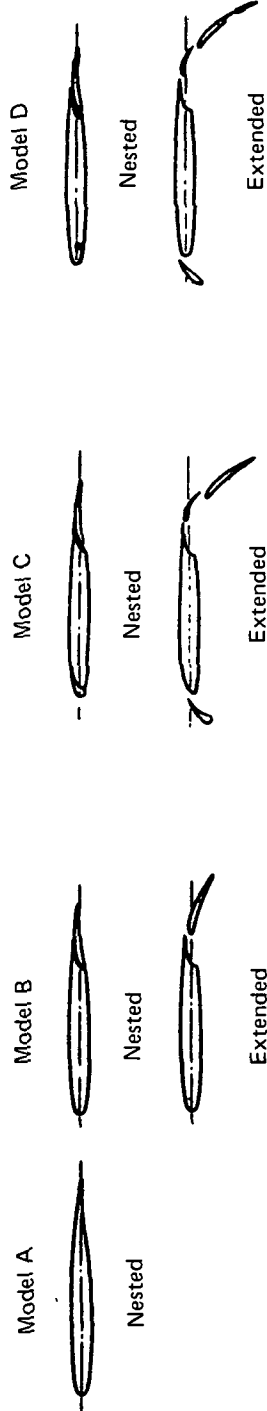
1. Pearcey, H. H.; and Osborne, J.: Some Problems and Features of Transonic Aerodynamics. ICAS paper 70-14, September 1970.
2. Wenzinger, Carl J.; and Harris, Thomas A.: Wind-Tunnel Investigation of an NACA 23012 Airfoil With Various Arrangements of Slotted Flap. NACA report 664, 1939.
3. Stevens, W. A.; Goradia, S. H.; and Braden, J. A.: Mathematical Model for Two-Dimensional Multicomponent Airfoils in Viscous Flow. NASA CR-1843, July 1971.

TABLE 1.—TAKEOFF AND LANDING DESIGN ORIENTATIONS OF HIGH-LIFT SYSTEMS OF MODELS B, C, AND D

Conditions	Takeoff			Landing			v_t/c
	δ_f , deg	G/c	$\Delta x/c$	δ_f , deg	G/c	$\Delta x/c$	
Single-slotted flap	20	0.029	0	—	—	—	—
Double-slotted flap	5/15	0.033/0.017	0/0	30/50	0.01/0.017	-0.004/0	—
Triple-slotted flap	—	—	—	20/45/65	0.016/0.028/0.009	-0.004/0/0	—
Slat 1	—	—	—	47	0.0175	—	0.022
Slat 2	—	—	—	44	0.0175	—	0.031

TABLE 2.—SUMMARY OF TEST PROGRAM

Model	Parameter						Recorded data				
	Angle of attack	Slat deflection	Trailing edge flap deflection	Slot geometry	Freestream Mach number	Trip strips	Model forces, C_D, C_L, C_m	Surface pressures	Boundary-layer measurements	Flow visualization	Tunnel conditions
A	X	-	-	-	X	X	X	-	-	X	X
B	X	-	X	X	-	-	X	X	X	X	X
C	X	X	X	X	-	-	X	X	-	X	X
D	X	X	X	X	-	-	X	X	-	X	X



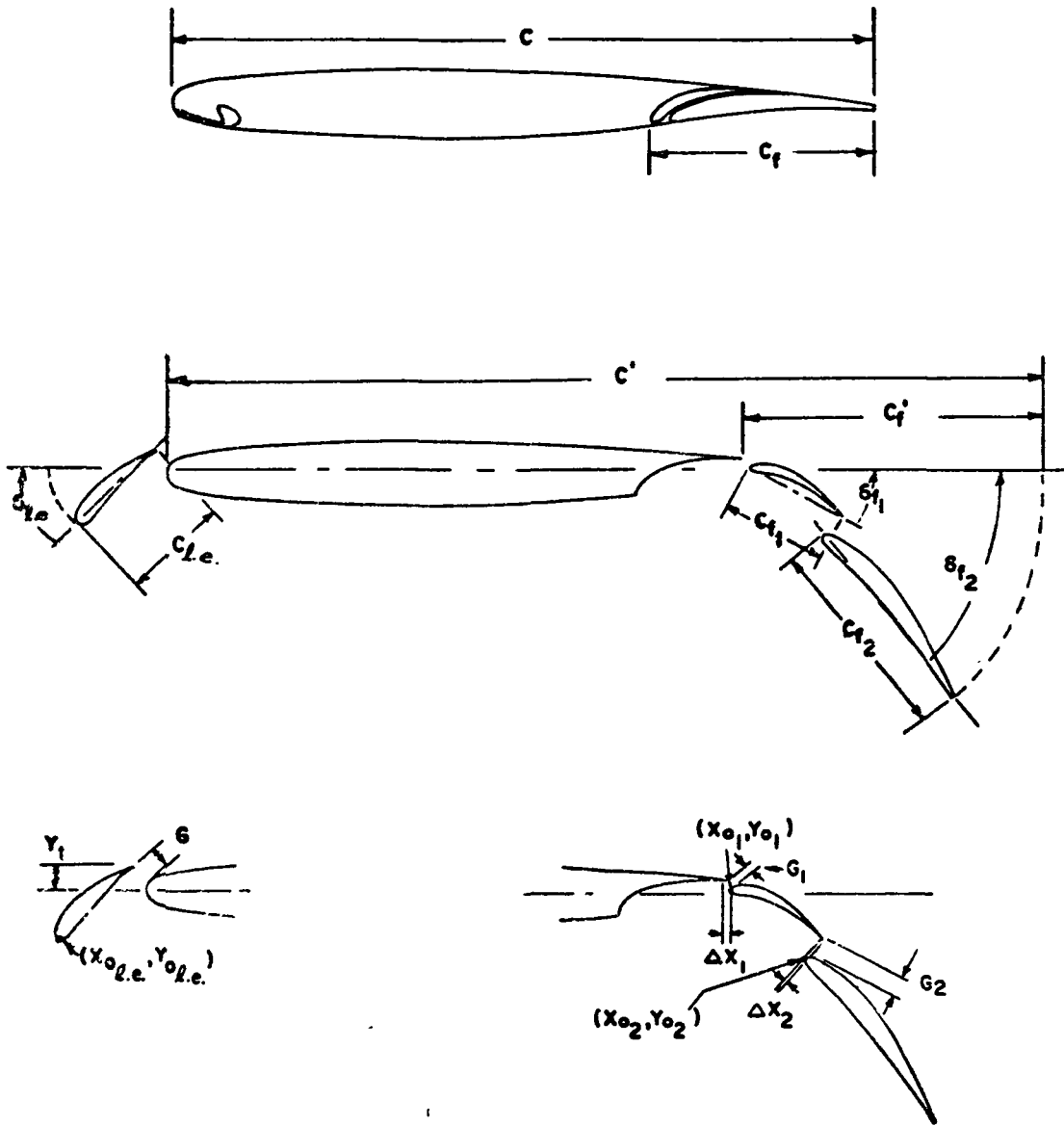


FIGURE 1.—GEOMETRIC AIRFOIL PARAMETERS

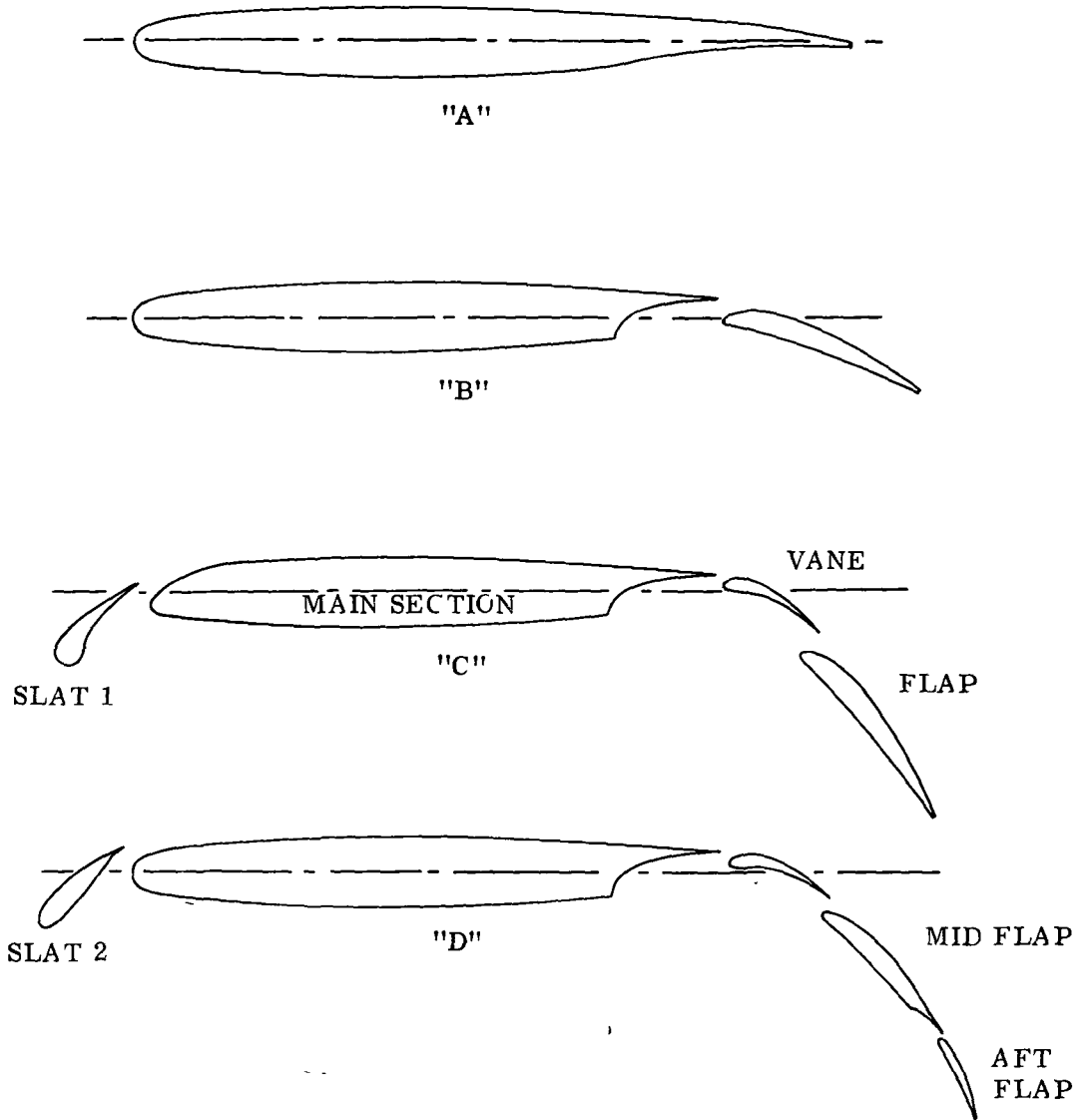


FIGURE 2.—WIND TUNNEL MODEL SECTIONS

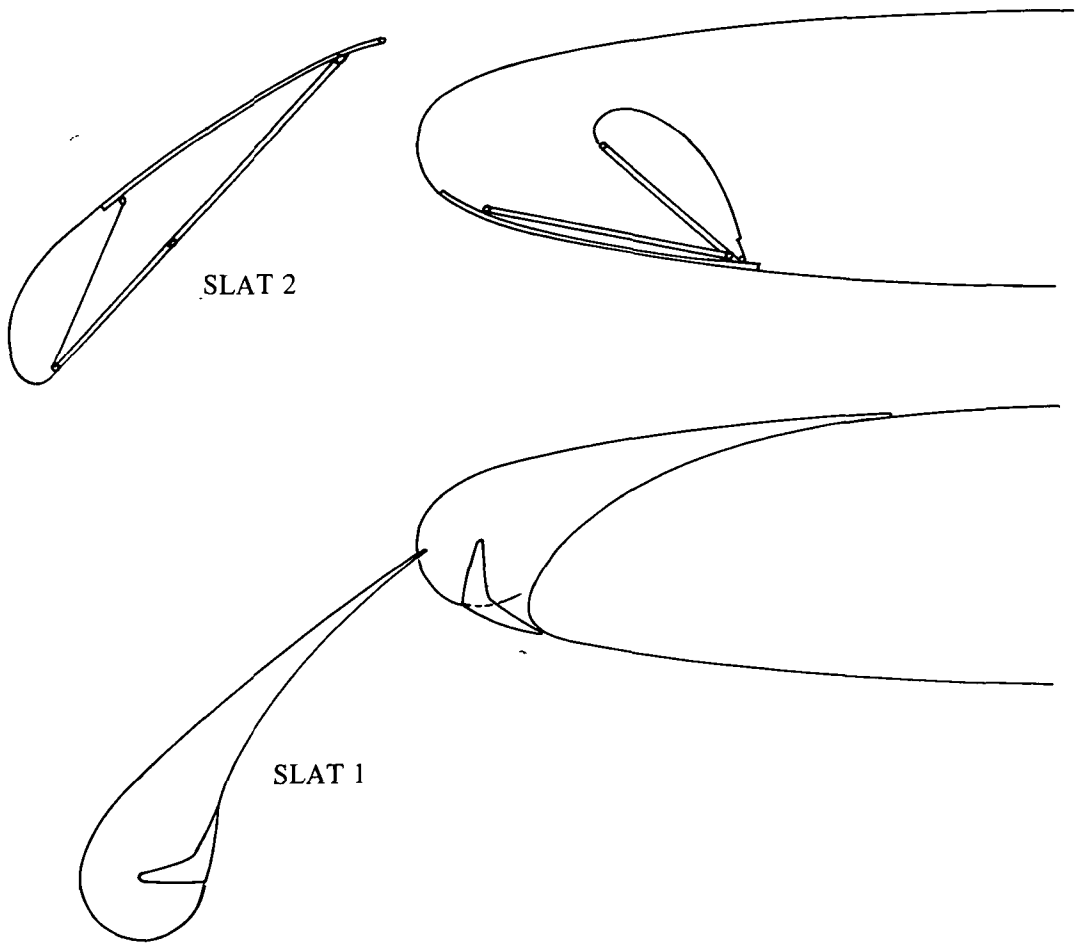
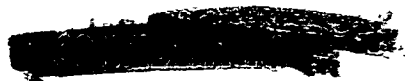


FIGURE 3.—NESTING OF LEADING-EDGE DEVICES



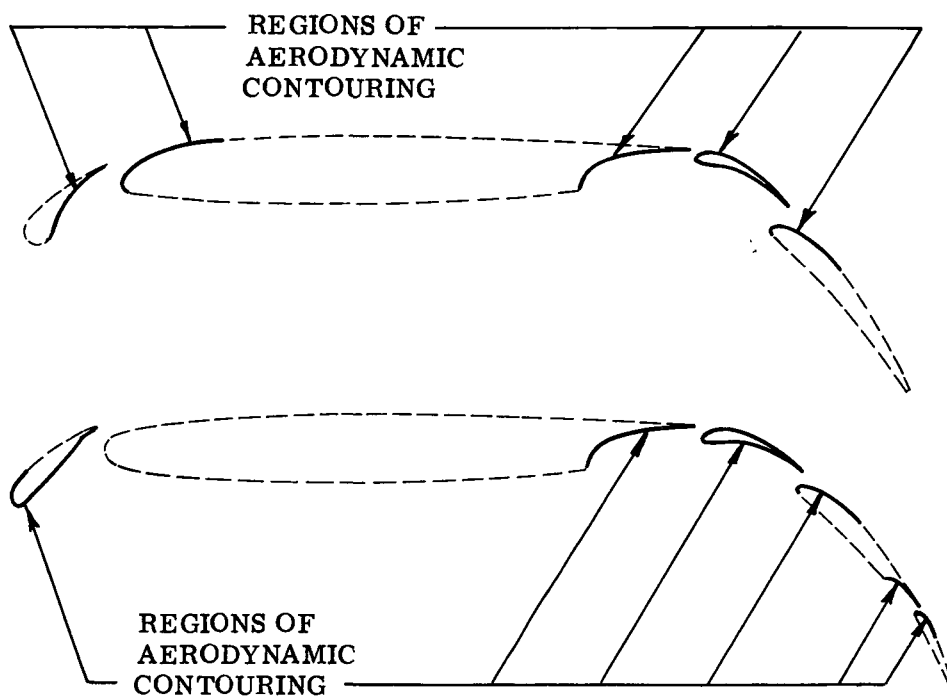


FIGURE 4.—REGIONS OF HIGH-LIFT COMPONENTS THAT WERE AERODYNAMICALLY CONTOURED

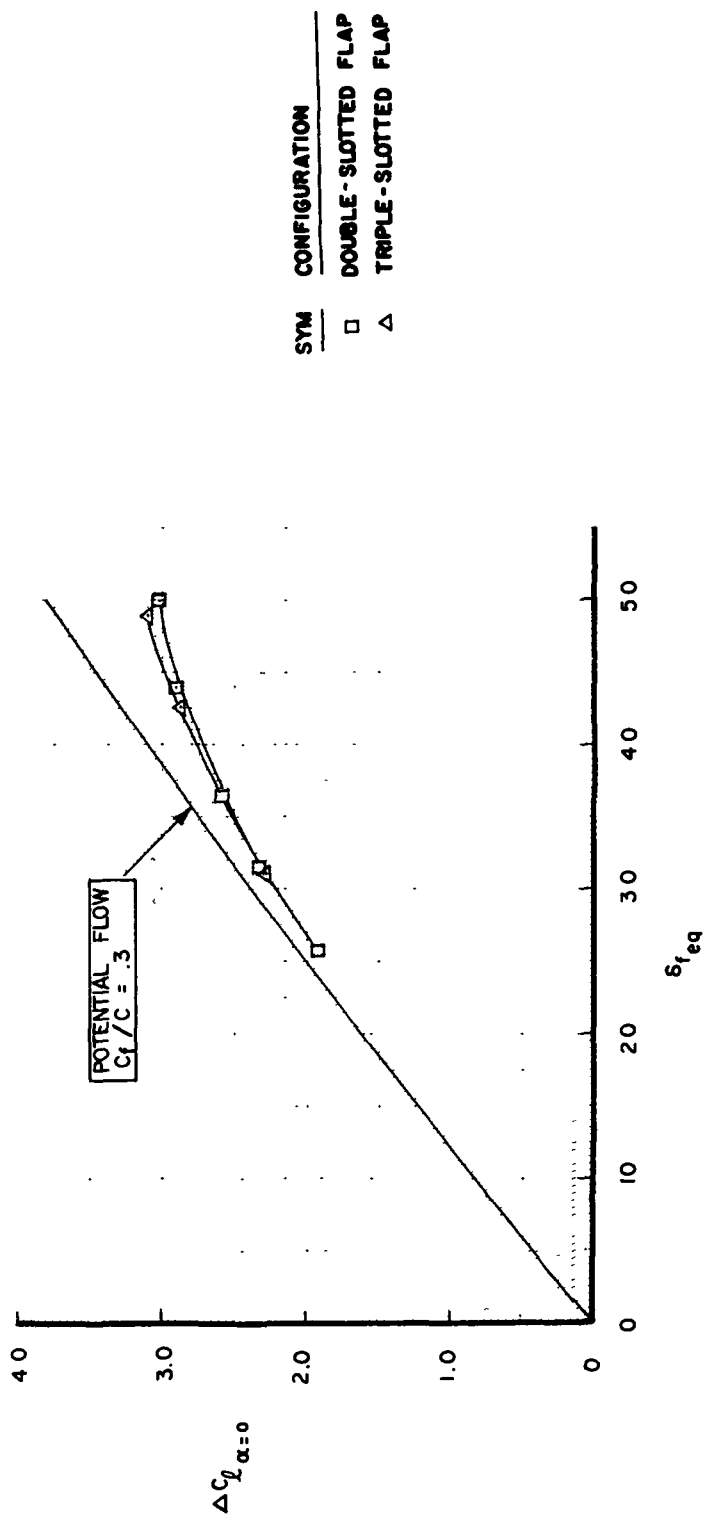
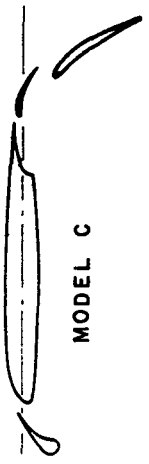
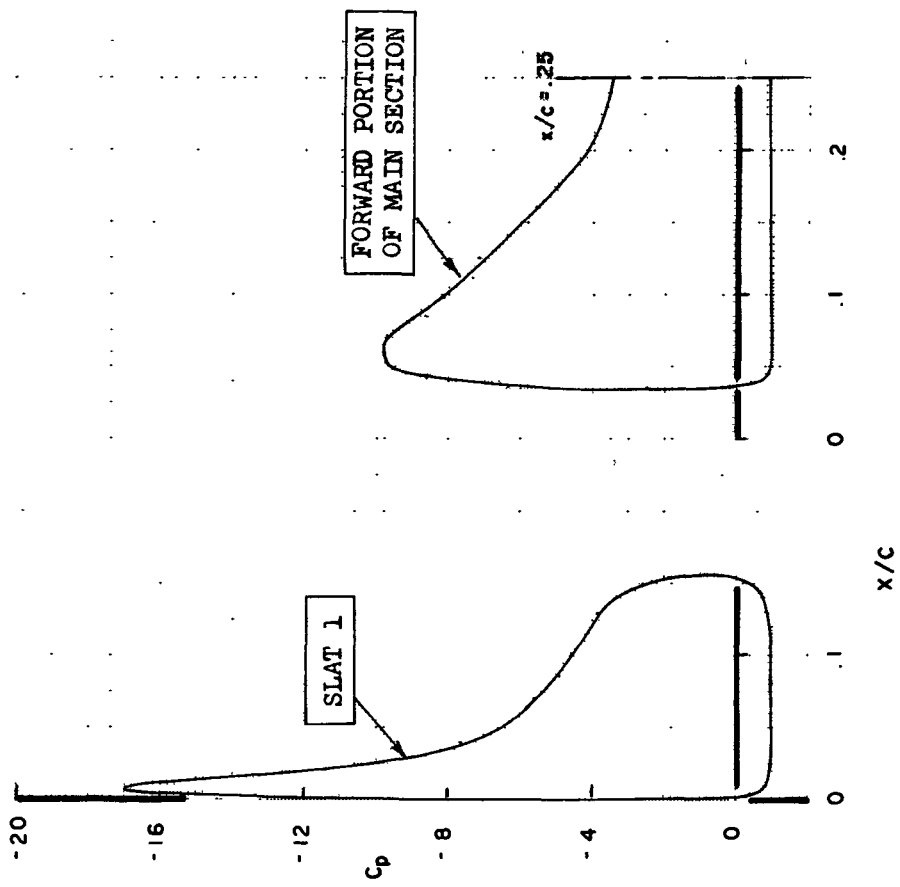


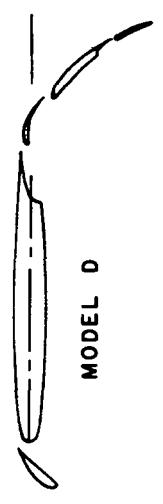
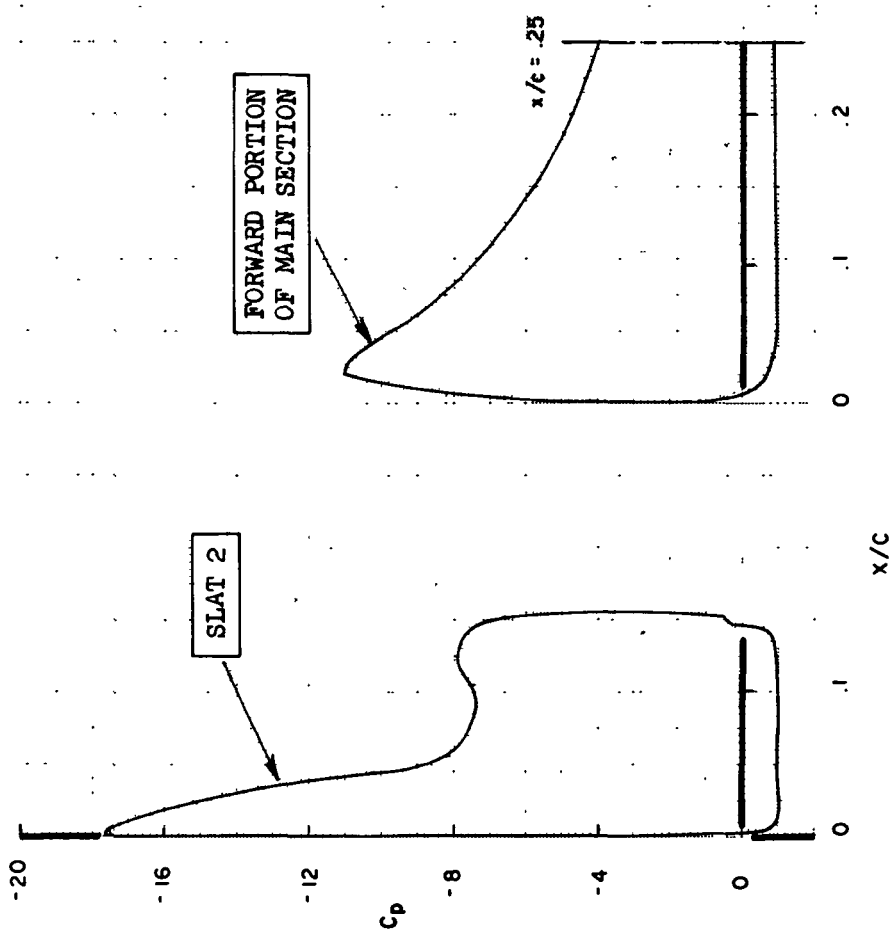
FIGURE 5.--LIFT INCREMENT DUE TO DEFLECTION OF 0.3c DOUBLE- AND TRIPLE-SLOTTED FLAPS (BOEING DATA)



MODEL C

$C_L = 4.92$
 $\alpha = 16^\circ$
 $\delta_{l.e.} = 50^\circ$

FIGURE 6.—DESIGN LEADING-EDGE PRESSURE DISTRIBUTIONS OF MODEL C
(POTENTIAL-FLOW ANALYSIS)



MODEL D

$C_L = 5.13$ $\alpha = 16^\circ$ $\delta_{l,d} = 47^\circ$
--

FIGURE 7.—DESIGN LEADING-EDGE PRESSURE DISTRIBUTIONS OF MODEL D
(POTENTIAL-FLOW ANALYSIS)

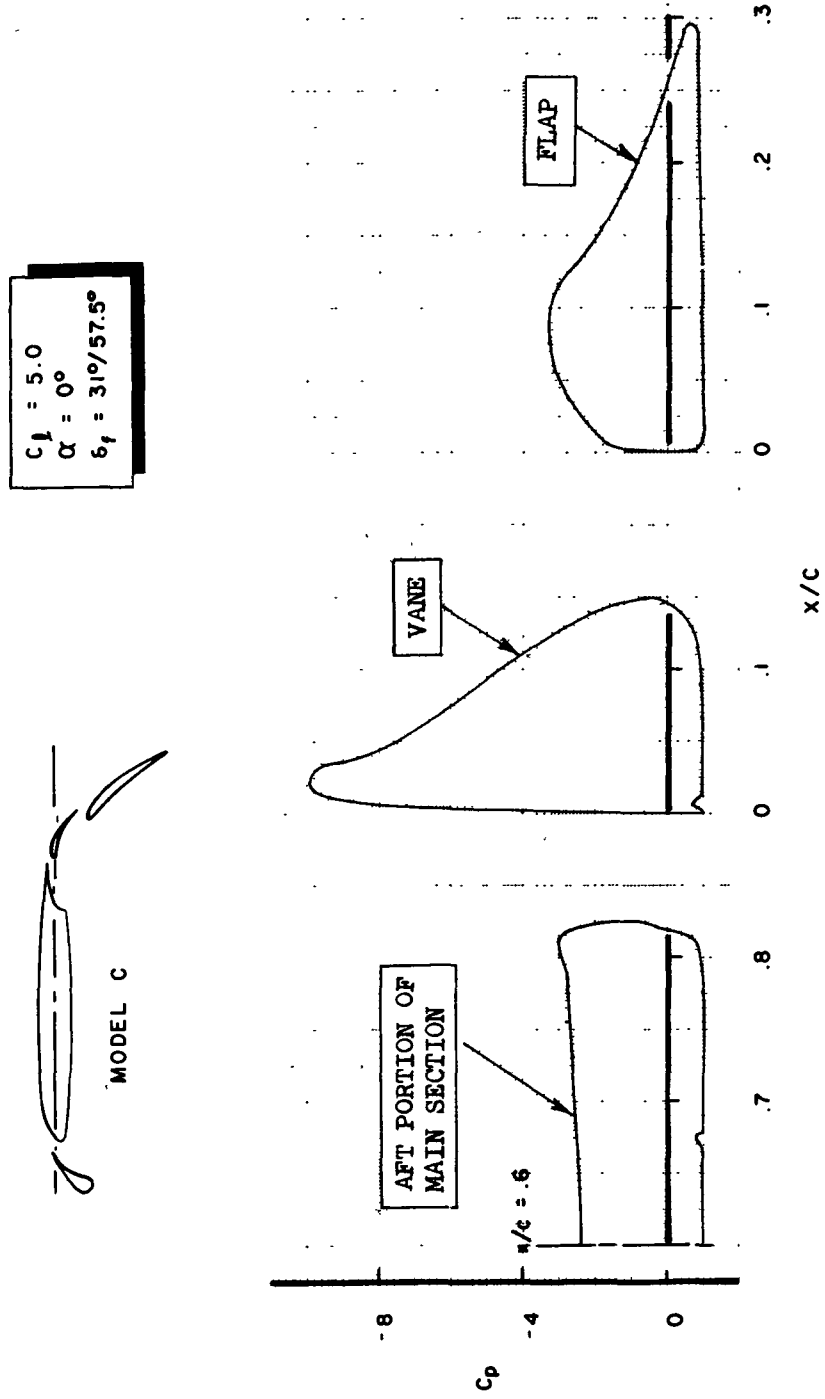


FIGURE 8.—DESIGN PRESSURE DISTRIBUTIONS OF THE TRAILING-EDGE FLAP OF MODEL C (POTENTIAL-FLOW ANALYSIS)

$C_l = 5.69$
 $\alpha = 0^\circ$
 $\delta_f = 25^\circ/55^\circ/77^\circ$

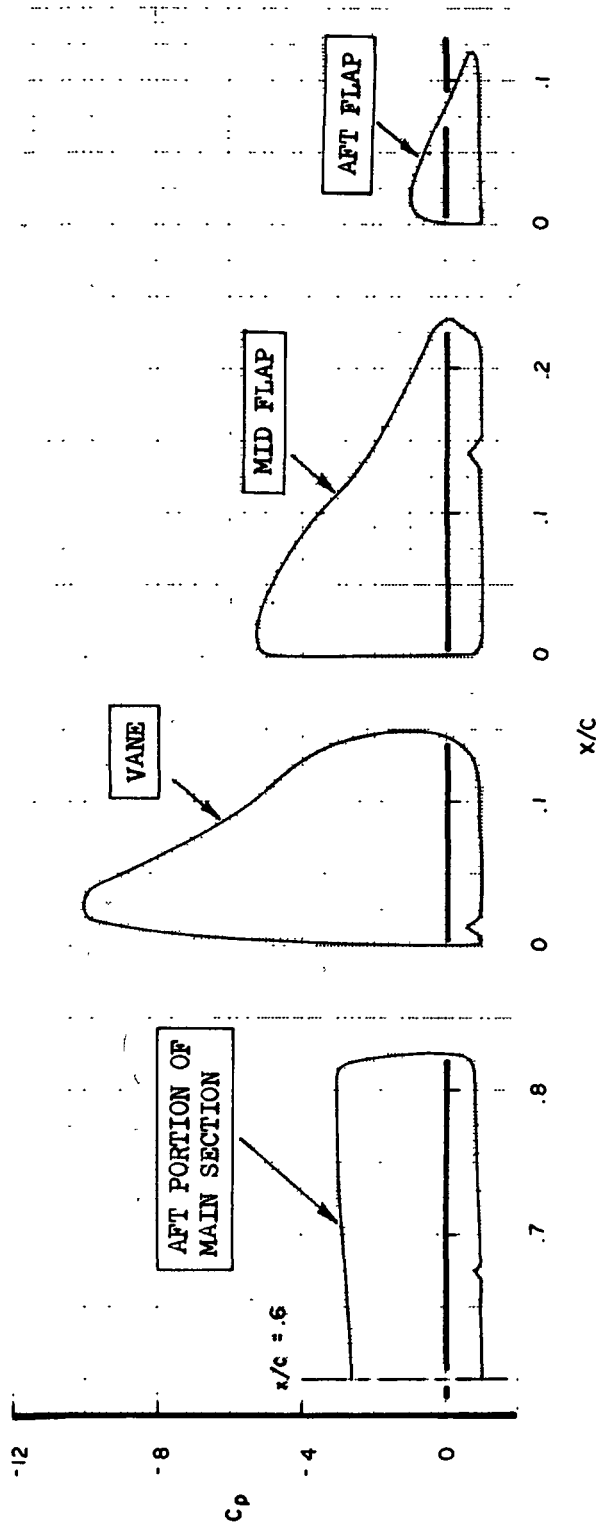
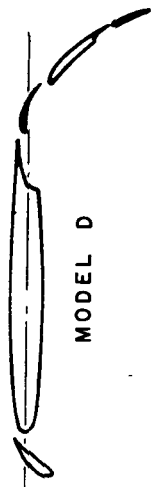


FIGURE 9.—DESIGN PRESSURE DISTRIBUTIONS OF THE TRAILING-EDGE FLAP OF MODEL D (POTENTIAL-FLOW ANALYSIS)

[REDACTED]

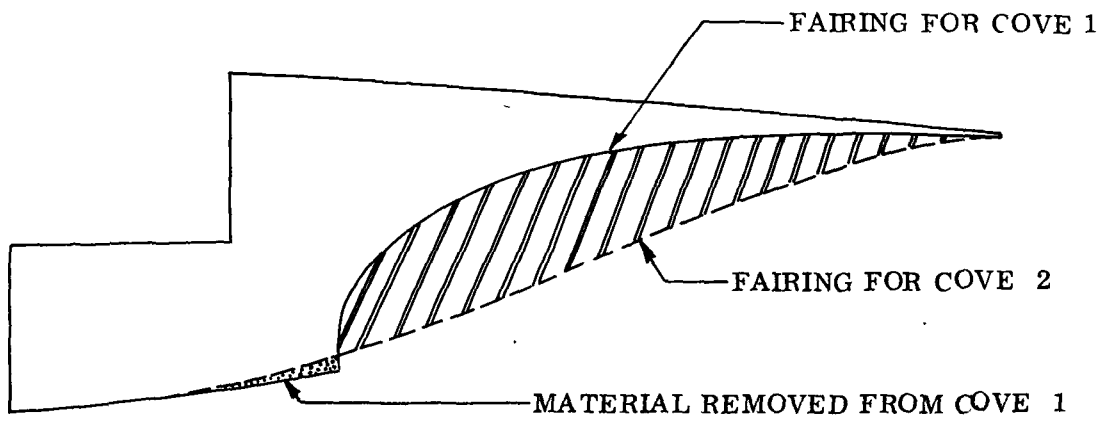


FIGURE 10.—COVE DESIGN AND FABRICATION DETAILS

[REDACTED]

SYM	δ_f	δ_{le}	$C_{l_{max}}$	α_{stall}
○	28.5°	50.2°	4.85	16.8°
□	0°	50°	4.39	21.8°

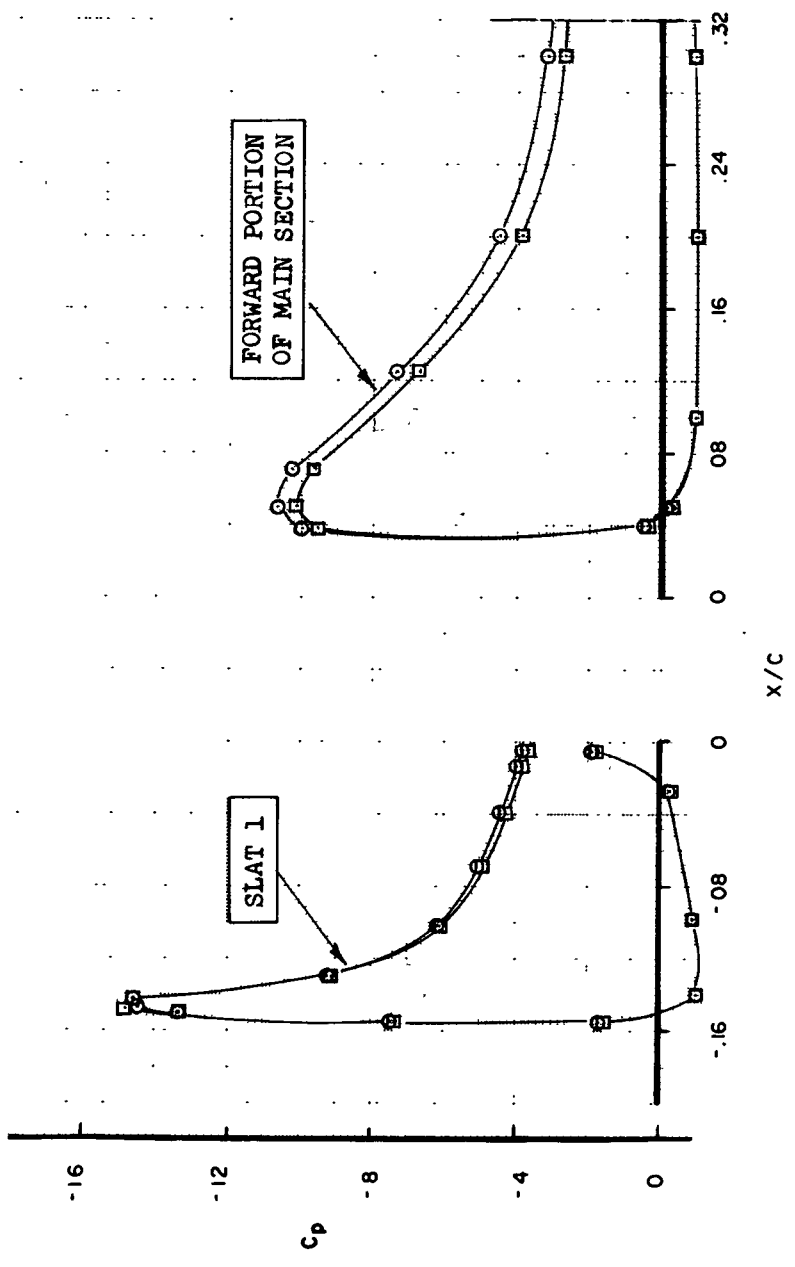
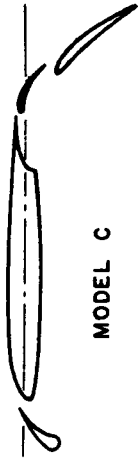


FIGURE 11.—VARIATIONS IN LEADING-EDGE PRESSURE DISTRIBUTIONS AT $C_{l_{max}}$ DUE TO TRAILING-EDGE FLAP DEFLECTION

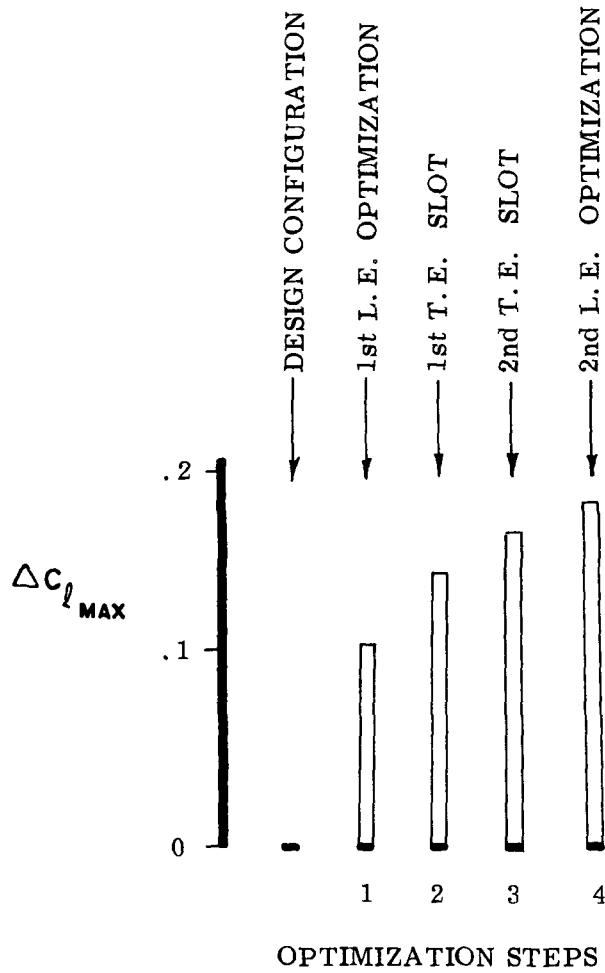
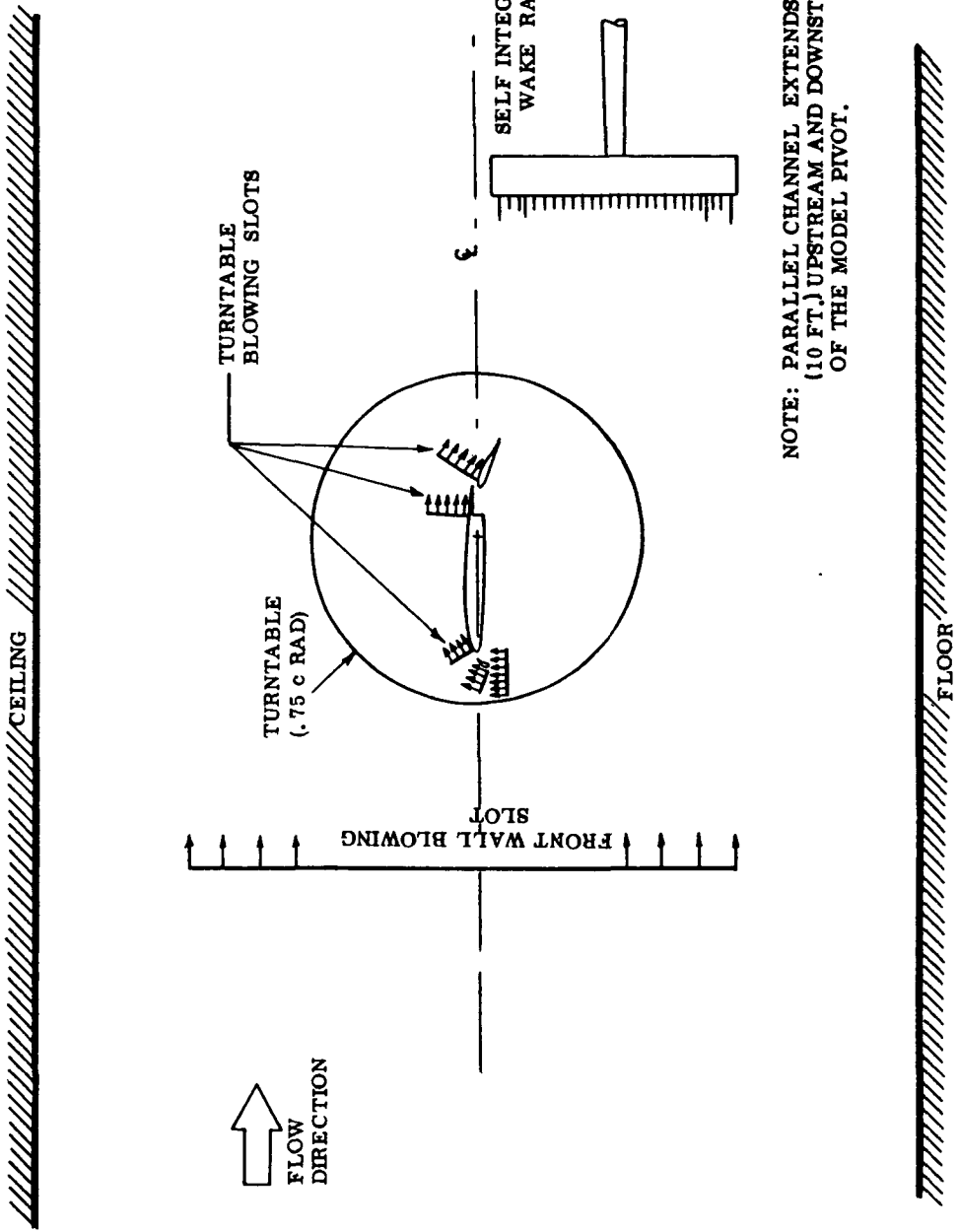


FIGURE 12.—IMPROVEMENTS IN $C_{l_{max}}$ OF MODEL C DUE TO LEADING-EDGE SLAT AND TRAILING-EDGE FLAP OPTIMIZATION



NOTE: PARALLEL CHANNEL EXTENDS 304.8 cm (10 FT.) UPSTREAM AND DOWNSTREAM OF THE MODEL PIVOT.

FIGURE 13.—LOCATIONS OF WALL AND TURNTABLE BOUNDARY-LAYER CONTROL SLOTS IN THE BOEING RESEARCH WIND TUNNEL TEST SECTION

CONFIDENTIAL

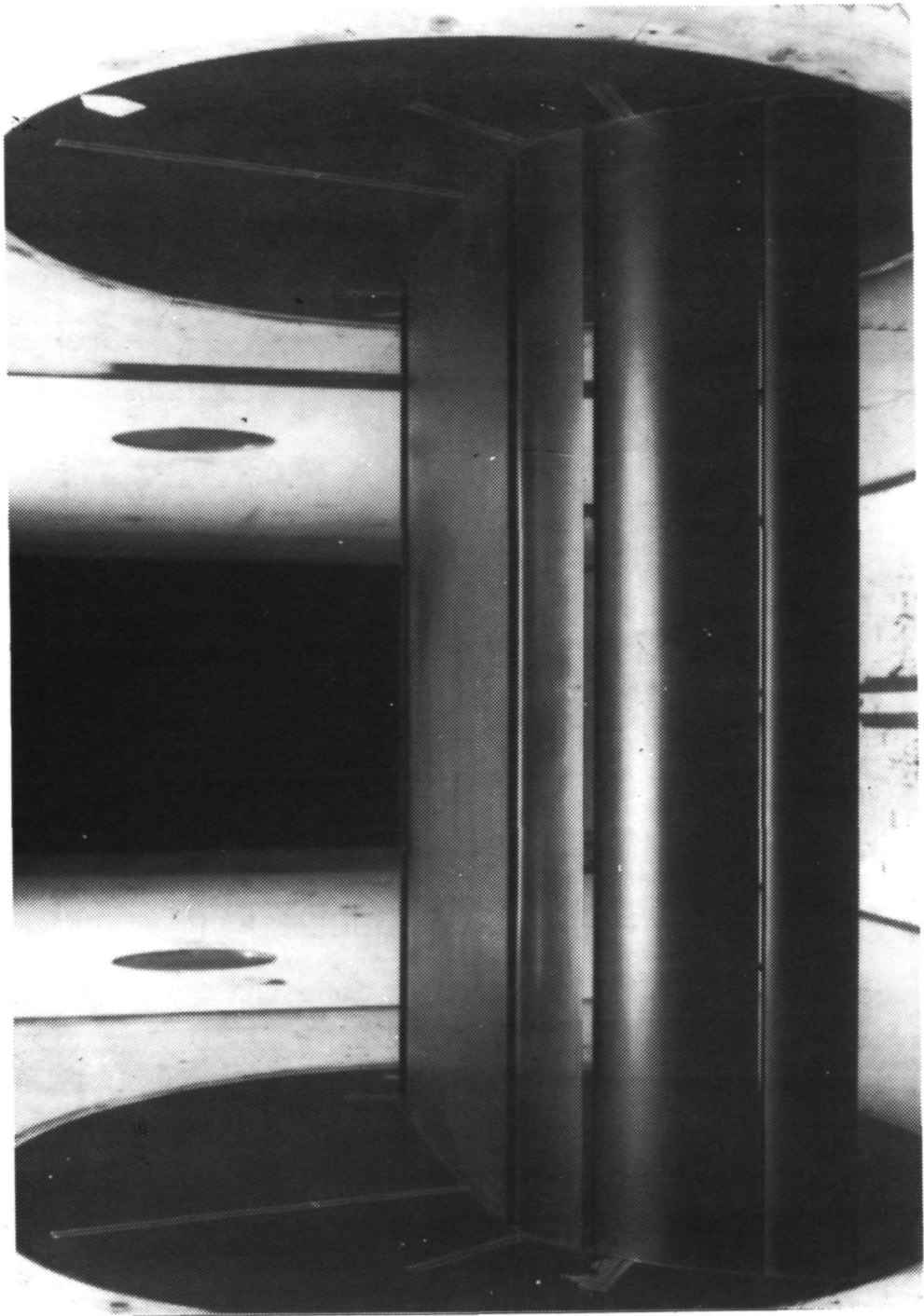
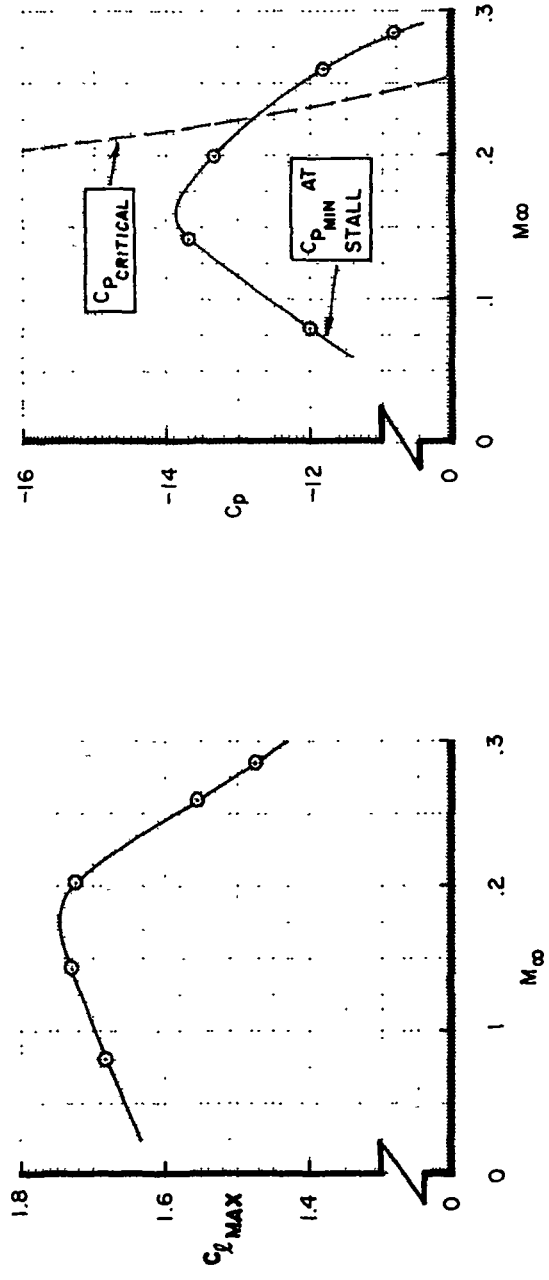


FIGURE 14.—INSTALLATION OF MODEL IN THE BOEING RESEARCH WIND TUNNEL

CONFIDENTIAL



(a)

(b)

FIGURE 15.—EFFECTS OF FREESTREAM MACH NUMBER ON $C_{l,max}$ AND $C_{p,min}$ OF THE NASA SUPERCRITICAL AIRFOIL

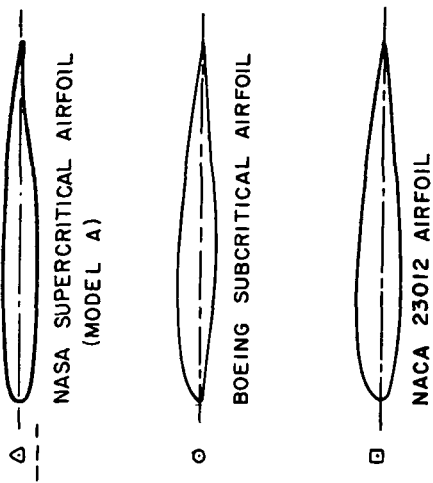
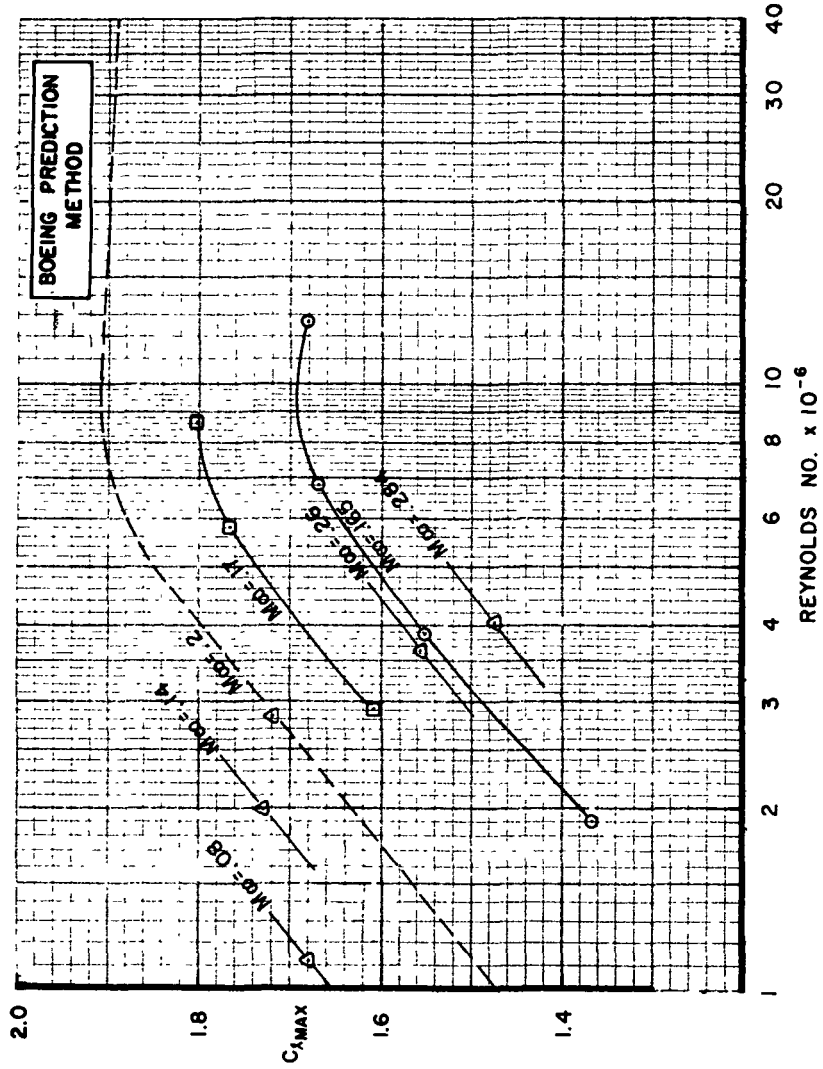
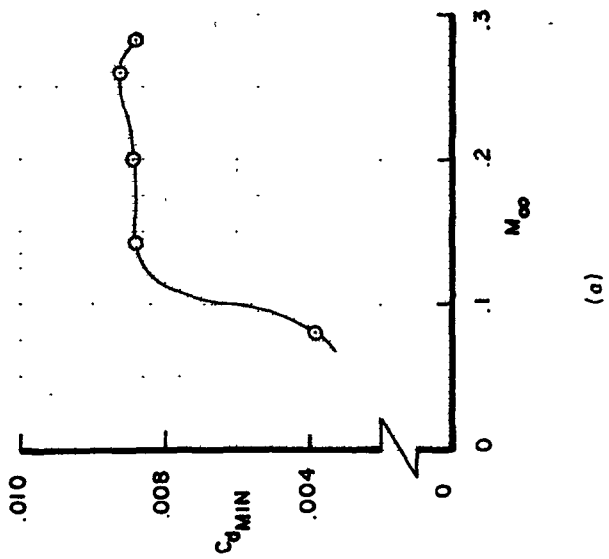
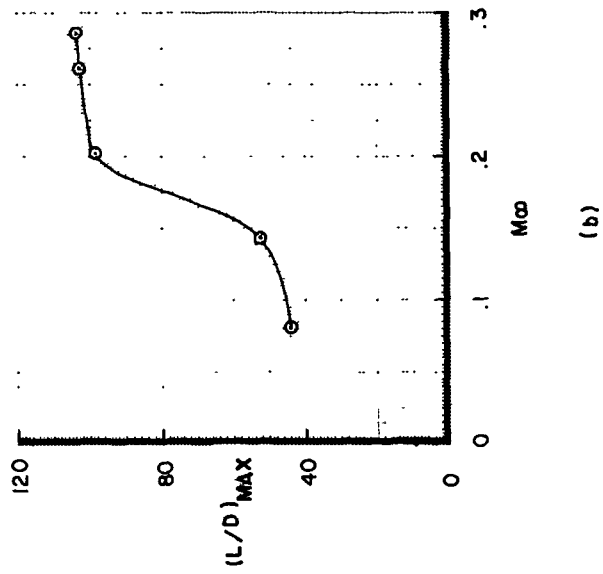


FIGURE 16.—EFFECTS OF MACH NUMBER AND REYNOLDS NUMBER ON $C_{L_{MAX}}$



(a)



(b)

FIGURE 17.—EFFECTS OF FREESTREAM MACH NUMBER ON $C_{d_{min}}$ AND $(L/D)_{max}$ OF THE NASA SUPERCRITICAL AIRFOIL

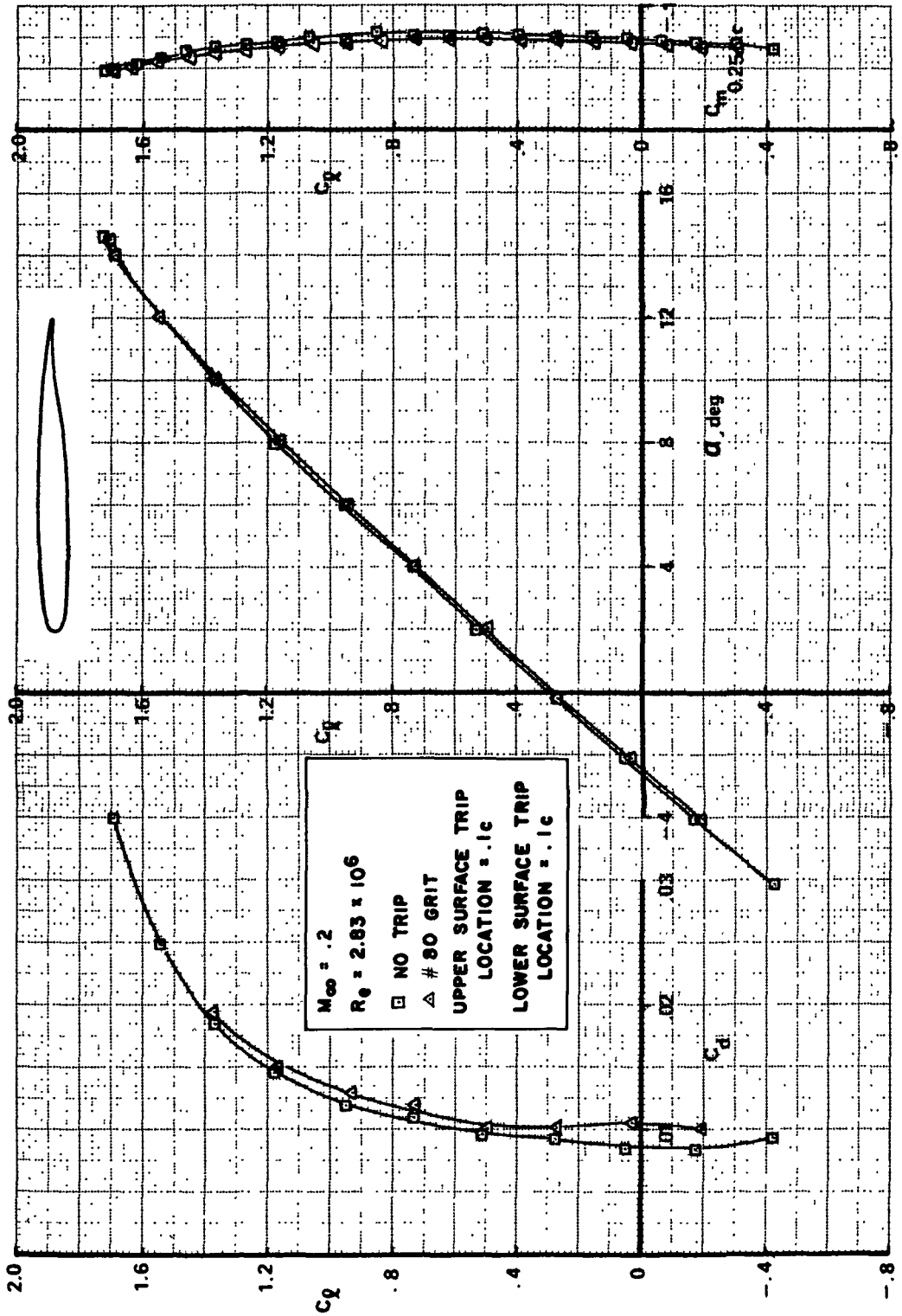


FIGURE 18.—AERODYNAMIC CHARACTERISTICS OF THE NASA 9.3% CHORD THICK SUPERCRITICAL AIRFOIL

SYM	δ_L	C/c	$\Delta x/c$
O	20°	.020	0.
△	30°	.010	.005
□	40°	.007	.010
◇	50°	.007	.010

NOTE: ● SYMBOLS
INDICATE
FAIRED COVE 2.

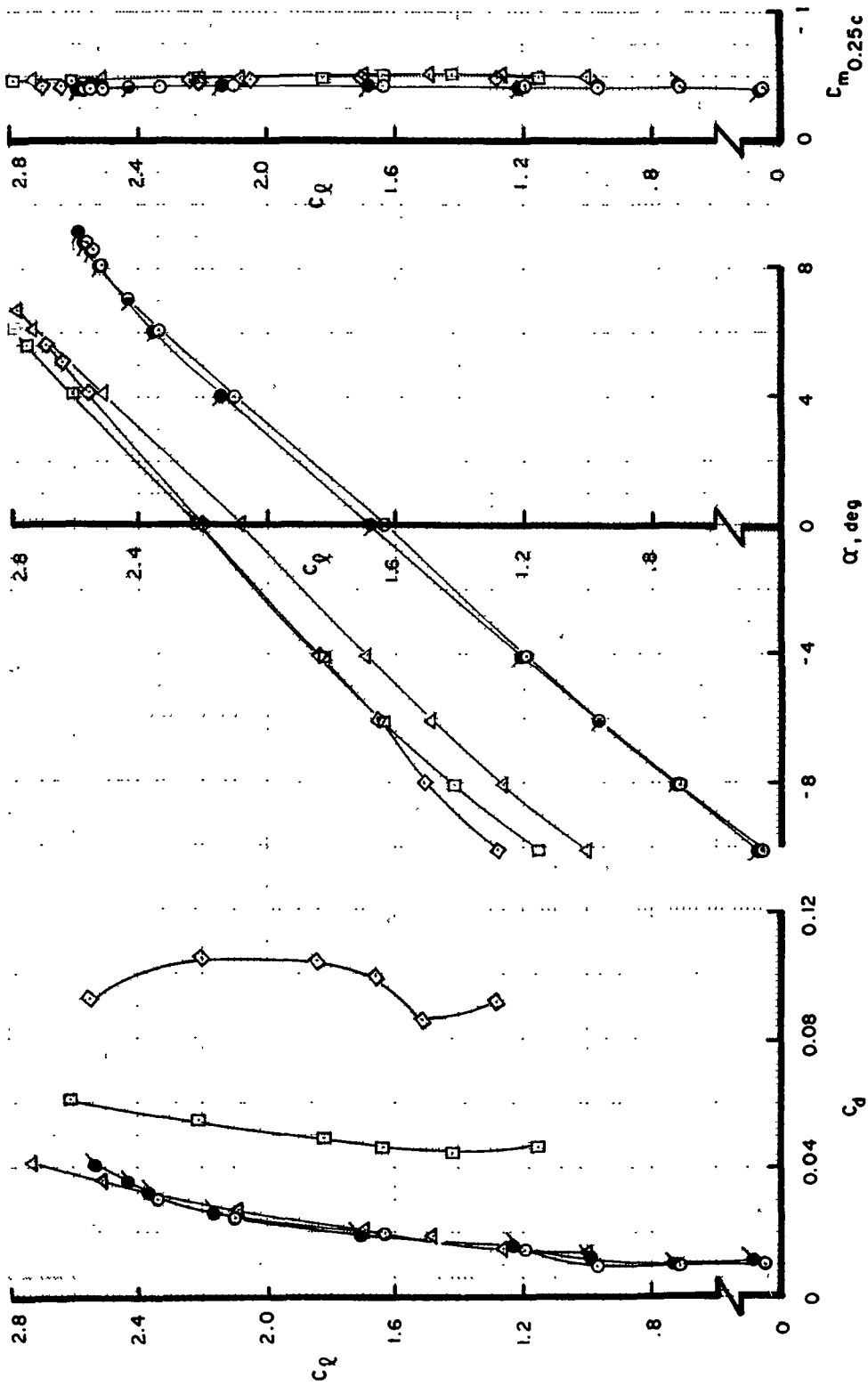


FIGURE 19.—AERODYNAMIC CHARACTERISTICS OF MODEL B FOR TRAILING-EDGE FLAP DEFLECTIONS OF 20°, 30°, 40°, AND 50°

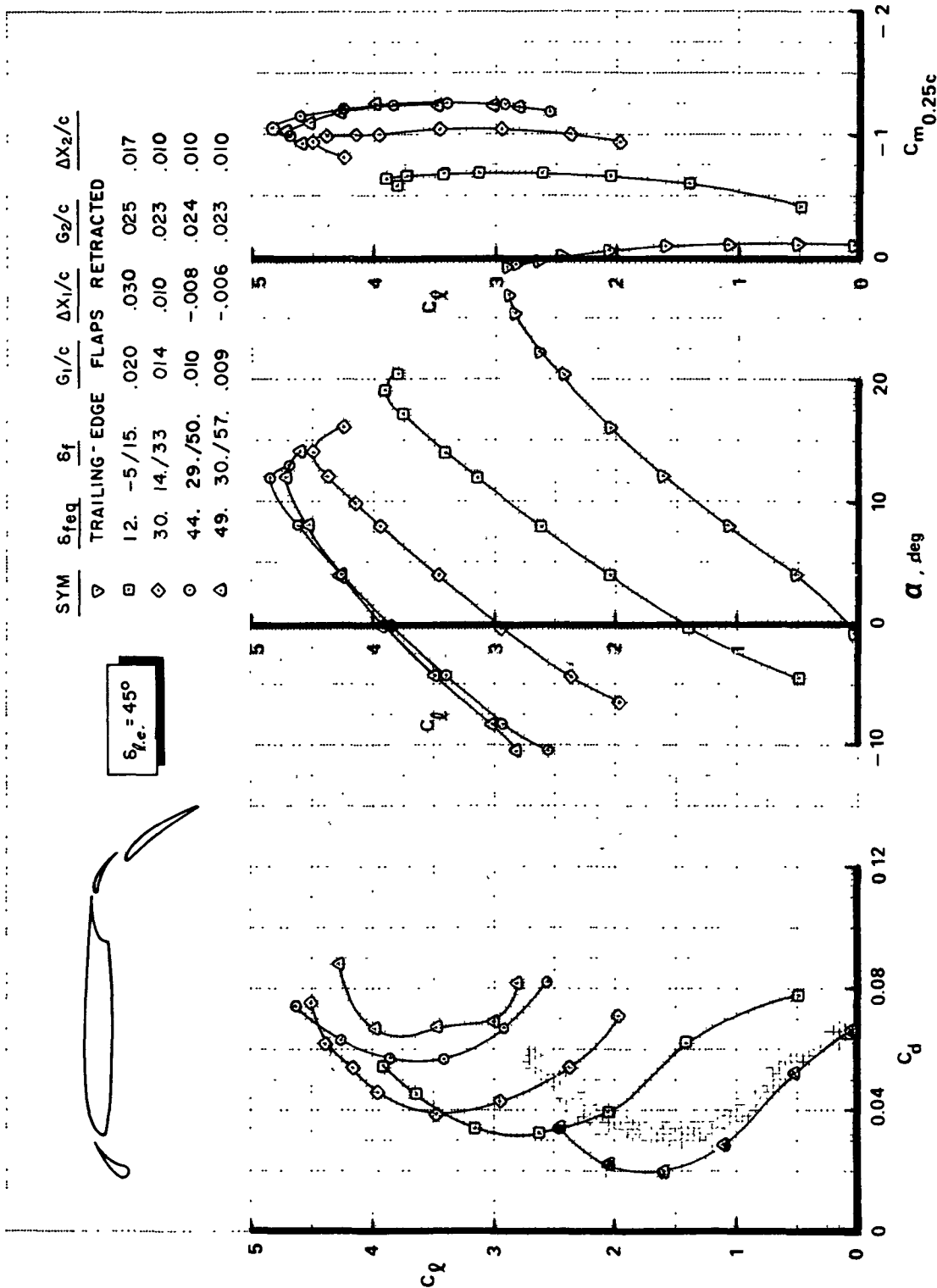


FIGURE 20.—AERODYNAMIC CHARACTERISTICS OF MODEL C FOR EQUIVALENT FLAP DEFLECTIONS OF 0°, 12°, 30°, 44°, AND 49°

SYM	δ_{1e}	δ_f	G_1/c	$\Delta\pi_1/c$	G_2/c	$\Delta\pi_2/c$
○	45°	5°/15°	.020	.030	.025	.017
□	50°	0°/16°	.020	-.008	.022	.010

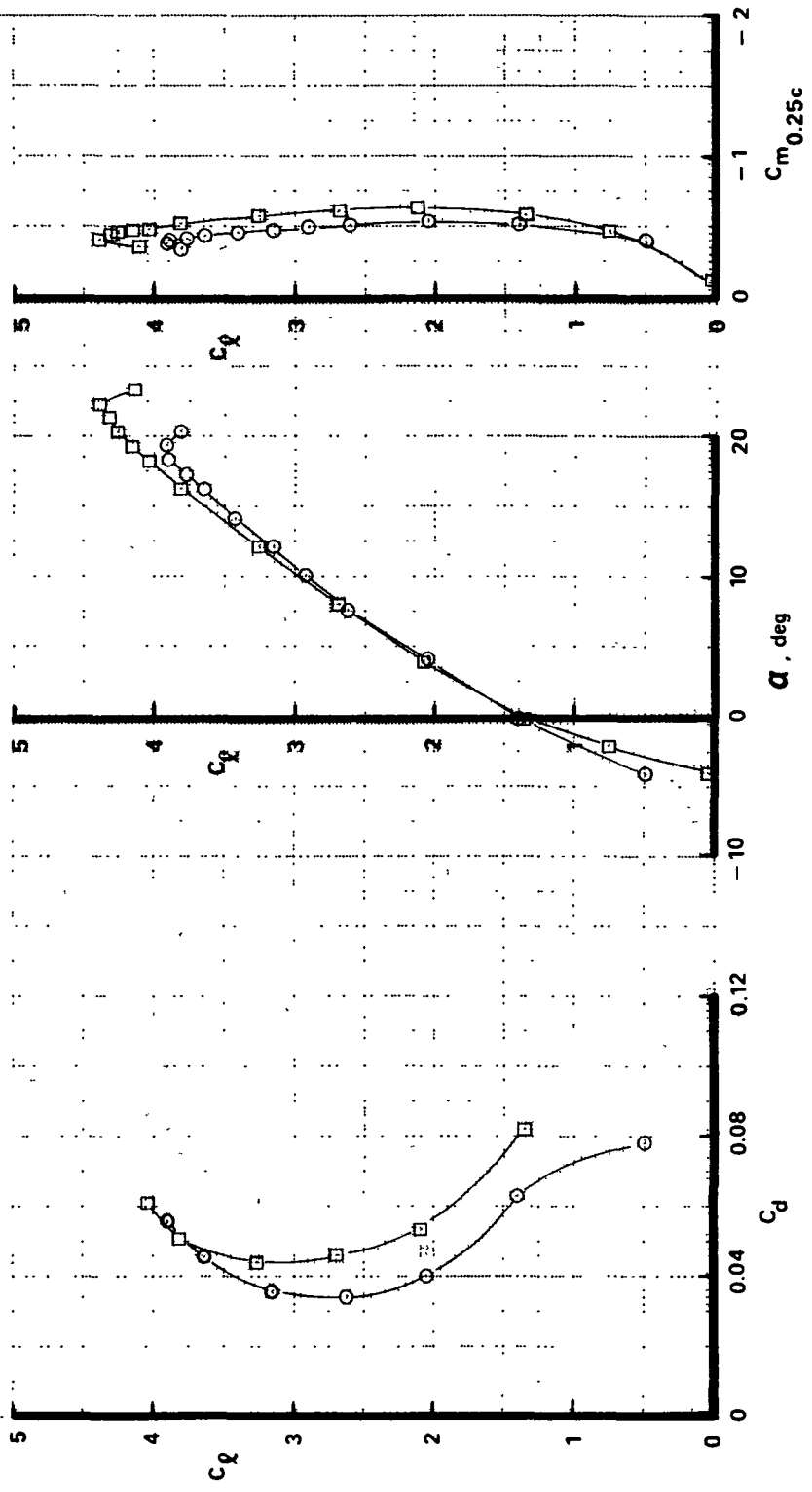
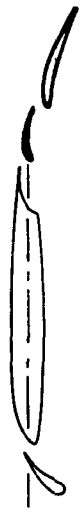


FIGURE 21.—COMPARISON OF A COMPROMISED TAKEOFF CONFIGURATION WITH ONE THAT HAS BEEN OPTIMIZED FOR $C_{l,max}$

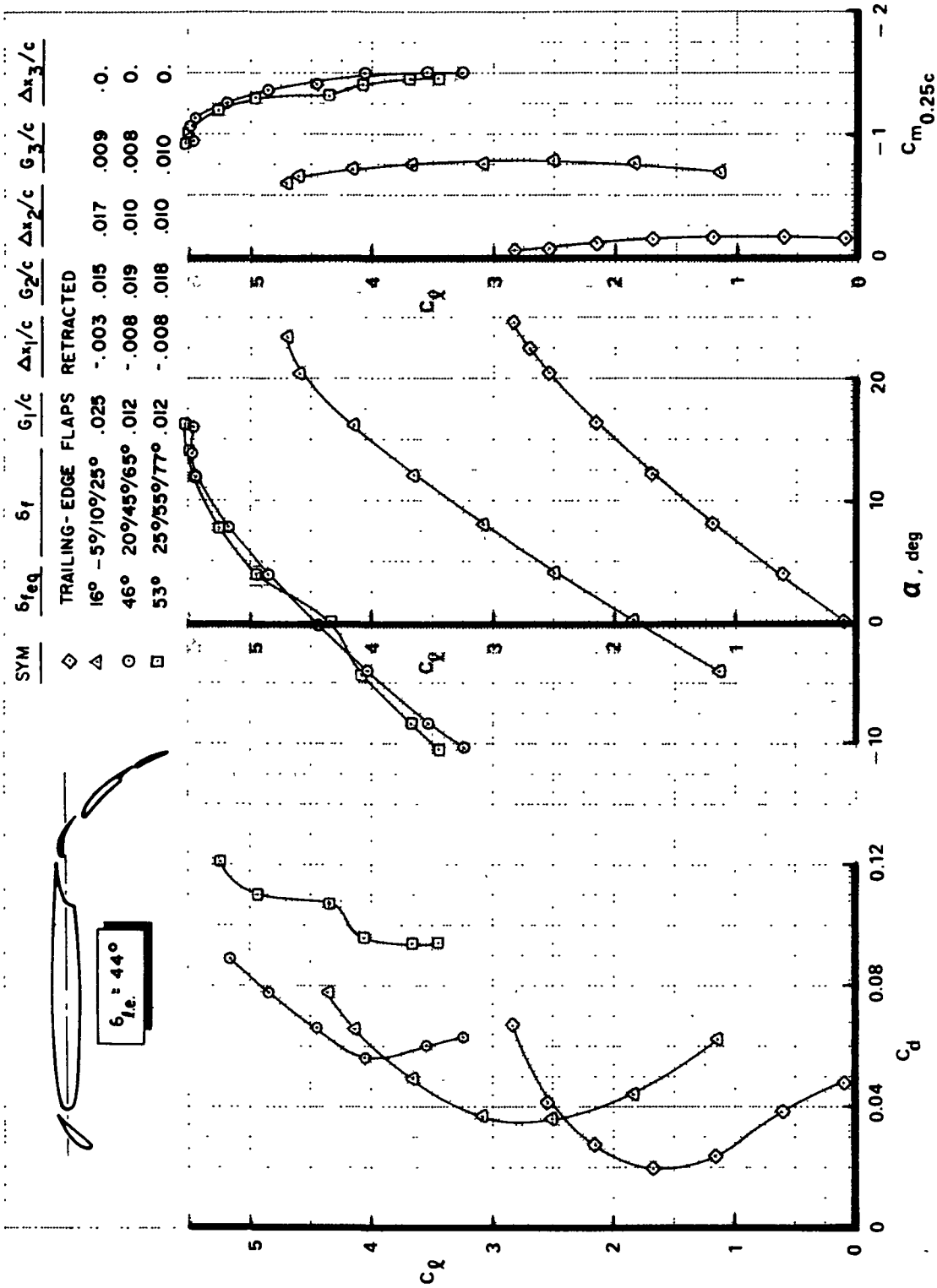
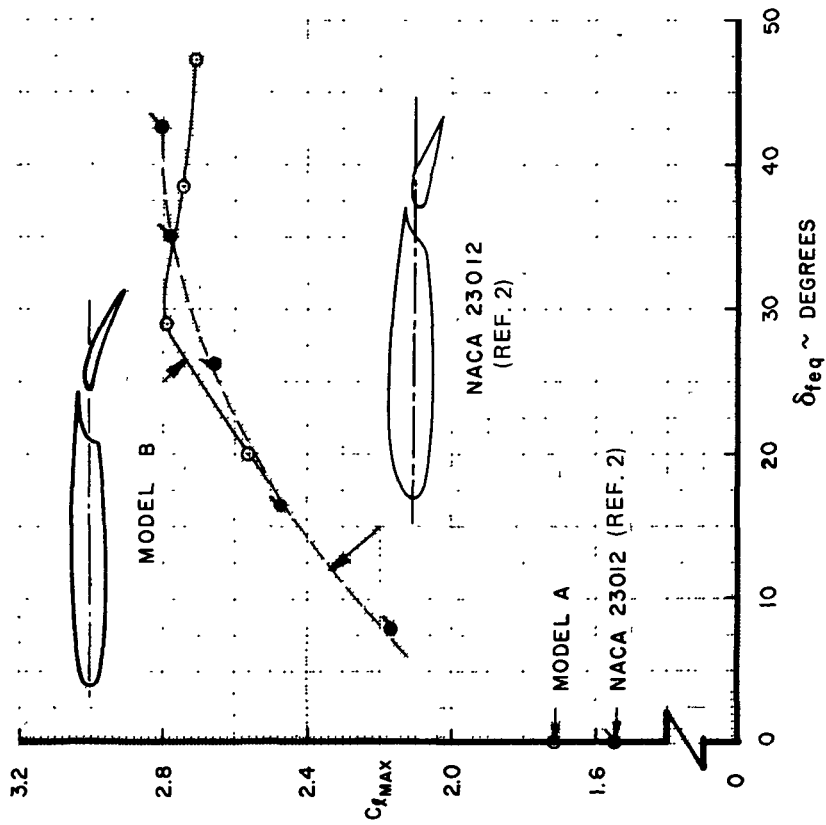


FIGURE 22.—AERODYNAMIC CHARACTERISTICS OF MODEL D FOR EQUIVALENT FLAP DEFLECTIONS OF 0°, 16°, 46°, AND 53°



SYM	CONFIG.	C_f/c	C'/C	Re
○	MODEL B	.295	1.12	$2.83 \cdot 10^6$
●	NACA 23012	.257	1.09	$3.5 \cdot 10^6$

FIGURE 23.—COMPARISON OF THE MAXIMUM LIFT OF MODEL B WITH THAT OF A SINGLE-SLOTTED FLAP CONFIGURATION OF THE NACA 23012 AIRFOIL

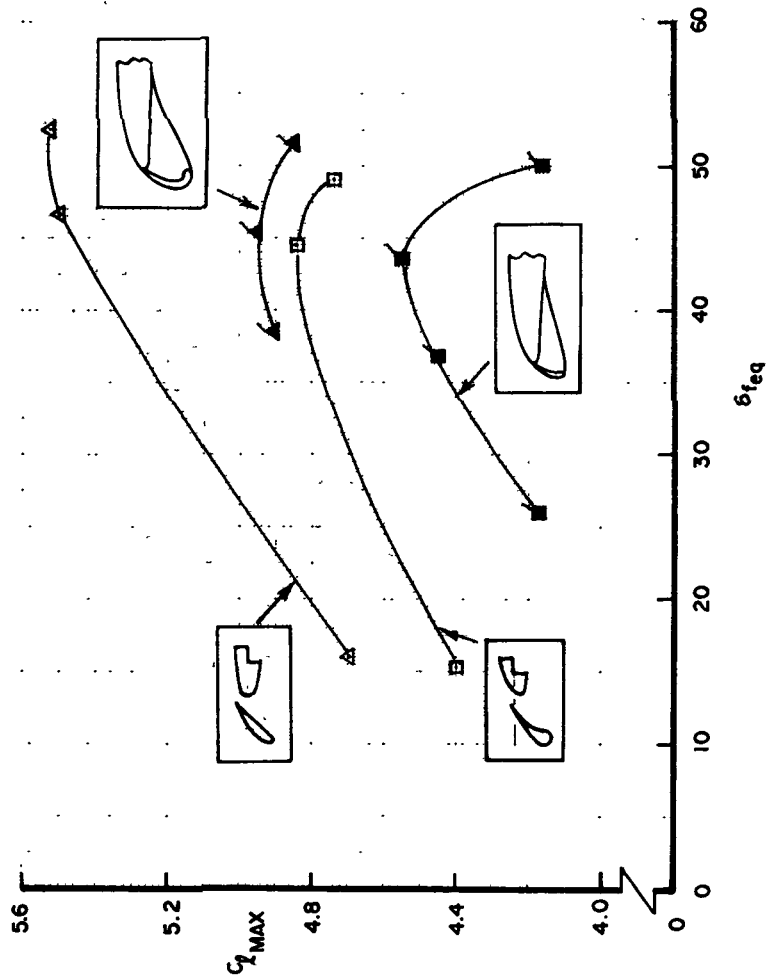


FIGURE 24.—COMPARISON OF THE MAXIMUM LIFT OF MODELS C AND D WITH DOUBLE- AND TRIPLE-SLOTTED FLAP CONFIGURATIONS OF THE BOEING 707 AIRFOIL

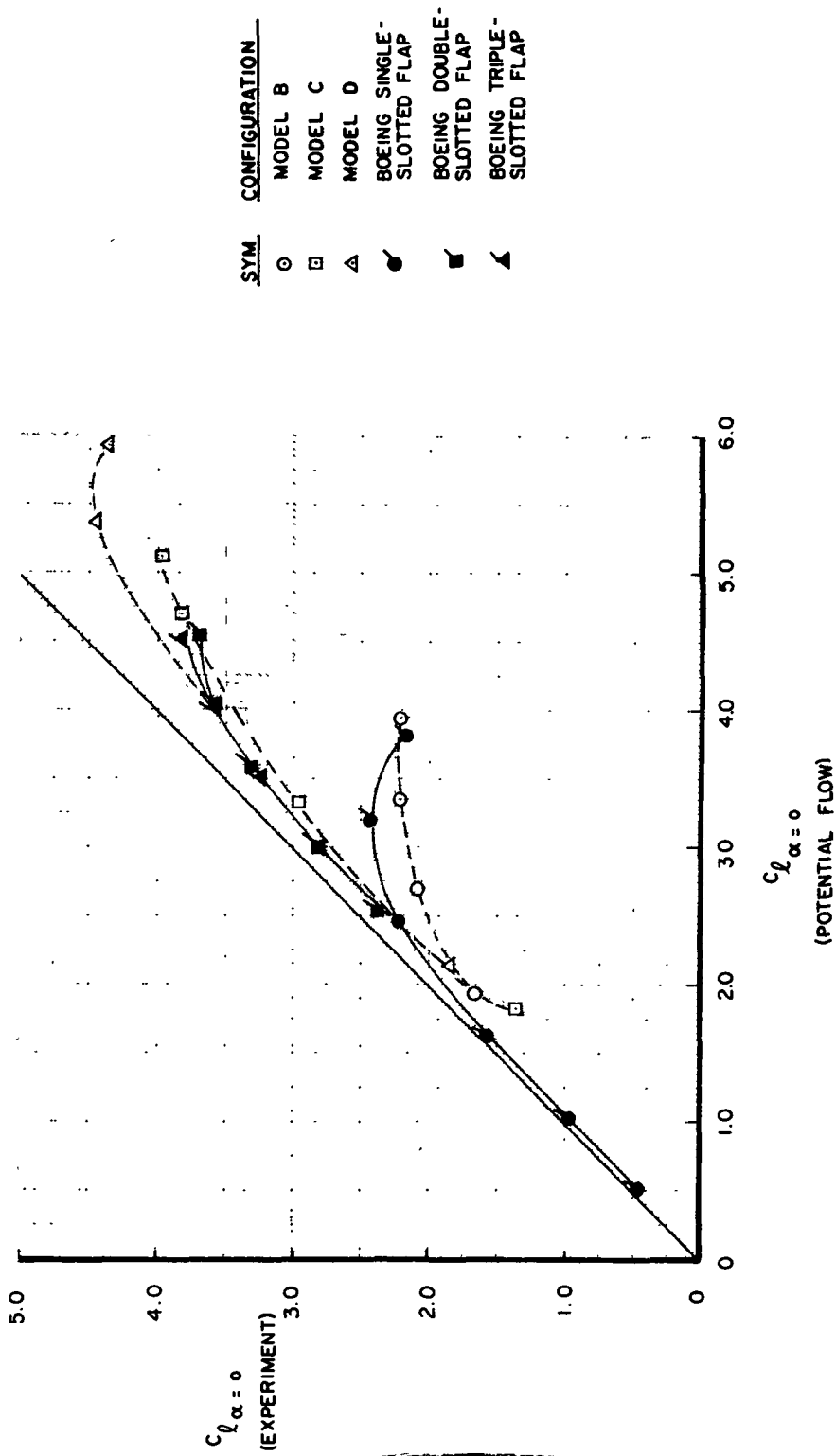
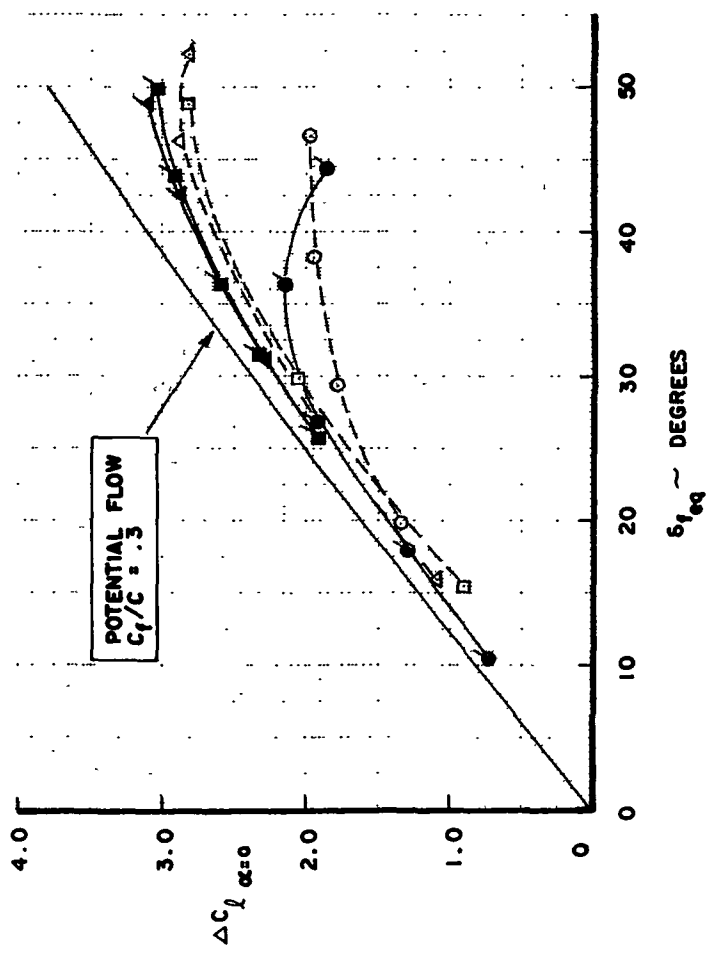


FIGURE 25.—COMPARISON OF EXPERIMENTAL VERSUS POTENTIAL-FLOW LIFT OF MODELS B, C, AND D AND OF THE HIGH-LIFT CONFIGURATIONS OF THE BOEING 707 AIRFOIL



SYM	CONFIGURATION
○	MODEL B
□	MODEL C
△	MODEL D
◊	BOEING SINGLE-SLOTTED FLAP
▽	BOEING DOUBLE-SLOTTED FLAP
▲	BOEING TRIPLE-SLOTTED FLAP

FIGURE 26.—COMPARISON OF LIFT DUE TO FLAP DEFLECTION OF MODELS B, C, AND D AND OF HIGH-LIFT CONFIGURATIONS OF THE BOEING 707 AIRFOIL

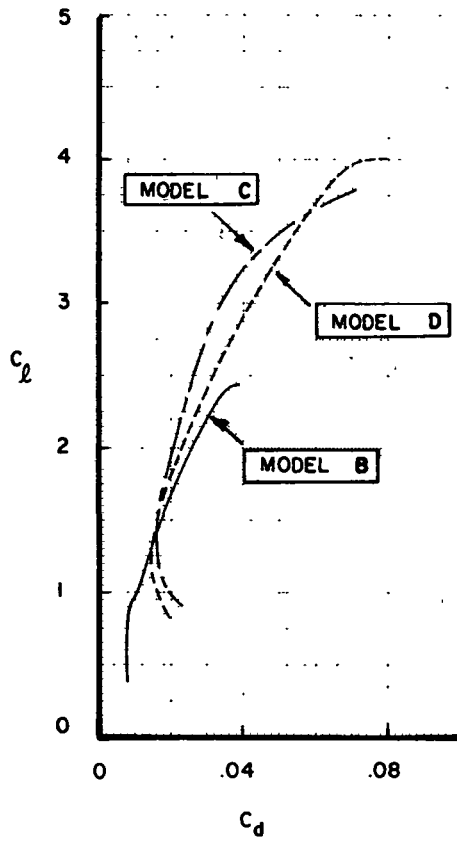


FIGURE 27.—COMPARISON OF THE DRAG ENVELOPES OF MODELS B, C, AND D

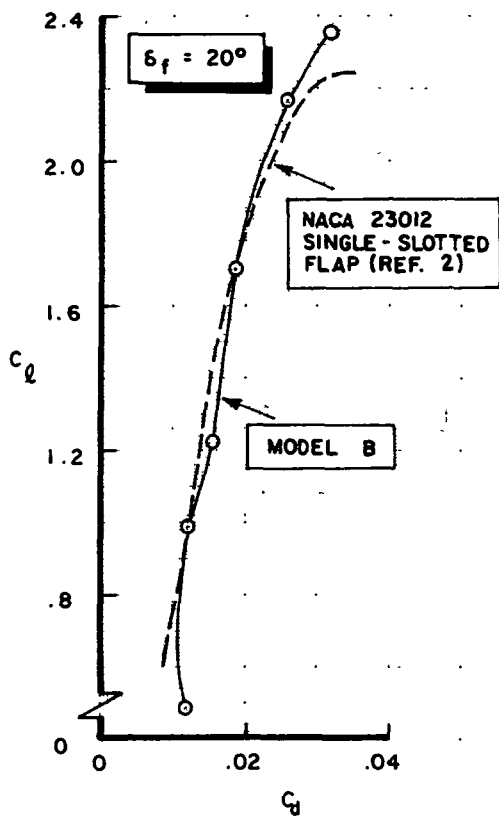


FIGURE 28.—COMPARISON OF THE DRAG POLARS OF MODEL B AND A SINGLE-SLOTTED FLAP CONFIGURATION OF THE NACA 23012 AIRFOIL

SYM	CONFIGURATION
⊙	MODEL B
□	MODEL C
△	MODEL D
●	BOEING SINGLE-SLOTTED FLAP
■	BOEING DOUBLE-SLOTTED FLAP
▲	BOEING TRIPLE-SLOTTED FLAP

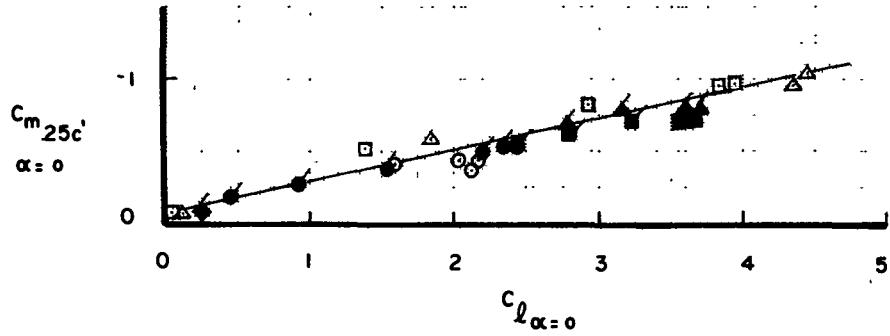


FIGURE 29.—COMPARISON OF THE PITCHING MOMENTS OF MODELS B, C, AND D AND OF HIGH-LIFT CONFIGURATIONS OF THE BOEING 707 AIRFOIL

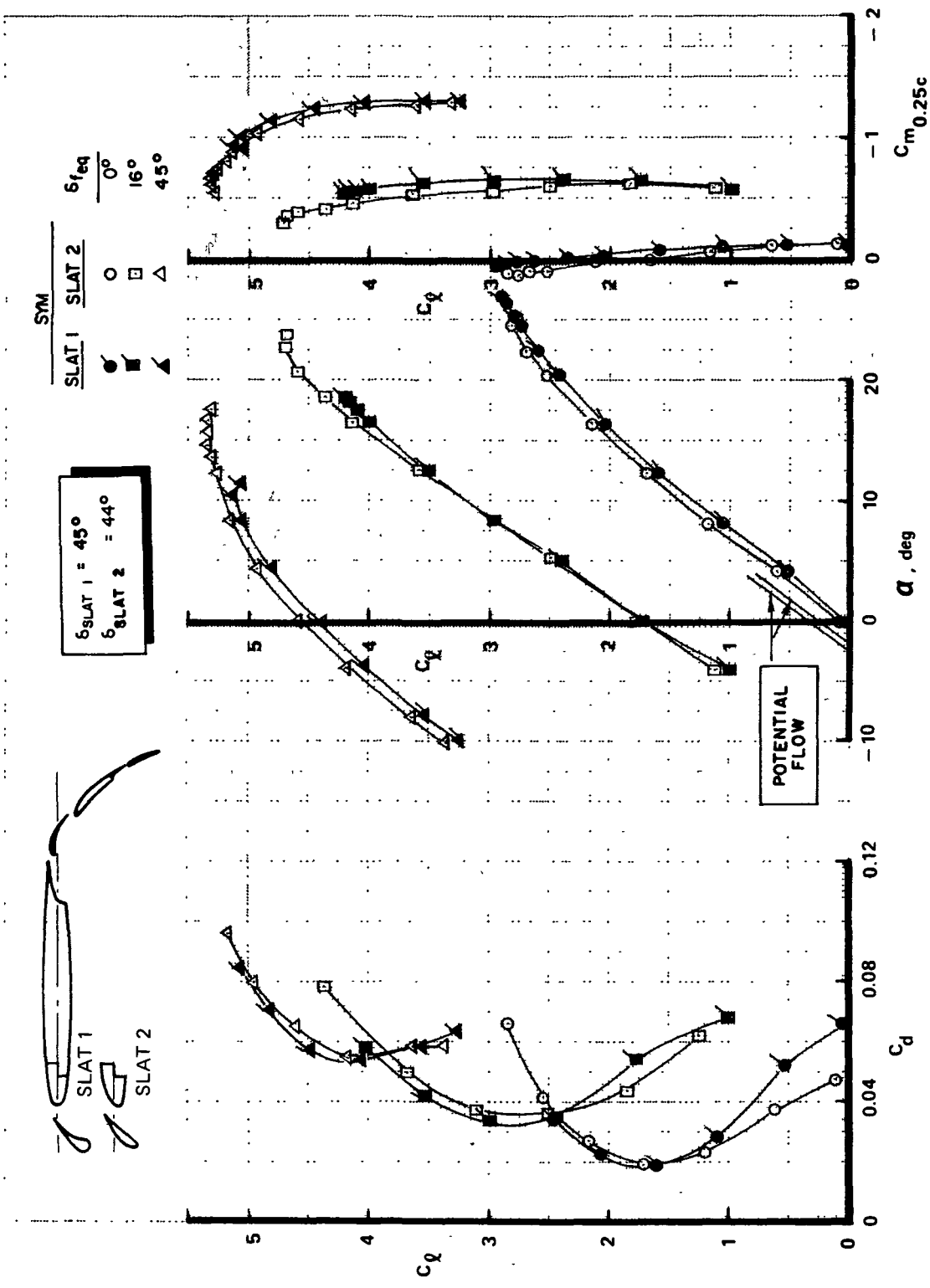


FIGURE 30.—COMPARISON OF LEADING-EDGE SLATS ON THE 9.3% CHORD THICK NASA SUPERCRITICAL AIRFOIL WITH A 0.325c TRIPLE-SLOTTED FLAP HAVING DEFLECTIONS OF 0°, 16°, AND 46°

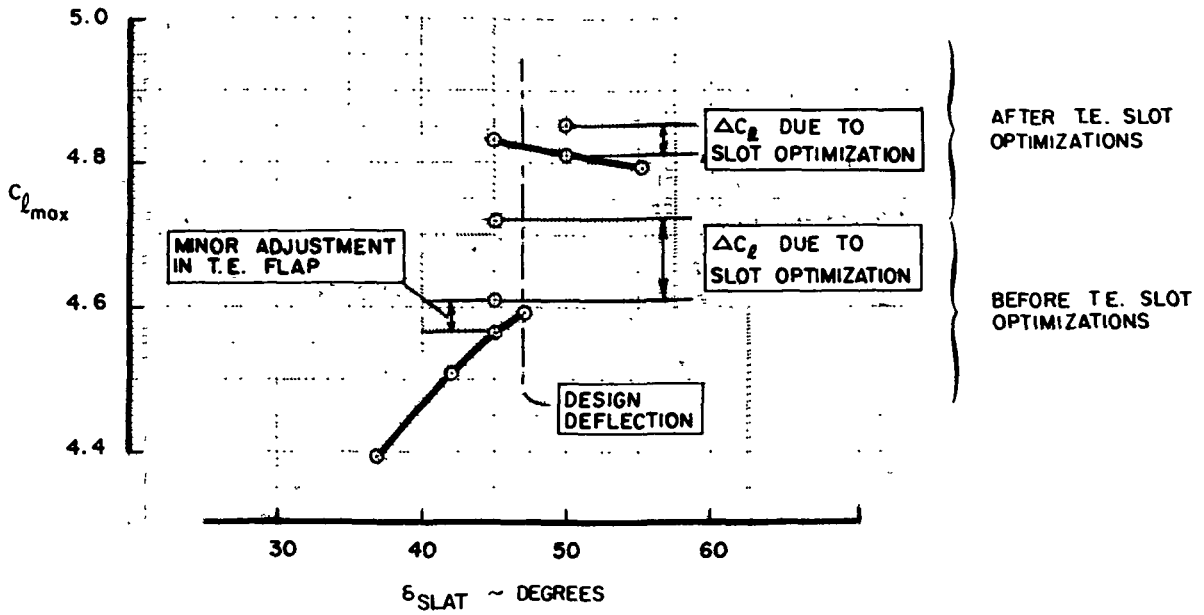


FIGURE 31.—INCREMENTS IN MAXIMUM LIFTS OF MODEL C DUE TO LEADING-EDGE SLAT OPTIMIZATION

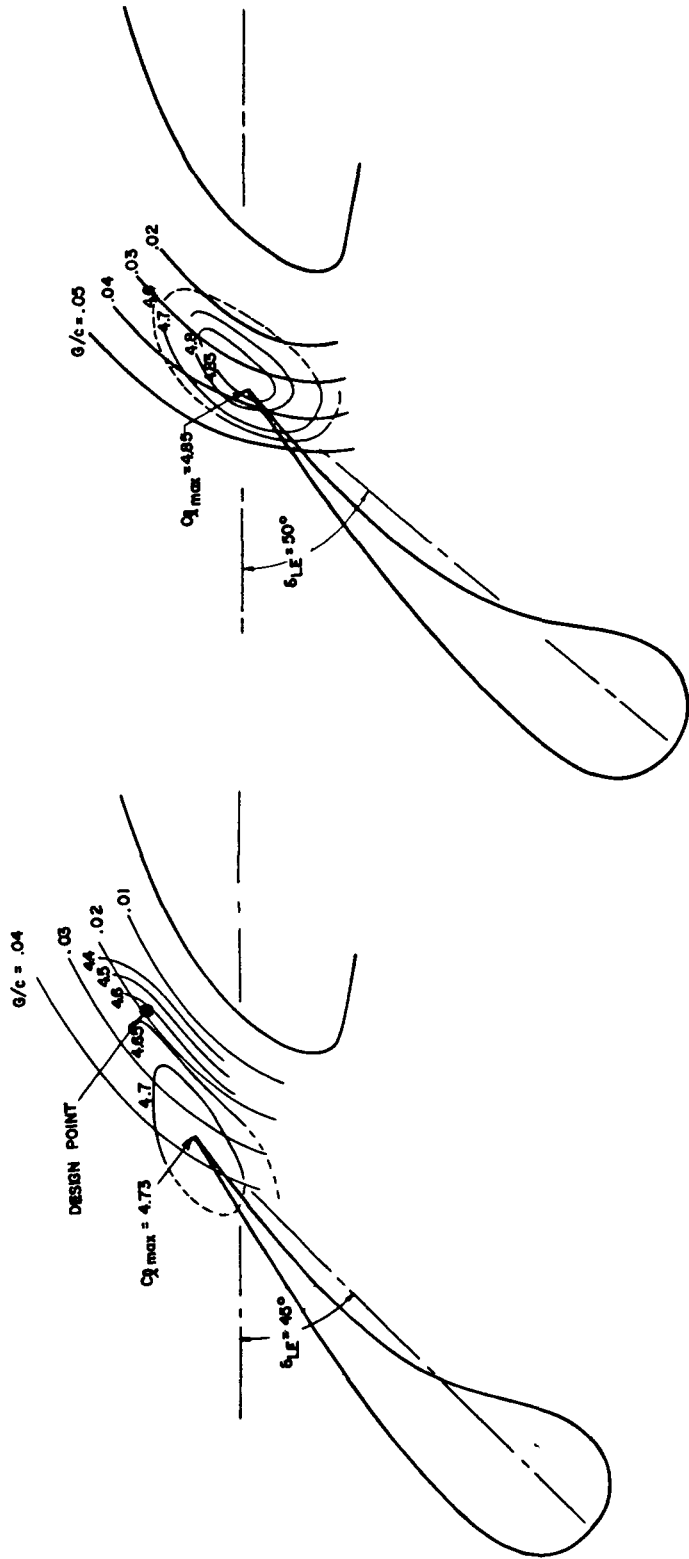


FIGURE 32.—CONTOURS OF SLAT TRAILING-EDGE POSITION FOR CONSTANT $C_{l,max}$ OF MODEL C

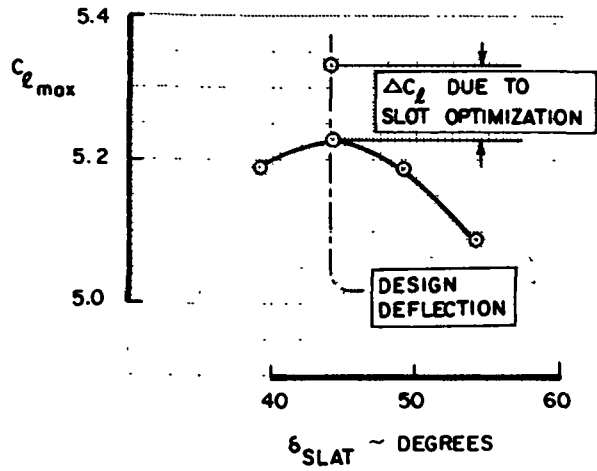


FIGURE 33.—INCREMENT IN $C_{l_{max}}$ OF MODEL D DUE TO LEADING-EDGE SLAT OPTIMIZATION

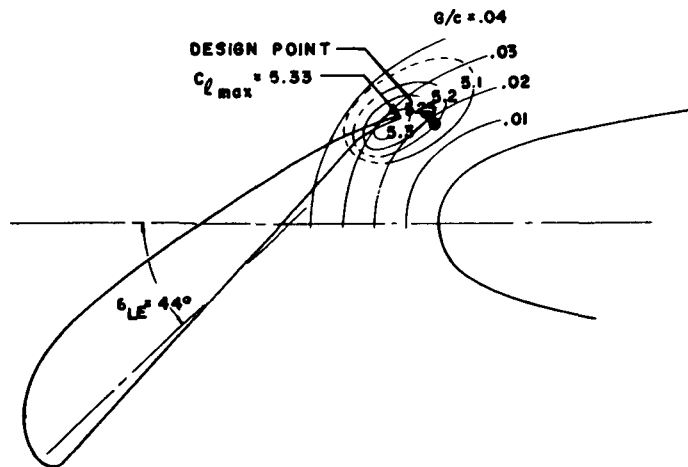


FIGURE 34.—CONTOURS OF SLAT TRAILING-EDGE POSITION FOR CONSTANT $C_{l_{max}}$ FOR MODEL D

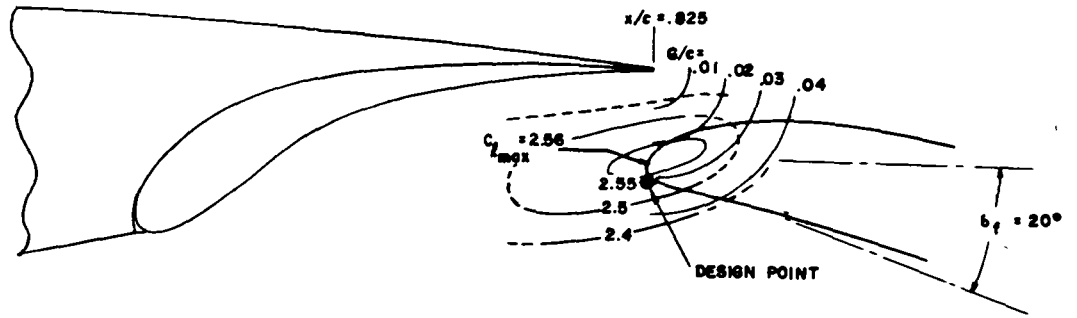


FIGURE 35.—CONTOURS OF THE MODEL B FLAP LEADING-EDGE POSITION FOR CONSTANT $C_{l_{max}}$

SYM	δ_r	δ_{feg}
○	30°/49.7°	44°
□	25°/51.2°	"
△	35°/48.3°	"
◇	28.5°/50.2°	"

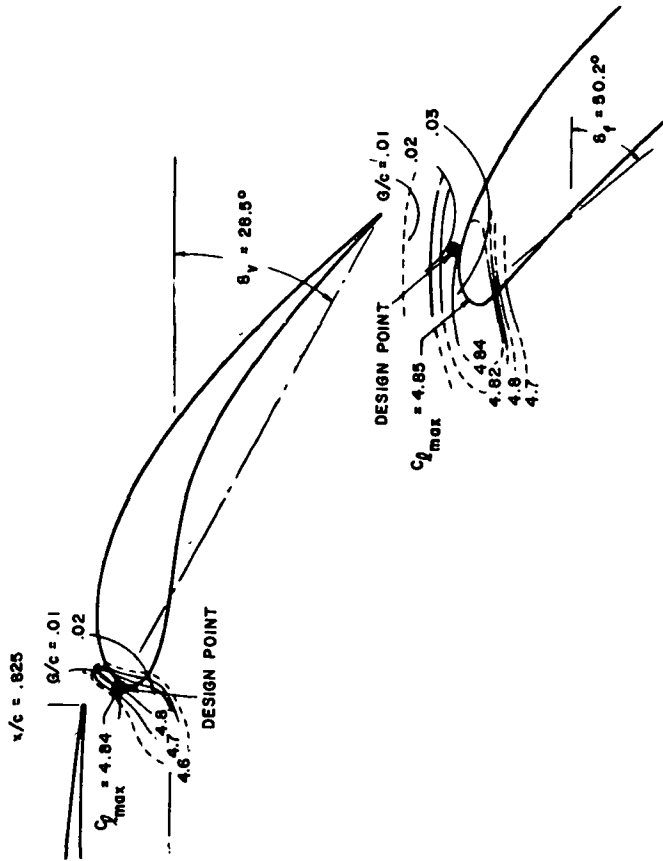
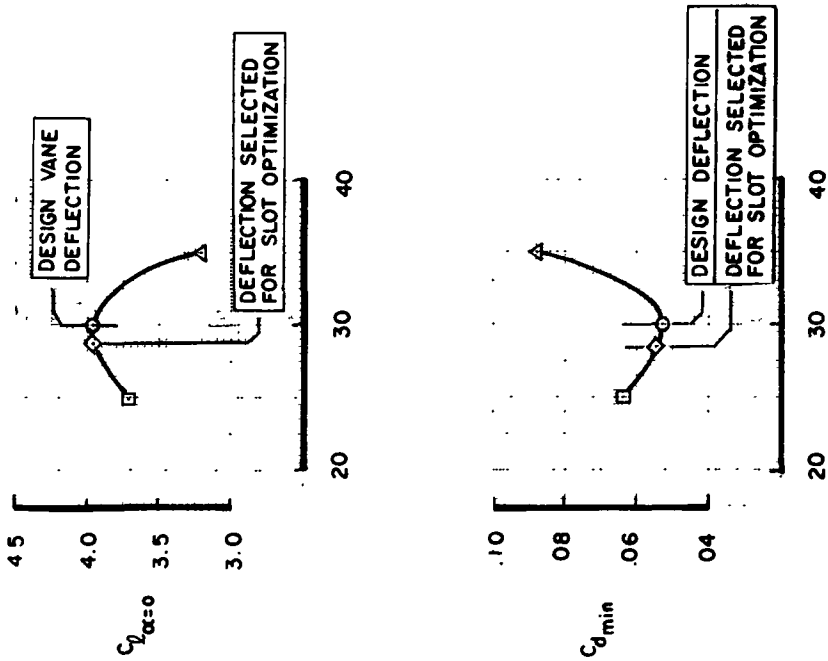


FIGURE 36.— VARIATION OF $C_{d_{max}}$ AND $C_{d_{min}}$ WITH VARYING COMPONENT DEFLECTION COMBINATIONS OF THE DOUBLE-SLOTTED FLAP OF MODEL C

FIGURE 37.— CONTOURS OF THE MODEL C FLAP LEADING-EDGE POSITIONS FOR CONSTANT $C_{d_{max}}$

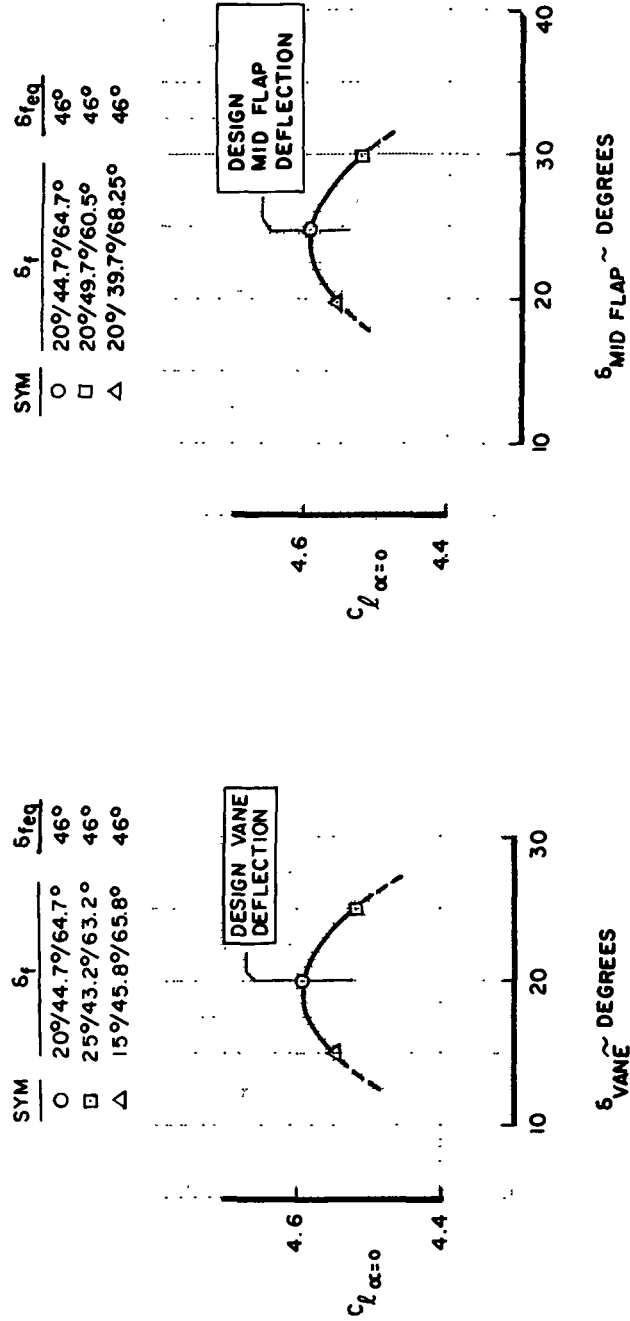


FIGURE 38.— VARIATION OF $C_{l_{max}}$ WITH VARYING COMPONENT DEFLECTION COMBINATIONS
 OF THE TRIPLE-SLOTTED FLAP OF MODEL D

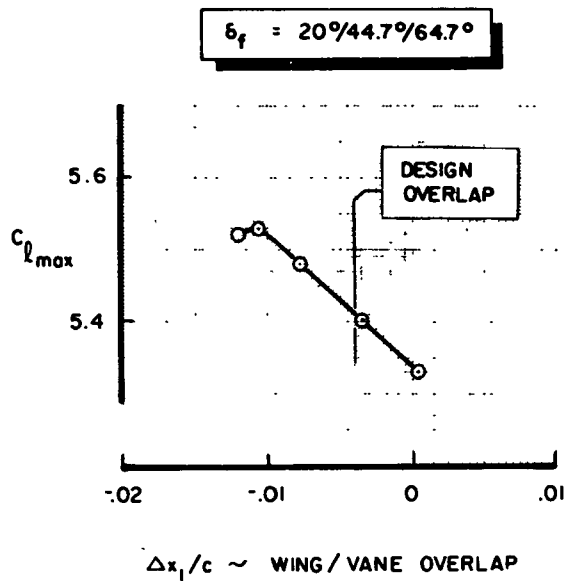


FIGURE 39.—VARIATION OF $C_{l_{max}}$ WITH VARYING OVERLAP OF THE FIRST COMPONENTS OF THE TRIPLE-SLOTTED FLAP OF MODEL D

$\delta_f = 20^\circ$
 $\alpha = 0^\circ$

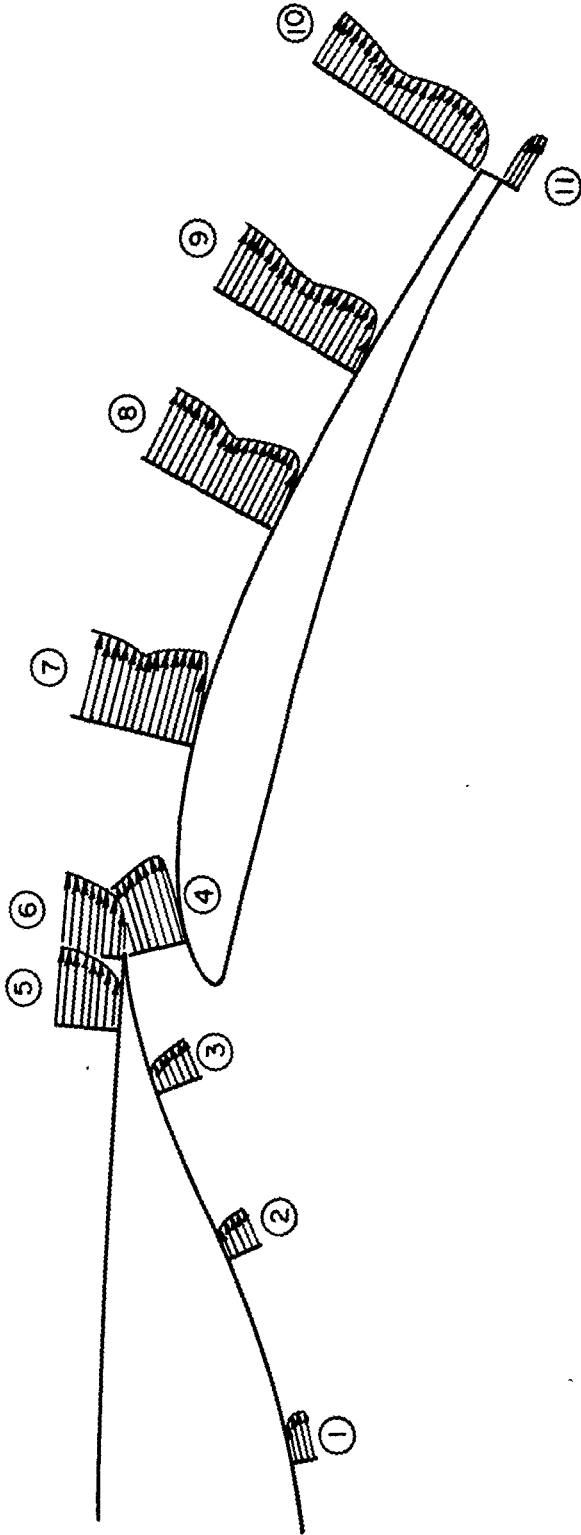


FIGURE 40.—STATIONS AT WHICH BOUNDARY-LAYER PROFILES WERE MEASURED ON MODEL B

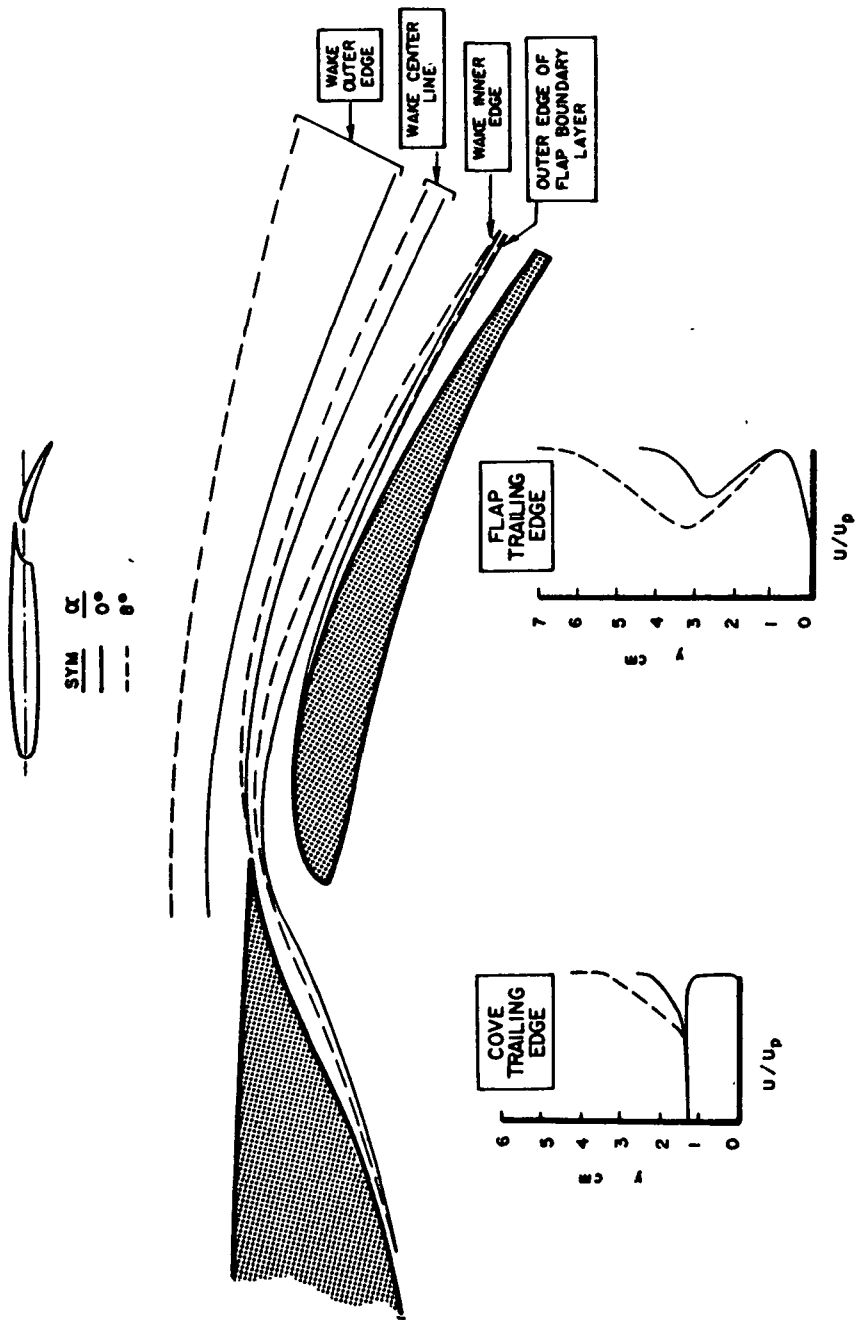


FIGURE 41.—BOUNDARY-LAYER DEVELOPMENT OVER THE FLAP AND COVE OF MODEL B

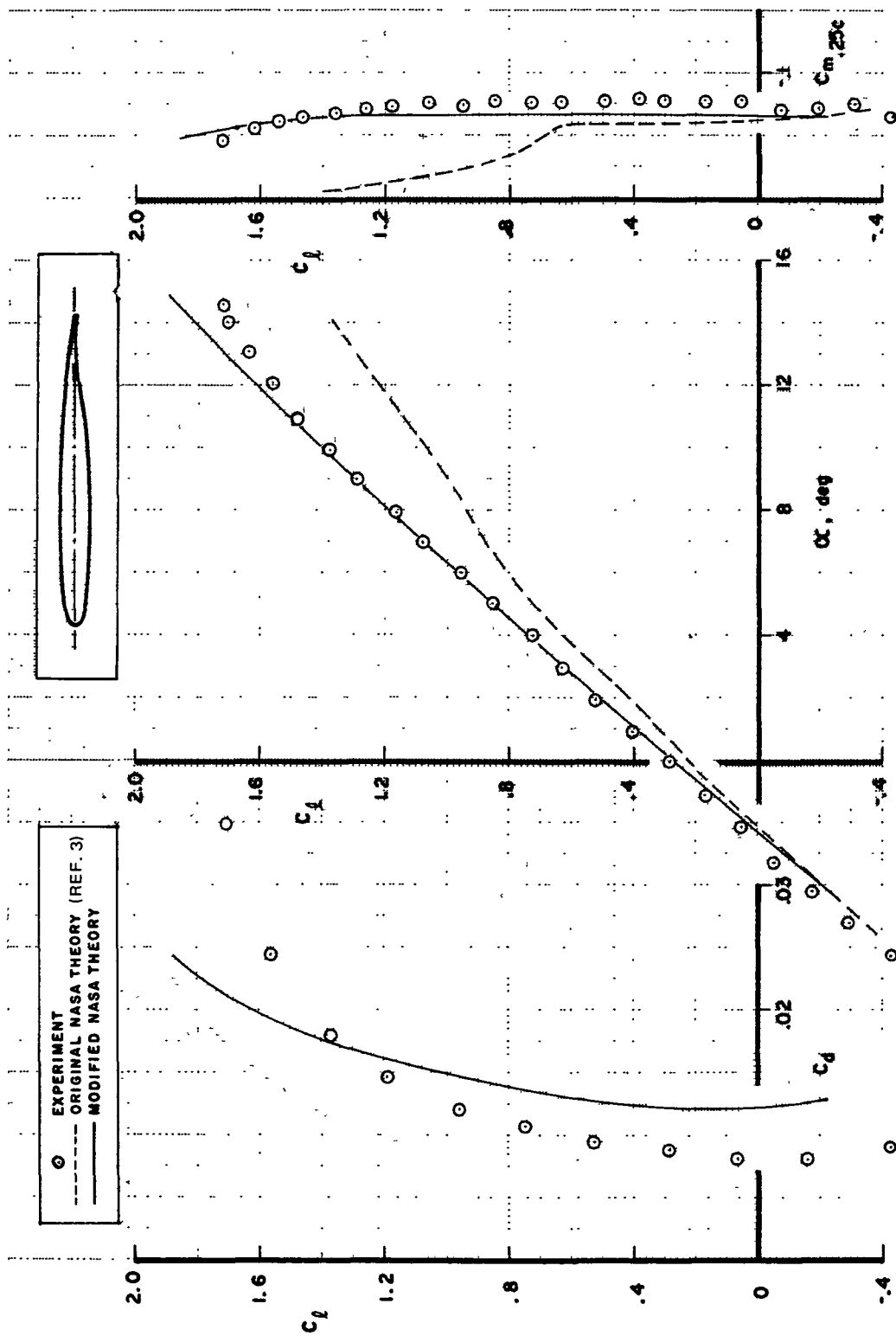


FIGURE 42.—COMPARISON OF THEORETICAL AND EXPERIMENTAL AERODYNAMIC CHARACTERISTICS OF MODEL A

SYM	α	C_L
\odot	-0.002°	.28
—	0°	.244
- - -	0°	.215

EXPERIMENT
MODIFIED NASA THEORY
ORIGINAL NASA THEORY
(Ref. 3)

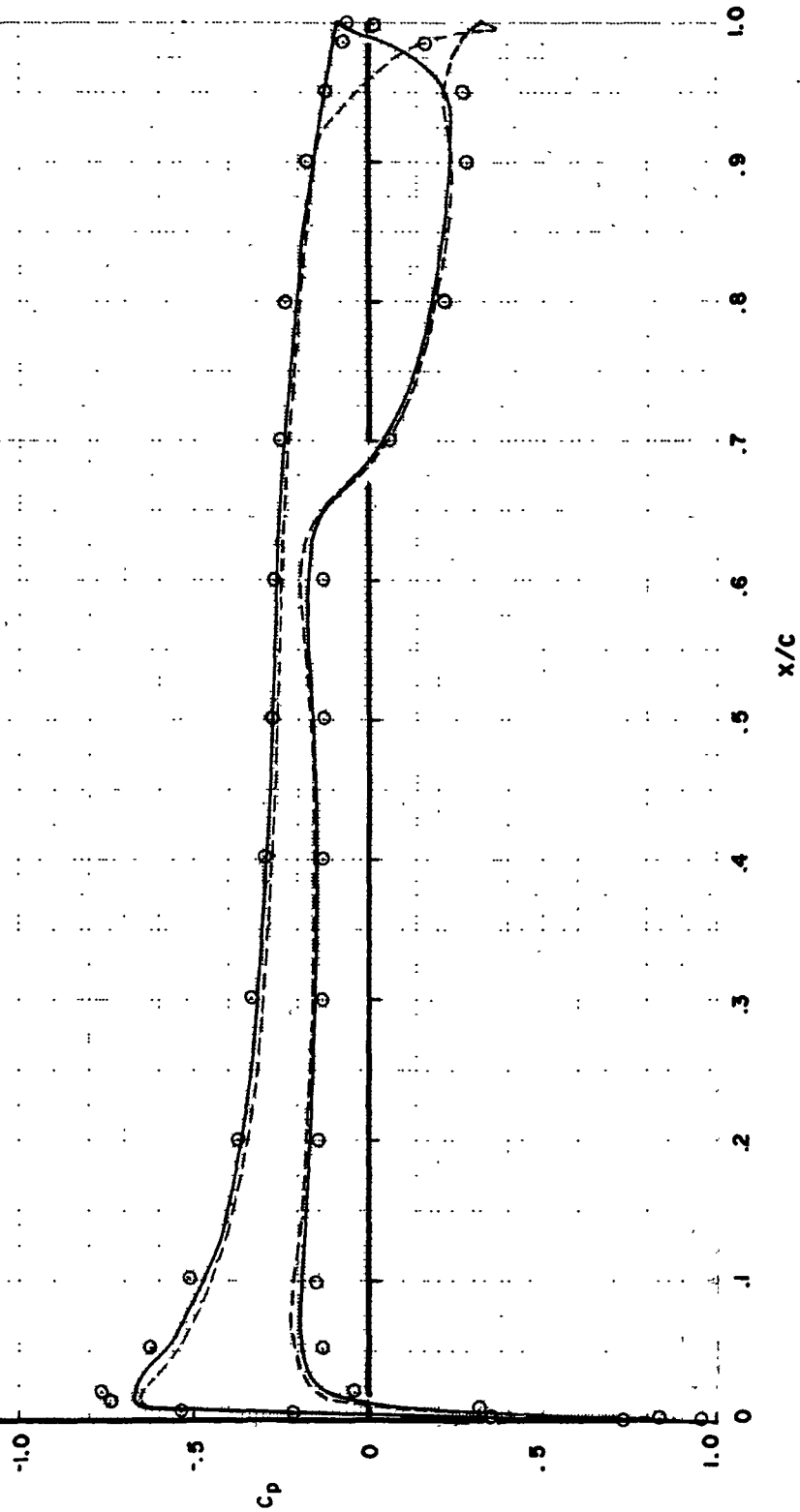


FIGURE 43.—COMPARISON OF THEORETICAL AND EXPERIMENTAL PRESSURES ABOUT MODEL A AT $\alpha = 0^\circ$

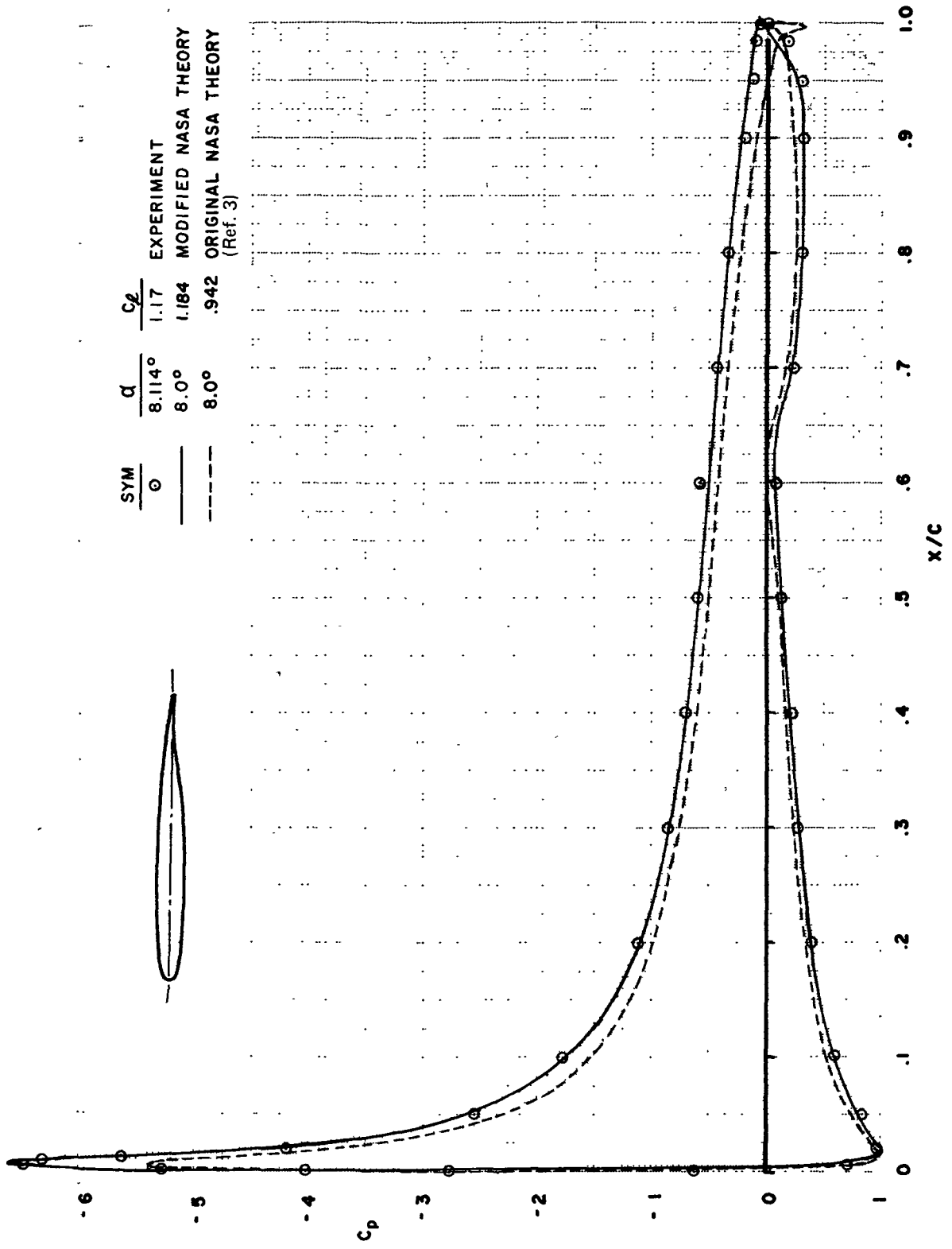


FIGURE 44.—COMPARISON OF THEORETICAL AND EXPERIMENTAL PRESSURES ABOUT MODEL A AT $\alpha = 8^\circ$

○ EXPERIMENT
 — MODIFIED NASA THEORY

SLAT = 45°

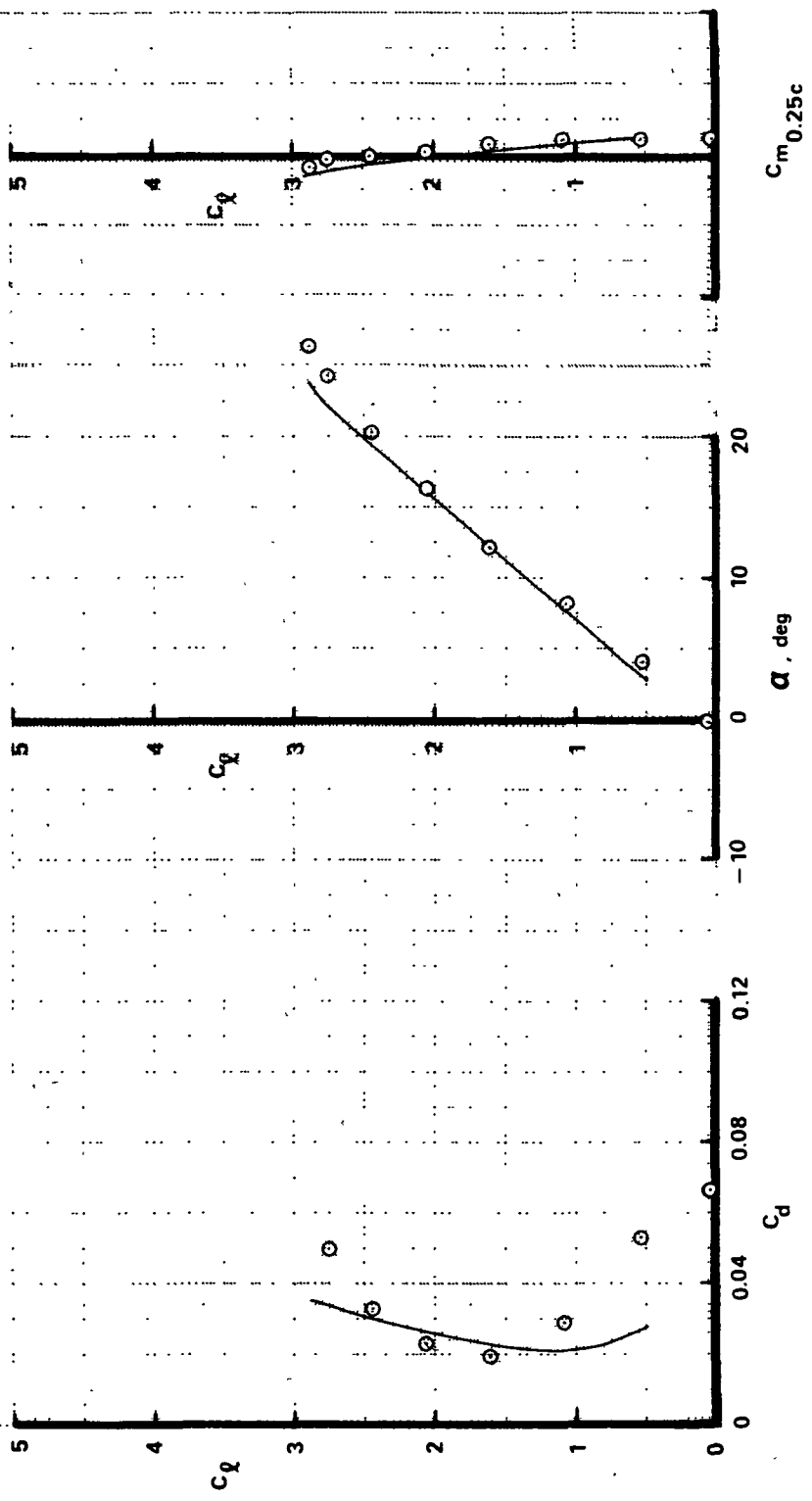
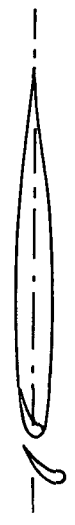


FIGURE 45.—COMPARISON OF THEORETICAL AND EXPERIMENTAL AERODYNAMIC CHARACTERISTICS OF MODEL A WITH LEADING-EDGE SLAT 1

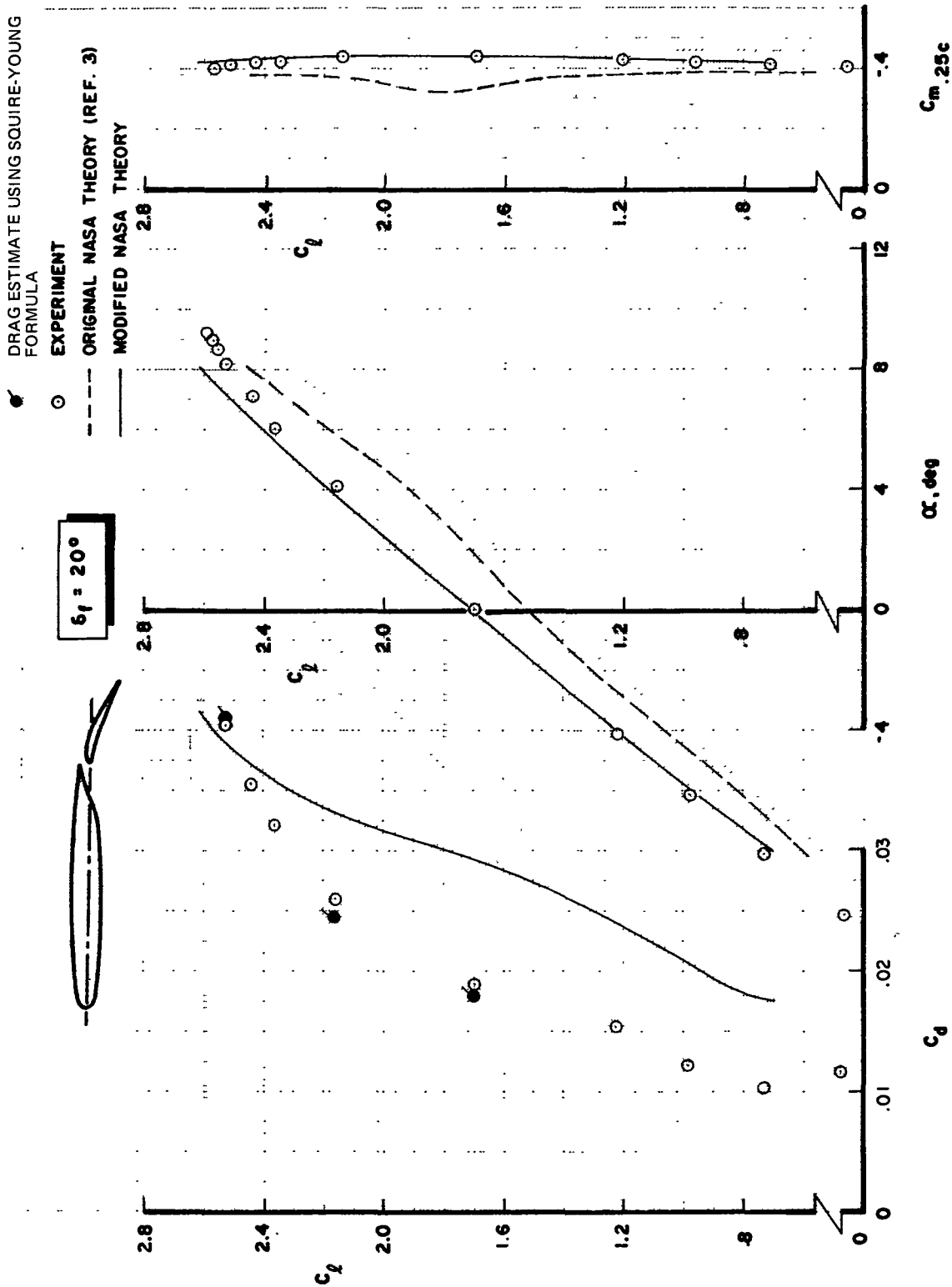


FIGURE 46.—COMPARISON OF THEORETICAL AND EXPERIMENTAL AERODYNAMIC CHARACTERISTICS OF MODEL B FOR $\delta_f = 20^\circ$

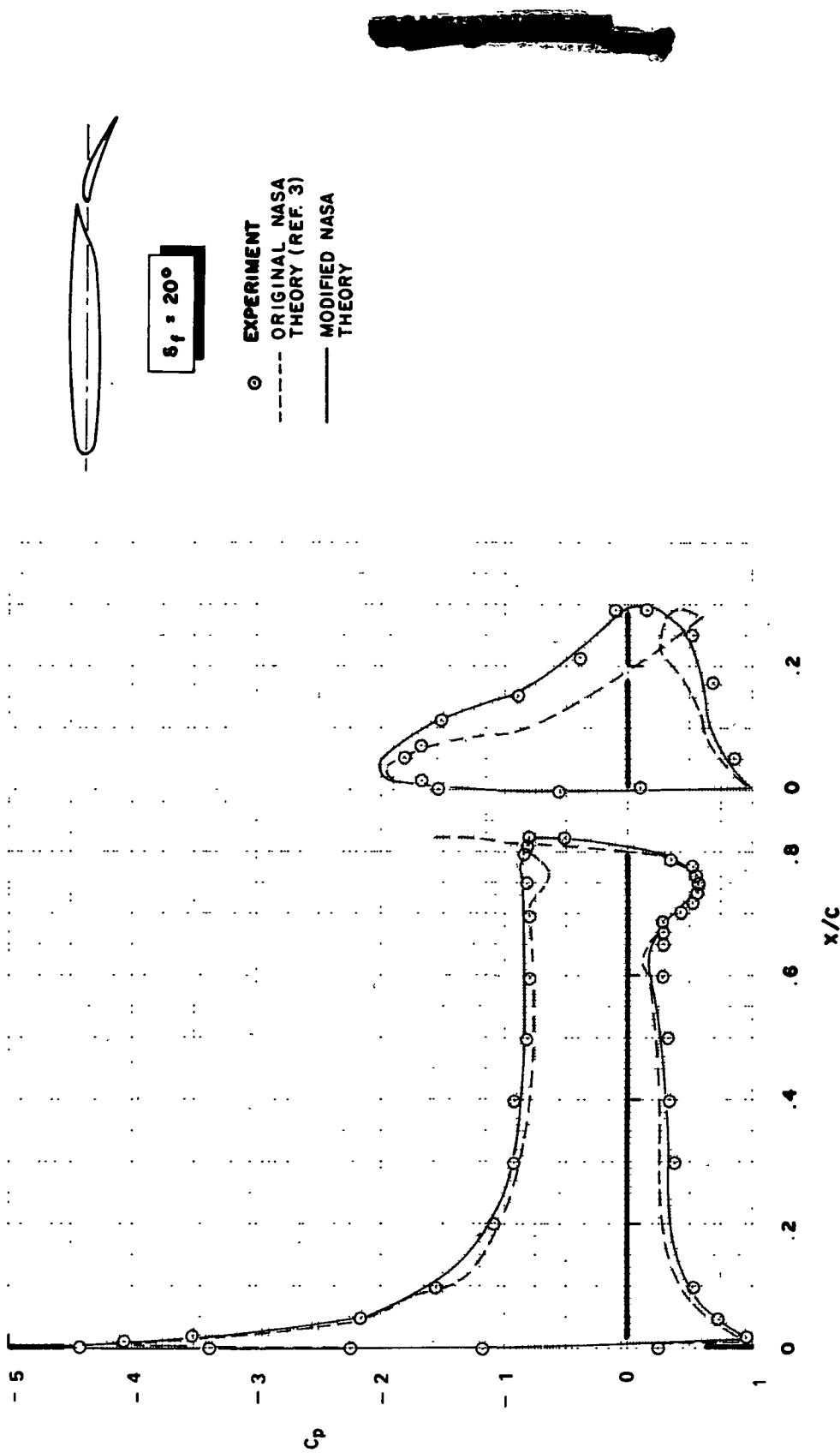


FIGURE 47.—COMPARISON OF EXPERIMENTAL AND THEORETICAL PRESSURES ABOUT MODEL B AT $\alpha = 0^\circ$ AND $\delta_f = 20^\circ$

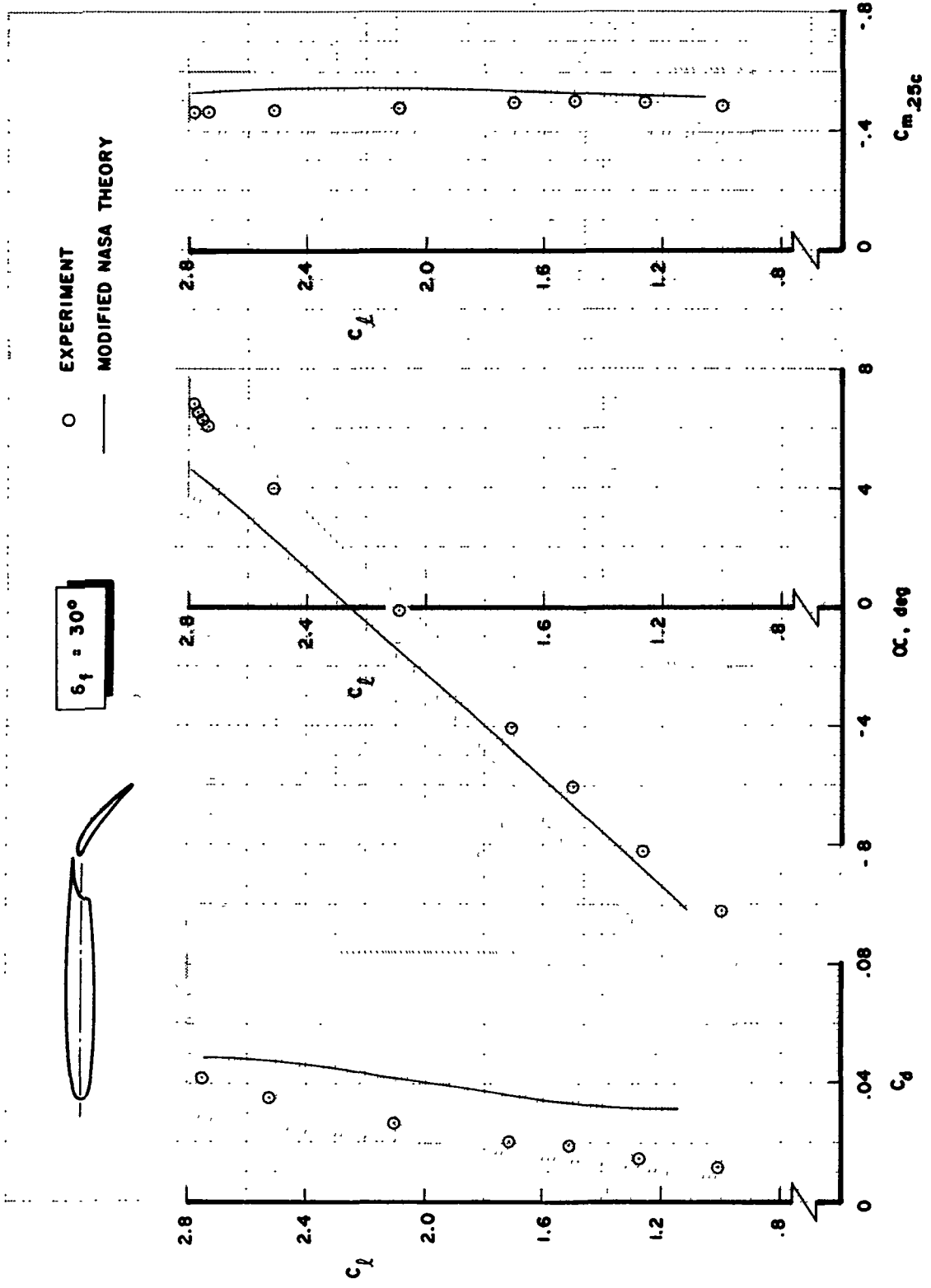


FIGURE 48.—COMPARISON OF THEORETICAL AND EXPERIMENTAL AERODYNAMIC CHARACTERISTICS OF MODEL B FOR $\delta_f = 30^\circ$

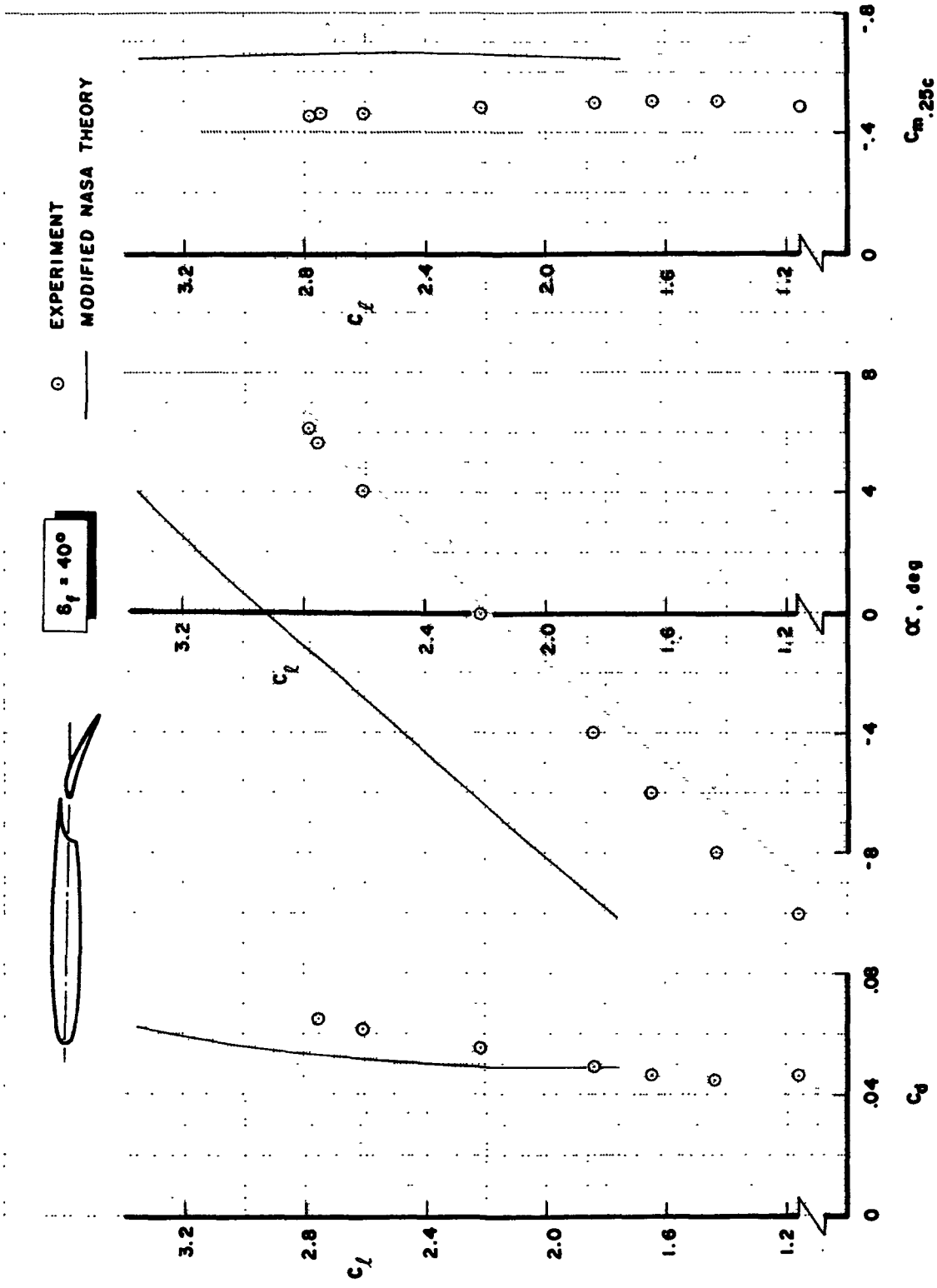


FIGURE 49.—COMPARISON OF THEORETICAL AND EXPERIMENTAL AERODYNAMIC CHARACTERISTICS OF MODEL B FOR $\delta_f = 40^\circ$

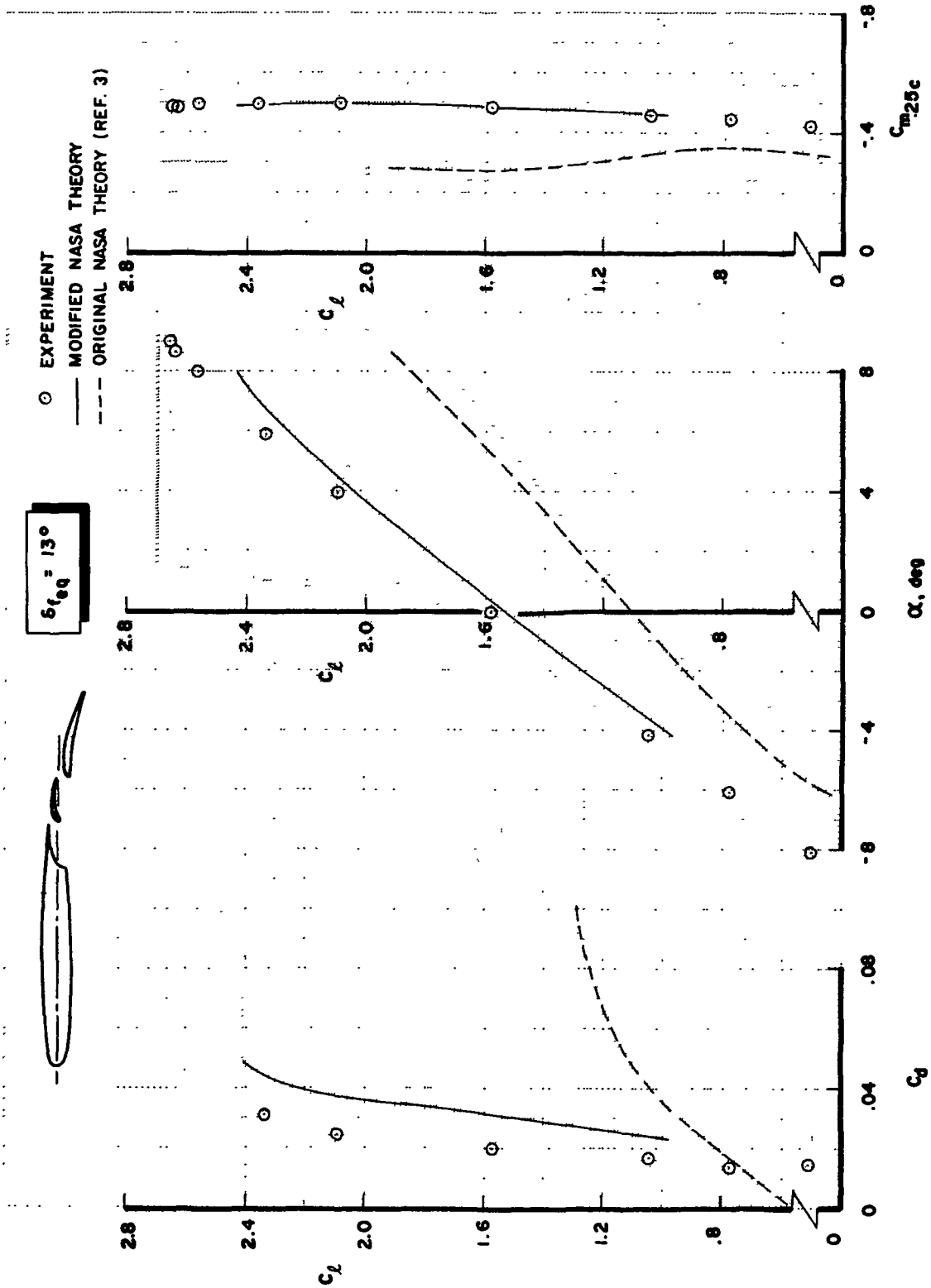


FIGURE 50.—COMPARISON OF THEORETICAL AND EXPERIMENTAL AERODYNAMIC CHARACTERISTICS OF MODEL A WITH A DOUBLE-SLOTTED FLAP AT $\delta_{f_{eq}} = 13^\circ$

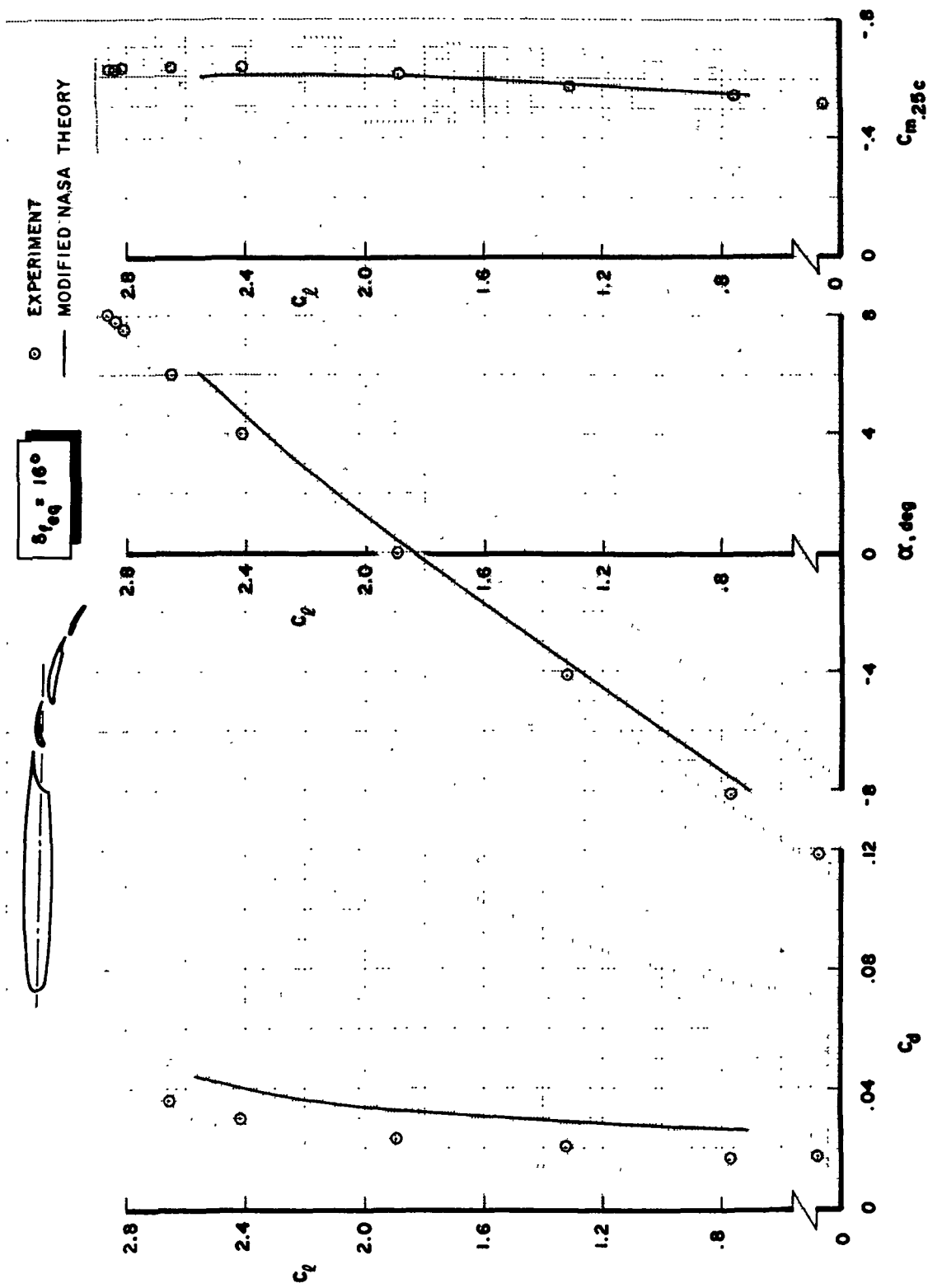


FIGURE 51.—COMPARISON OF THEORETICAL AND EXPERIMENTAL AERODYNAMIC CHARACTERISTICS OF MODEL A WITH A TRIPLE-SLOTTED FLAP AT $\delta_{f,eq} = 16^\circ$

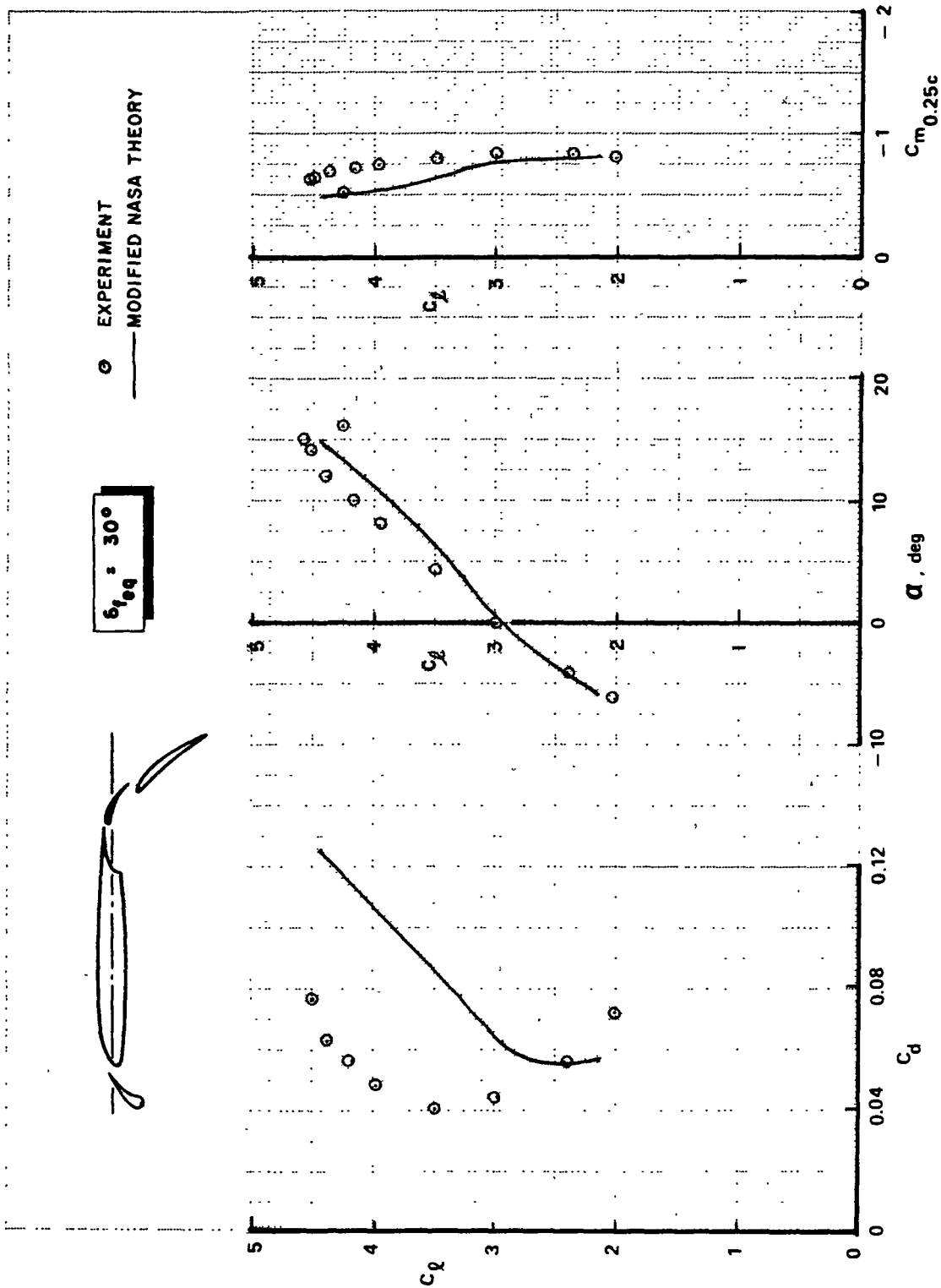


FIGURE 52.—COMPARISON OF THEORETICAL AND EXPERIMENTAL AERODYNAMIC CHARACTERISTICS OF MODEL C FOR $\delta_{f_{eq}} = 30^\circ$

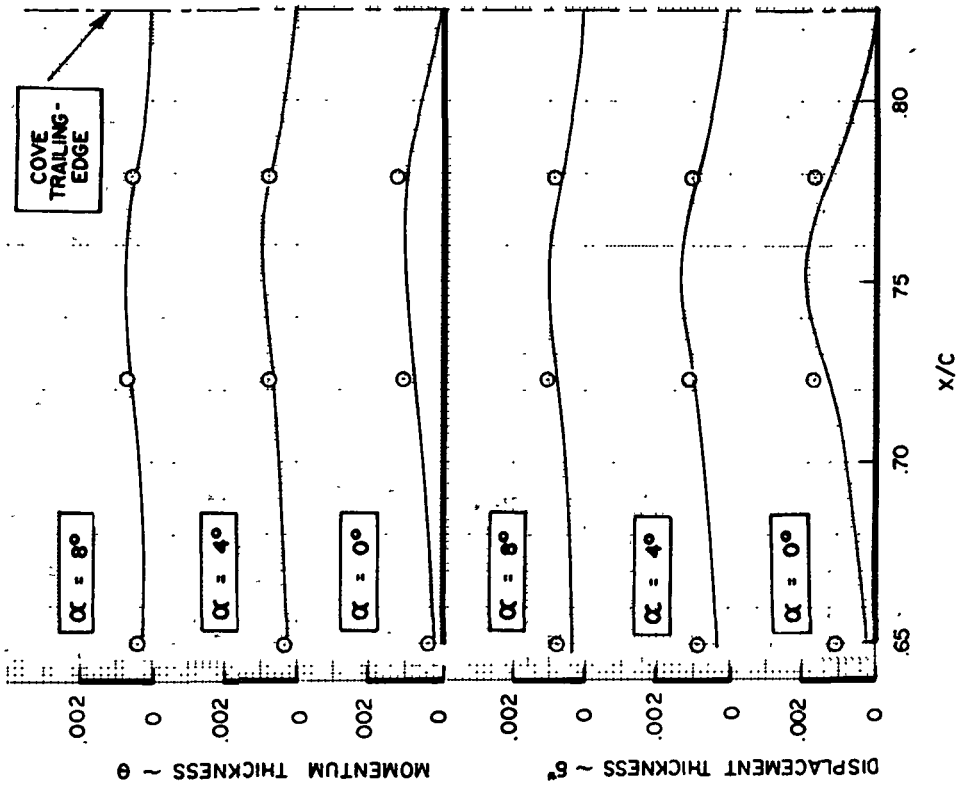
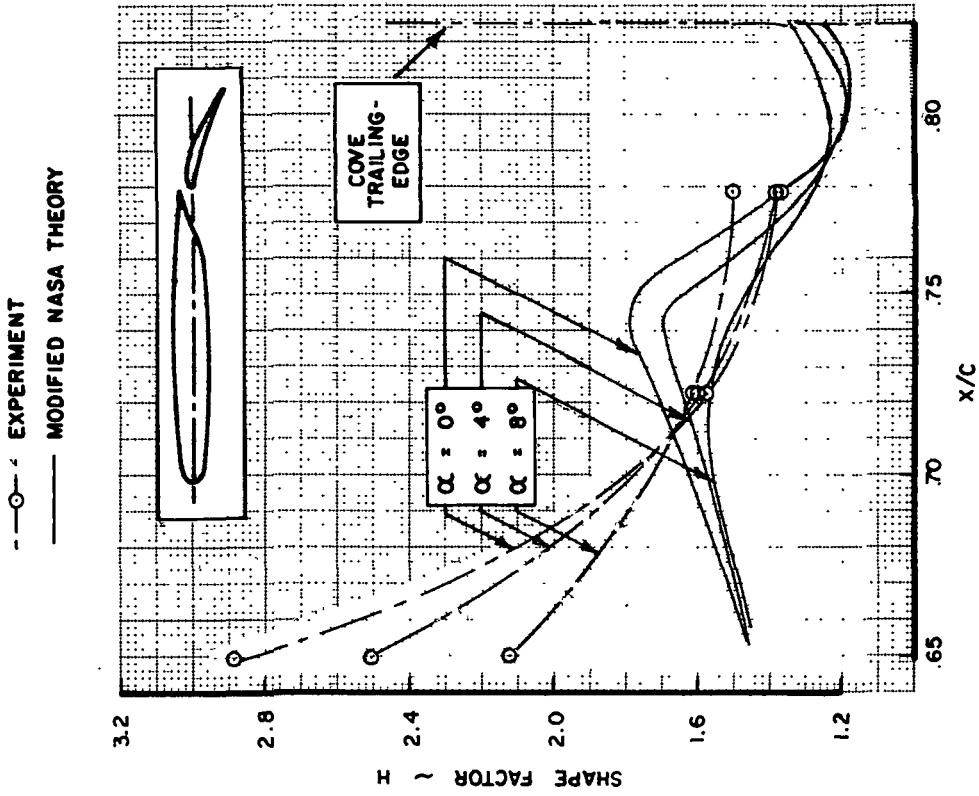


FIGURE 53.—COMPARISON OF THEORETICAL AND EXPERIMENTAL BOUNDARY-LAYER PROPERTIES FOR THE COVE REGION OF MODEL B

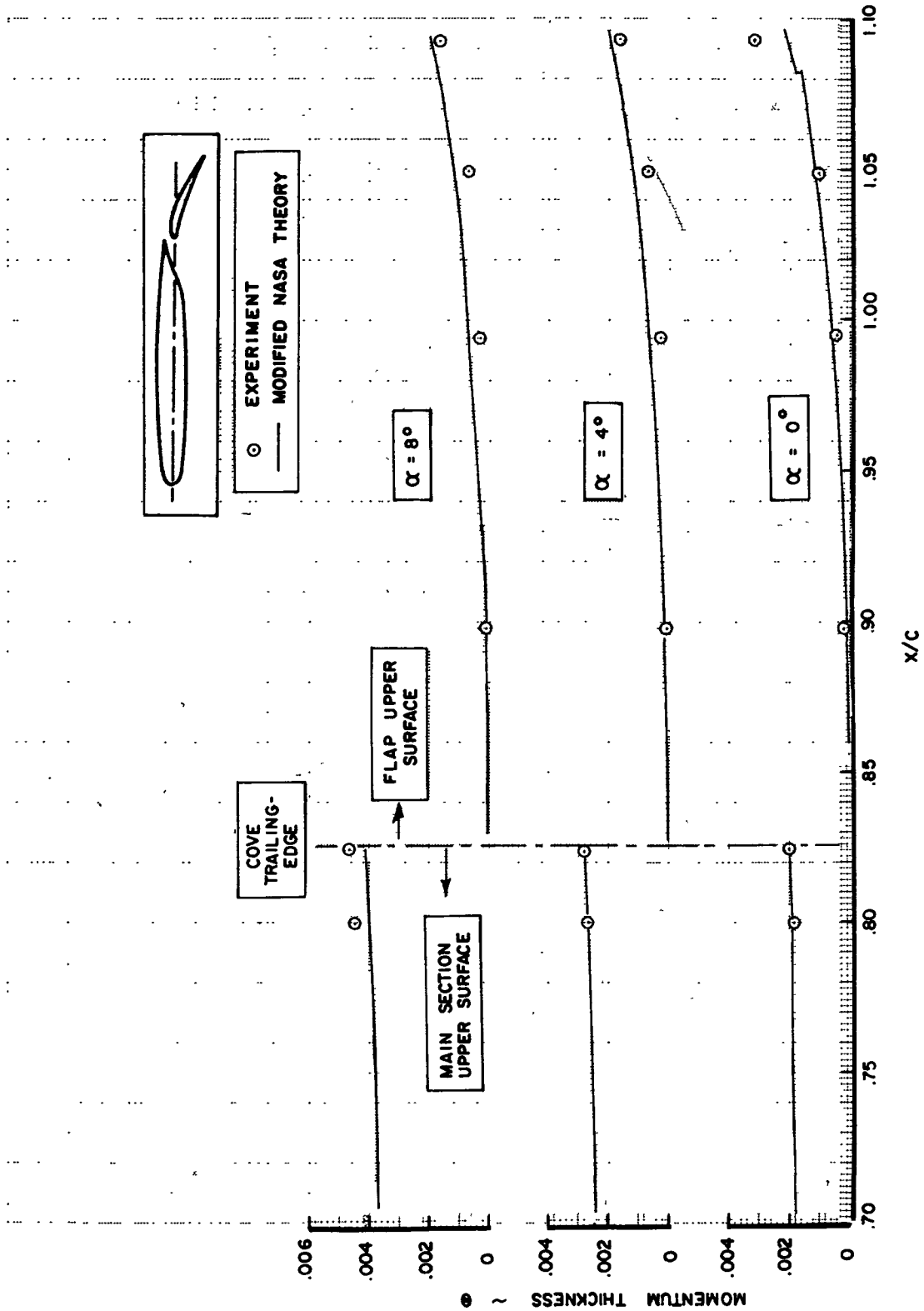


FIGURE 54.—COMPARISON OF THEORETICAL AND EXPERIMENTAL CONFLUENT BOUNDARY-LAYER MOMENTUM THICKNESS FOR MODEL B

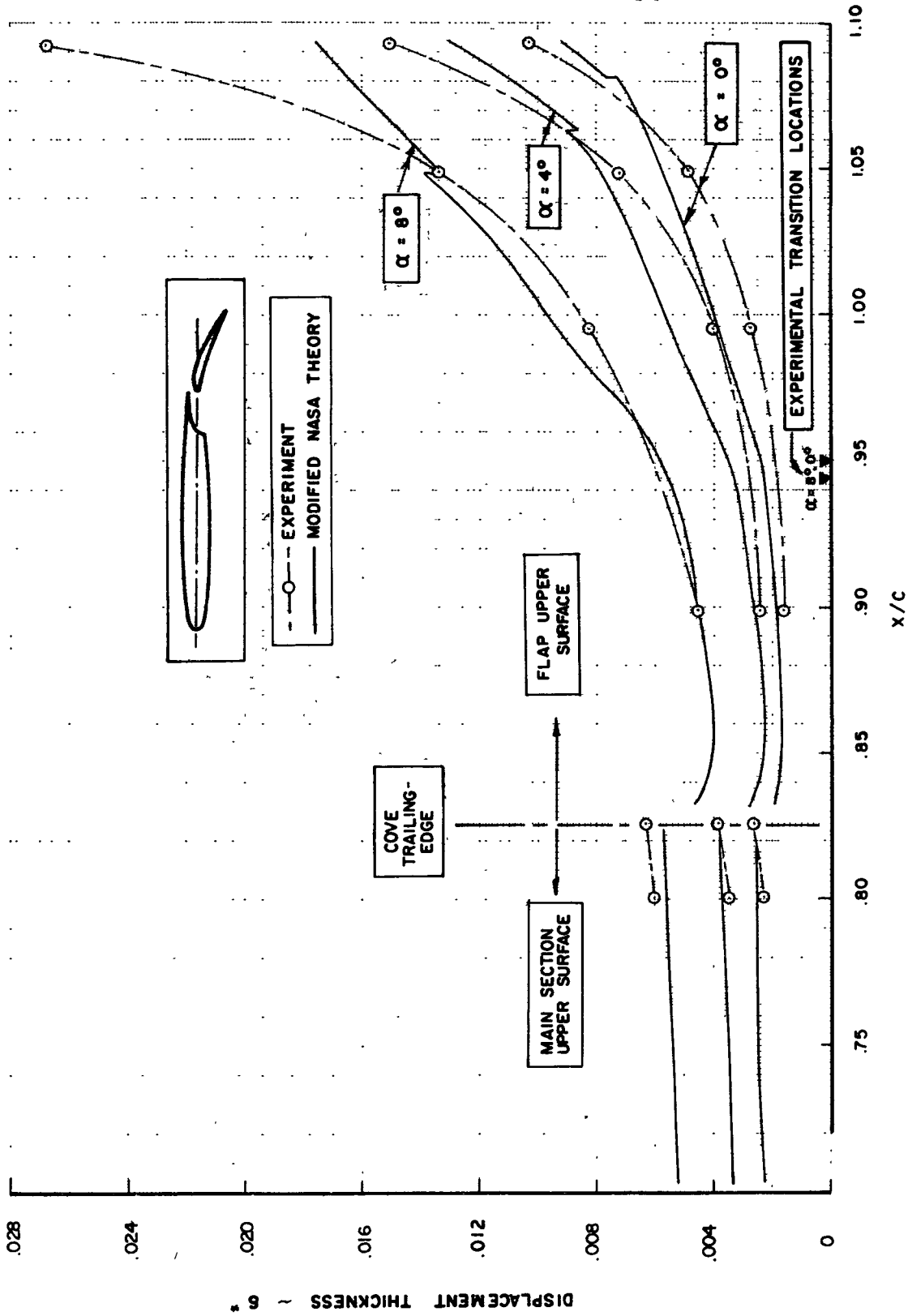


FIGURE 55.—COMPARISON OF THEORETICAL AND EXPERIMENTAL CONFLUENT BOUNDARY-LAYER DISPLACEMENT THICKNESS FOR MODEL B

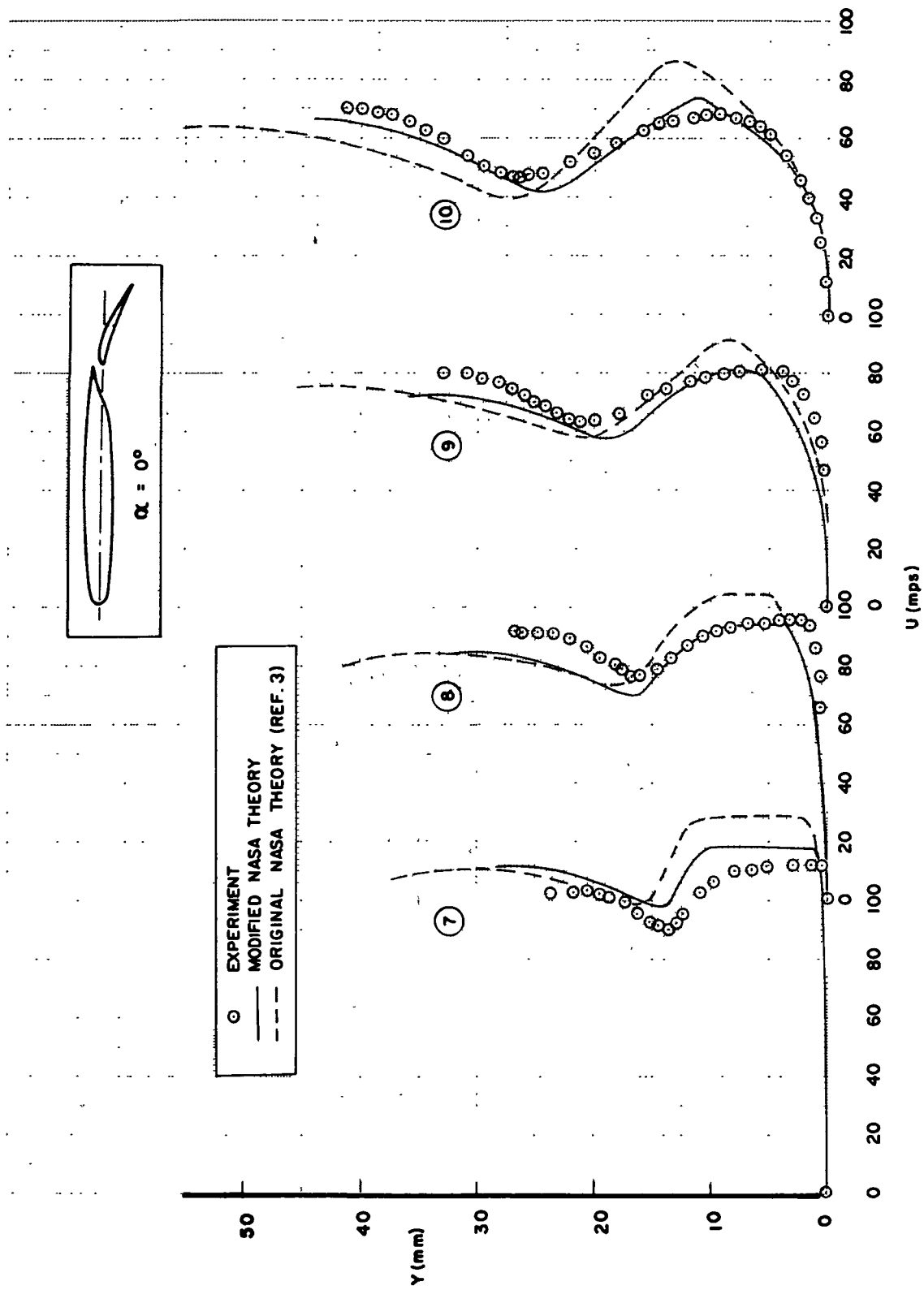


FIGURE 56.—COMPARISON OF THEORETICAL AND EXPERIMENTAL CONFLUENT BOUNDARY-LAYER PROFILES OF MODEL B

"The aeronautical and space activities of the United States shall be conducted so as to contribute . . . to the expansion of human knowledge of phenomena in the atmosphere and space. The Administration shall provide for the widest practicable and appropriate dissemination of information concerning its activities and the results thereof."

— NATIONAL AERONAUTICS AND SPACE ACT OF 1958

NASA SCIENTIFIC AND TECHNICAL PUBLICATIONS

TECHNICAL REPORTS Scientific and technical information considered important, complete, and a lasting contribution to existing knowledge.

TECHNICAL NOTES Information less broad in scope but nevertheless of importance as a contribution to existing knowledge

TECHNICAL MEMORANDUMS
Information receiving limited distribution because of preliminary data, security classification, or other reasons.

CONTRACTOR REPORTS Scientific and technical information generated under a NASA contract or grant and considered an important contribution to existing knowledge.

TECHNICAL TRANSLATIONS: Information published in a foreign language considered to merit NASA distribution in English.

SPECIAL PUBLICATIONS: Information derived from or of value to NASA activities. Publications include conference proceedings, monographs, data compilations, handbooks, sourcebooks, and special bibliographies

TECHNOLOGY UTILIZATION PUBLICATIONS Information on technology used by NASA that may be of particular interest in commercial and other non-aerospace applications. Publications include Tech Briefs, Technology Utilization Reports and Notes, and Technology Surveys.

Details on the availability of these publications may be obtained from:

**SCIENTIFIC AND TECHNICAL INFORMATION OFFICE
NATIONAL AERONAUTICS AND SPACE ADMINISTRATION
Washington, D.C. 20546**